CHARACTERIZATION OF CELLULAR ORGANELLES AND THE ENDO-LYSOSOMAL PATHWAY IN CHOROIDEREMIA PATIENT CELLS

RITA ALEXANDRE COELHO

A dissertation submitted in partial fulfilment of the requirements for the Degree of Masters in Biomedical Research (Specialization Area: Ageing and chronic diseases) at Faculdade de Ciências Médicas | NOVA Medical School of NOVA University Lisbon

September, 2022

CHARACTERIZATION OF CELLULAR ORGANELLES AND THE ENDO-LYSOSOMAL PATHWAY IN CHOROIDEREMIA PATIENT CELLS

Rita Alexandre Coelho
Supervisors: Mafalda Lopes-da-Silva, PhD at NOVA Medical School

A dissertation submitted in partial fulfilment of the requirements for the Degree of Masters in Biomedical Research (Specialization Area: Ageing and chronic diseases)

September, 2022

Funding

The studies presented on this master thesis were performed in the research group “Molecular Mechanisms of Disease”, headed by Professor Miguel Seabra, at NOVA Medical School Research Center – NOVA Medical School, Lisbon, under the supervision of Mafalda Lopes-da-Silva, PhD.

Funding: This work is supported by the Fundação para a Ciência e Tecnologia (FCT) project **EXPL/MED-OUT/0599/2021**; iNOVA4Health – **UIDB/04462/2020** and **UIDP/04462/2020**, and by the Associated Laboratory LS4FUTURE (**LA/P/0087/2020**), two programs financially supported by Fundação para a Ciência e Tecnologia / Ministério da Ciência, Tecnologia e Ensino Superior.

Outputs

Rita Coelho, Daniela Oliveira, Pedro Antas, Mafalda Lopes da Silva, Sandra Tenreiro, Miguel Seabra. Characterization of cellular organelles and the endo-lysosomal pathway in choroideremia patient cells. Lysocil Final Conference. 7th – 9th April 2022, Cascais [Flash talk and Poster Presentation]

Acknowledgments

Começo por agradecer ao Professor Paulo Pereira e às Professoras Rita Teodoro e Cláudia Almeida e a todos os restantes membros da Coordenação do Mestrado em Investigação Biomédica pela incrível oportunidade que foi frequentar um curso que tanto me ensinou. Um agradecimento à faculdade de Ciências Médicas da Universidade NOVA de Lisboa que durante dois anos me acolheu.

Aos membros do laboratório Molecular Mechanisms of Disease e do laboratório Aging and Degeneration quero agradecer todo o apoio que me deram ao longo deste ano. Foi um orgulho fazer parte de um grupo que todos os dias trabalha e se esforça para elevar a ciência em Portugal. Obrigada ao Prof. Miguel Seabra, Dra. Sandra Tenreiro, Dra. Sofia Falcão, Dra. Luísa Lemos e a Ana Fradinho por toda a ajuda. Ao Dr. Pedro Antas que, de uma forma muito paciente, me ensinou tudo o que sei sobre as tão queridas hiPSc.

Um agradecimento especial às minhas colegas de viagem que rapidamente se tornaram família, Rita, Marta, Inês e Daniela. Obrigada a todas pelos almoços tardios, as noites no microscópio e as tardes na MU.

À minha orientadora, Dra. Mafalda Lopes-da-Silva, devo tudo o que esta tese representa. Agradeço-lhe todas as dicas e incansável apoio ao longo de todo o processo, e por me ter ensinado a ser independente e crítica com tudo o que me deparo. Não poderia ter privado com melhor orientadora que rapidamente ganhou a minha admiração pelo seu sentido encorajador, persistente e humano. Foi um prazer ser guiada nesta viagem pela Dra. Mafalda e levo comigo um ano recheado de conhecimento.

Aos meus colegas do mestrado em Investigação Biomédica, foi um orgulho fazer parte de um grupo de pessoas tão incríveis. Obrigada pelas noites de zoom, maratonas de apresentações, piqueniques no Torel e todos os jantares.

Um obrigada gigante aos meus amigos: **Sofia** e **Ana Rita** por serem os meus pilares. À **Maiara** que há 23 anos é a minha melhor amiga, estás longe, mas sempre perto. Ao **Luís**, **Ana** e **Liliana** por todos os conselhos. À **Filipa**, **Luísa**, **Maria Laura**, **Vicente**, **Pedro**, **Fábio** e **Tiago** agradeço por os ter conhecido e terem partilhado esta viagem comigo. Obrigada pelas conversas, restaurantes falhados, danças pela noite fora e tardes de bowling.

À minha família, à minha **mãe** e **pai**, os meus corações fora do corpo, obrigada por tudo o que sou. Obrigada pelo apoio incondicional, eternamente agradecida por todas as oportunidades que me deram. Não há palavras suficientes que descrevam a gratidão que sinto. Dedico-vos esta tese, que é tanto minha como vossa. Obrigada por sempre me ouvirem a falar incansavelmente de ciência e tentarem perceber. Obrigada, pai, por seres a pessoa humana e empática que és e a ti mãe, o meu modelo a seguir e melhor amiga, obrigada por teres tentado perceber o meu projeto e ao fim de tantos meses finalmente sabes dizer coroideremia.

Aos meus avós e tios, obrigada pelos almoços em família e por todo o apoio ao longo dos anos, um obrigada especial à minha **Avó**, a minha segunda mãe, por me dares força e me mostrares o que significa ser Mulher.

À minha irmã, **Beatriz**, obrigada por tudo.

Abstract

Keywords: Choroideremia, Retinal Pigment Epithelium, Photoreceptor outer segments, human induced Pluripotent Stem Cells, ARPE-19, endocytic lysosomal pathway

Choroideremia (CHM) is a form of retinal degeneration, with an X-linked pattern of inheritance caused by mutations in the *CHM* gene that codifies the Rab Escort Protein 1 (REP1). Given its genetic component and the closed system of the eye, CHM is an excellent target for gene therapy. However, this type of treatment still presents its challenges, thus it is important to uncover new molecular mechanisms of the disease, with the hopes of finding new therapeutic targets. The retinal pigment epithelium (RPE) consists of a monolayer of cells, localized between the choroid and the photoreceptors. The RPE is functionally diverse, performing tasks such as the daily phagocytosis and degradation of photoreceptor outer segments (POS), secretion of growth factors and transport of nutrients and metabolites. The REP1 protein is responsible for the geranylgeranylation of Rab GTPases, a post-translational modification that facilitates the binding of these small GTPases to membranes and therefore, exert their role in the regulation of membrane traffic. CHM patients have been shown to have RPE dysfunction; accumulation of unprocessed POS accompanied by a reduced degradation capacity and a decrease in phagosomal acidity.

With this project we intended to make a full characterization of cellular organelles and pathways, to dissect new uncharacterized cellular defects, with a focus on the endo-lysosomal pathway, as well as the impact of unprocessed POS accumulation in CHM RPE cells. To carry out our objective we used two different *in vitro* RPE cell models: differentiated RPE from human induced pluripotent stem cells from both healthy and CHM patient donors, hiPSc-RPE, and a commonly used immortalized RPE cell line, ARPE-19 where we used CRISPR/Cas9 to generate a CHM KO line. Characterization of the endo-lysosomal pathway revealed an increase in the number of LAMP1+ and CD63+ vesicles in both hiPSc-RPE and ARPE-19 CHM cell models, suggesting an increase in the number of both lysosomes and multivesicular bodies (MVBs), respectively. Western blot analysis of CHM hiPSc-RPE whole cell lysates revealed an increase in (inactive) procathepsin D and L, suggesting an impairment in the delivery of the immature form of these antibodies cathepsin forms to their proper cellular compartments, pointing to a targeting dysfunction within the endo-lysosomal pathway. Additionally, in ARPE-19 CHM cells, after a single pulse of POS, a significant accumulation of autofluorescent granules (AFGs) was observed, verified at both 24h- and 72h- post feeding resulting from incomplete digestion of POS. Furthermore, hiPSc-RPE CHM cells revealed an increase in cell size as well as a decrease in polarization, as analysed by a decrease in the transepithelial electrical resistance (TER), suggesting a dysfunction in the establishment of a tight monolayer, this evidence should be further analysed. Overall, this work provides novel evidence of cellular dysfunction in CHM cells, specifically on the endo-lysosomal pathway, as well as POS incorporation and degradation. We also show key differences between two cellular models of RPE, describing advantages and disadvantages of each model for the use of different assays and technical approaches. In the future, we aim to achieve optimized protocols for hiPSc-RPE to overcome

technical challenges and make hiPSc-RPE an even better model of human RPE to investigate the molecular and cellular mechanisms of choroideremia as well as other diseases of the RPE.

Resumo

A coroideremia (CHM) é uma forma de degeneração da retina, com um padrão de transmissão ligado ao cromossoma X, causada por mutações no gene *CHM* que codifica a *Rab escort protein 1* (REP1). Devido ao seu componente génico e ao sistema fechado presente no olho, a CHM é um excelente alvo para terapia génica. No entanto, este tratamento apresenta desvantagens, sendo da maior importância decifrar potenciais mecanismos moleculares tendo em vista a descoberta de novos alvos terapêuticos. O epitélio pigmentado da retina (RPE) consiste numa monocamada de células localizadas entre a coroide e os fotorreceptores. O RPE é funcionalmente diverso, apresentando como principais funções a fagocitose e degradação diária dos segmentos externos dos fotorreceptores (POS), a secreção de fatores de crescimento e o transporte de nutrientes e metabolitos. A proteína REP1 é responsável por uma modificação pós-traducional nas proteínas Rab GTPases que facilita a ligação das proteínas Rab a membranas biológicas, de forma a exercer o seu papel na regulação do tráfico celular. Dados prévios revelam que pacientes com CHM podem apresentar defeitos no epitélio pigmentado da retina, acumulação de POS não processados acompanhados de uma redução da capacidade degradativa, e uma diminuição da acidez dos fagossomas. Com este projeto, pretendemos efetuar uma caracterização total dos organelos celulares e de vias de sinalização, com o intuito de decifrar novos defeitos celulares, com um foco na via endocítica-lisosomal. Além disso tivemos também o objetivo de analisar o impacto da acumulação de POS não processados em células RPE CHM. Com esse propósito, foram empregues dois modelos diferentes de RPE *in vitro*: RPE diferenciado a partir de células humanas com pluripotência induzida de dadores saudáveis e pacientes, hiPSc-RPE, e uma linha celular imortalizada, ARPE-19, onde se recorreu à técnica CRISPR/Cas9 para gerar uma linha *knockout* para o gene da CHM. A caracterização da via endo-lisosomal revelou um aumento no número de vesículas LAMP1+ e CD63+ em ambos os modelos de CHM, hiPSc-RPE e ARPE-19, sugerindo, respetivamente, um aumento de lisossomas e corpos multivesiculares (MVBs). Análises de western blot de células hiPSc-RPE CHM, revelaram um aumento dos níveis de expressão de pro-catepsina (inativa) D e L, indicando uma disfunção na distribuição das formas imaturas de catepsina para os respetivos compartimentos, onde se desencadeia a sua ativação. Adicionalmente, em células CHM ARPE-19, após um único pulso de POS, verificou-se uma acumulação significativa de grânulos autofluorescentes a 24h e 72h após o estímulo, sendo estas resultante de uma digestão incompleta de POS, que modela a lipofuscina *in vivo*. Além disso, células CHM hiPSc-RPE revelaram um aumento de tamanho e uma diminuição no seu nível de polarização, de acordo com análises da resistência elétrica transepitelial (TER), o que sugere uma disfunção no estabelecimento de uma monocamada coesa. Contudo, estas evidências devem ser analisadas mais a fundo. Em suma, este trabalho providenciou novas evidências relativamente a fenótipos celulares de estruturas pertencentes à via endo-lisosomal, e também relativos à incorporação e degradação de POS. Também demonstrámos diferenças chave entre os dois modelos de RPE, descrevendo vantagens e desvantagens de cada um dos modelos em diferentes ensaios e abordagens técnicas. Como perspetiva futura, pretendemos otimizar protocolos para a diferenciação de células hiPSc-RPE de forma a ultrapassar desafios técnicos, e tornar estas

células num modelo ainda mais fidedigno de RPE de forma a investigar os mecanismos moleculares e celulares de coroideremia.

Table of contents

List of Figures

List of Tables

List of Abbreviations

AAV	Adeno-associated virus
AFGs	Autofluorescent granules
AMD	Age-related macular degeneration
CavME	Caveolin-mediated endocytosis
CIE	Clathrin-independent endocytosis
CHM	Choroideremia
CHML	CHM - Like
CME	Clathrin-mediated endocytosis
CRISPR	Clustered Regularly Interspaced Short Palindromic Repeats
CTSB	Cathepsin B
CTSD	Cathepsin D
CTSL	Cathepsin L
EE	Early endosomes
EEA1	Early endosome antigen 1
EP	Early phagosome
GAP	GTPase activating protein
GEF	Guanine nucleotide exchange factors
hESCs	Human embryonic stem cells
hfRPE	Human fetal retinal pigment epithelium
hiPSc	Human induced pluripotent stem cells
ILVs	Intraluminal vesicles
IRDs	Inherited retinal diseases
LAMP	Lysosome-associated membrane protein
LCA	Leber's Congenital Amaurosis
LE	Late endosomes
LP	Late phagosomes
LSDs	Lysosome storage disorders
MVBs	Multivesicular bodies
NPC1	Niemman-Pick disease type C1
PCR	Polymerase chain reaction
PMEL	Premelanosomal protein
POS	Photoreceptor outer segments
PtdSer	Phosphatidylserine
REP	Rab escort protein
REP1	Rab escort protein 1
REP2	Rab escort protein 2
RGGT	Rab geranylgeranyl transferase
RP	Retinitis pigmentosa
RPE	Retinal pigment epithelium
SD	Stargardt disease
SNAREs	Soluble N-ethylmaleimide sensitive factor attachment receptors
TER	Trans-epithelial electrical resistance
ZO-1	Zonula Occludin-1

Chapter 1 – Introduction

1.1. The endo-lysosomal pathway

The endo-lysosomal pathway is comprised of a series of intracellular interconnected membranous compartments that are dynamically transported along the cell, such as early endosomes (EEs), recycling endosomes, late endosomes (LEs) and lysosomes[5]. The main function of such a system is to regulate protein degradation and recycling, in order to maintain cellular homeostasis[6]. The existence of different types of compartments is characterized by distinct phenotypes, one of them the acquisition of distinct regulatory proteins, known as Rab family of small GTPases[6,7], as represented in **Figure 1**.

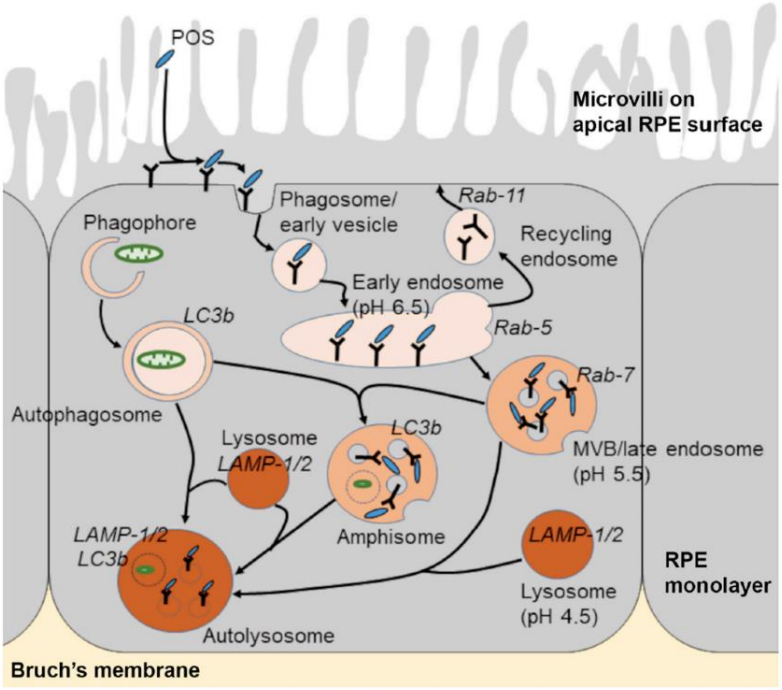

Figure 1. The endocytic-lysosomal pathway in the retinal pigment epithelium (RPE) and some regulatory Rabs. Cargo internalization begins with recognition by specific receptors on the apical surface of RPE and entry in the phagocytic pathway into early endosomes, Rab5 is then recruited, and the maturation process begins into late endosomes (LEs)/multivesicular bodies (MVBs), where Rab5 is converted into Rab7, a common marker of late endosomes. LEs/MVBs fuse with lysosomes for degradation. Recycling endosomes, as well as components from the autophagic pathway are also represented in the Figure. Adapted from Keeling, E., Lotery, A., Tumbarello, D., & Ratnayaka, J. (2018). Impaired Cargo Clearance in the Retinal Pigment Epithelium (RPE) Underlies Irreversible Blinding Diseases. Cells, 7(2), 16.

1.1.1. Rab family of GTPases

Rab GTPases are small proteins, that switch between an active (GTP-bound) and inactive (GDP-bound) state, **Figure 2**. When active they bind to effectors and biological membranes to perform their important role in the regulation of membrane traffic[8–11]. There are a variety of different Rab proteins, each one is specific to a cellular compartment, therefore controlling its function and identity[12,13]. Some Rab proteins are ubiquitously expressed, such as Rab1 (found in most cell types), while Rab27a is exclusive to melanocytes and secretion capable cells[13,14].

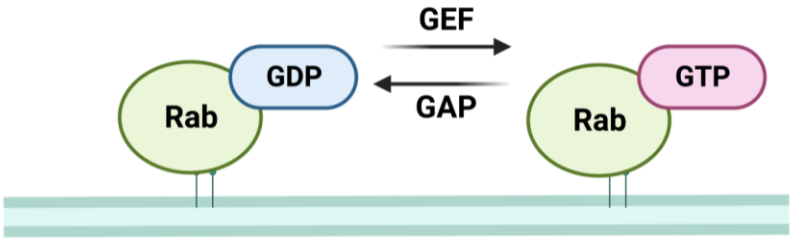

Figure 2. Rab GTPase activation/inactivation cycle. Rab GTPases are activated by guanine nucleotide exchange factors (GEFs) and inactivated by GTPase-activating proteins (GAPs). The activation of Rabs is essential for the regulation of membrane traffic pathways, the GDP-bound Rab can bind to effectors responsible for different functions, such as budding, transport, tethering, and vesicle fusion. Created with BioRender. Adapted from Homma Y, Hiragi S, Fukuda M. Rab family of small GTPases: an updated view on their regulation and functions. FEBS J. 2021;288(1):36–55.

Rab GTPases undergoes different post-translational modifications, one of the most well-known is protein prenylation, denominated by the addition of farnesyl or geranylgeranyl. This modification is necessary to help Rab GTPases bind to membranes. To prenylate Rab proteins, two different mechanisms exist; the classical and the alternative pathway[13].

In the classical pathway, unprenylated Rab proteins bind to Rab escort protein (REP), followed by recognition by Rab geranylgeranyl transferase (RGGT), which catalyses the exchange of geranyl groups to the protein. Finally, through a series of reactions, REP is released and assists the binding of prenylated Rab GTPases to membranes. An alternative pathway has also been proposed, where REP and RGGT first form a complex that then associates with Rab protein, however this seems to be much slower than the classical pathway[13,15], **Figure 3**.

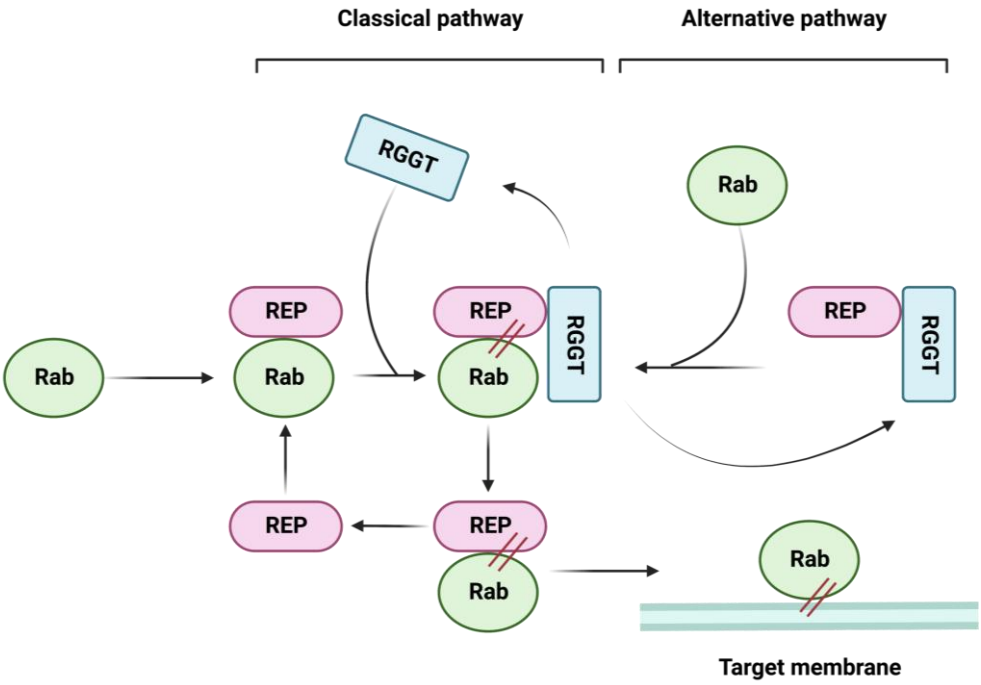

Figure 3. Classical and Alternative pathway for Rab protein prenylation. In the classical pathway, a complex is formed with REP and Rab proteins, and this complex is then recognized by Rab geranylgeranyl transferase (RGGT) which prenylates the Rab protein. In the alternative pathway, a complex is firstly formed between

RGGT and REP, which then associate with the Rab protein. Prenylated Rab GTPases are then able to bind to target membranes. Created with BioRender. Adapted from Leung KF, Baron R, Seabra MC. Thematic review series: Lipid Posttranslational Modifications Geranylgeranylation of Rab GTPases. J Lipid Res. 2006; 47:467–75.

1.1.2. Mechanisms for the uptake from the extracellular space – Endocytosis

For cells to receive the components necessary to maintain cellular homeostasis, they need to uptake from the extracellular environment different sized macromolecules and fluids containing a variety of products. The first step of this process is denominated endocytosis and different types have been described; clathrin-mediated endocytosis (CME) and caveolae-mediated endocytosis (CavME)[16]. CME was first described in 1964[17], using electron microscopy studies, and entails multiple steps, including initiation, where clathrin starts to coat membrane pits, cargo-selection, growth of the clathrin-coated pits, maturation, scission from the membrane, release and uncoating of clathrin[16]. CavME, was also described using electron microscopy studies in 1955, and consists of 50-100 nm sized membrane evaginations, denominated caveolae. In recent years, other mechanisms have been described to mediate extracellular uptake, denominated clathrin-independent endocytosis (CIE)[16,18]. The different uptake mechanisms of extracellular content are represented in **Figure 4.**

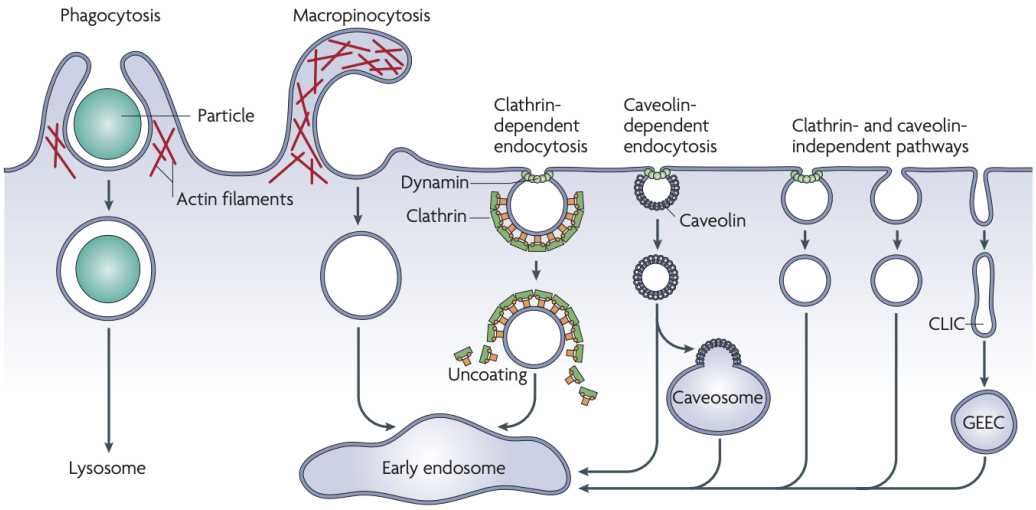

Figure 4. Different pathways of internalization into cells. Phagocytosis is the incorporation of large particles and is mediated by membrane receptors. Macropinocytosis is a bulk non-selective uptake of fluids. Both of these mechanisms have an underlying actin remodelling step. Other mechanisms include clathrin-dependent endocytosis, caveolin-mediated endocytosis, and clathrin-independent pathways. The vesicles formed from phagocytosis and macropinocytosis present the larger size compared to other forms of endocytosis. The pathways converge into the formation of early endosomes. Adapted from Mayor S, Pagano RE. Pathways of clathrin-independent endocytosis. Nat Rev Mol Cell Biol 2007 88. 2007 Aug;8(8):603–12.

Macropinocytosis was the first endocytic mechanisms observed in 1931 and comprises another form of endocytosis, where growth factors are responsible for the activation of this actin-driven form of internalization, and therefore, macropinocytosis is considered a bulk and nonselective form of extracellular fluid uptake[19].

1.1.2.1. Phagocytosis – a specialized endocytosis

Phagocytosis describes a universal process which occurs in almost all cell types; however, some cells are known as professional phagocytes (such as cells in the immune system) and are highly specialized in identifying a foreign organism and carry out its removal. In non-professional phagocytes, such as fibroblasts, epithelial and endothelial cells, these cells retain some phagocytic capacity according to their biological needs[20].

As a definition, phagocytosis is the incorporation of particles with a size larger than 0.5 μm and involves the presence of receptors at the plasma membrane that recognize the soon to be internalized particle. Phagocytosis shares similarities with endocytosis, being considered a type of endocytosis specialized in the uptake of larger particles. The first step is the recognition of the particle by specific membrane receptors, followed by internalization and formation of an early phagosome (EP), the homologous of an early endosome (EE). The EP, just like an EE, fuses with EEs, involving the Rab5 protein, which recruits, early endosome antigen 1 (EEA1) to promote fusion and recruitment of Rab7[21]. Further along the pathway, Rab5 is gradually lost and replaced with Rab7 which mediates the fusion with late LEs to form late phagosomes (LP). These vesicles, acquire a set of characteristics that start mimicking the degradative prone environment of the lysosomes, such as a decrease in luminal pH, addition of cathepsins and hydrolases and acquisition of membrane proteins, including lysosome-associated membrane protein (LAMP). Eventually LP fuse with lysosomes, creating a hybrid known as phagolysosome[20], **Figure 5**.

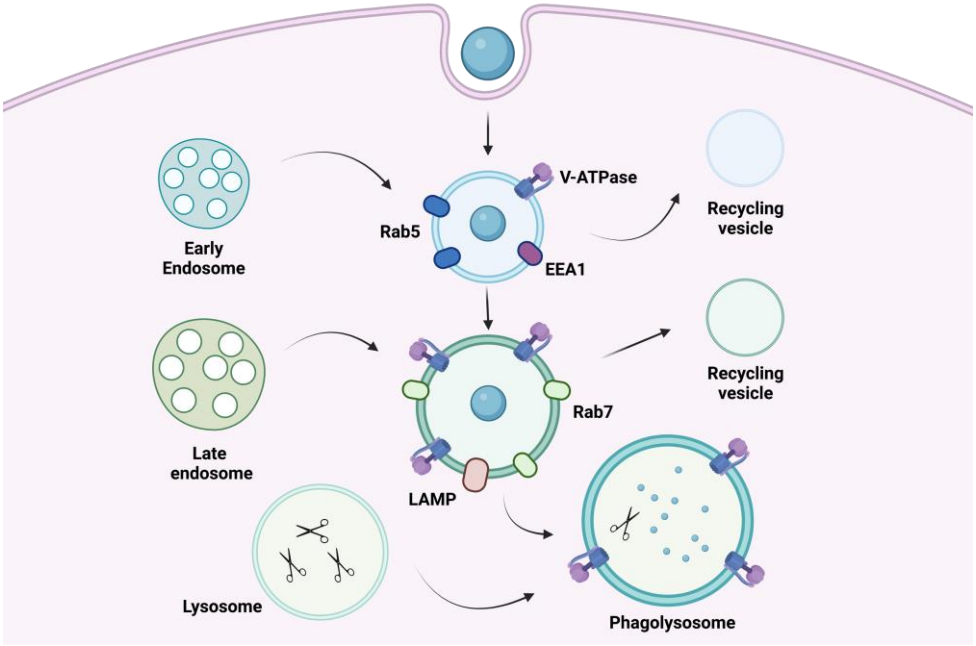

Figure 5. Phagocytosis and the phagosome maturation pathway. Particles are incorporated within the cell into early endosomes, forming early phagosome which matures into late phagosomes which fuse with lysosomes to form the phagolysosomal structure. The transformation of early phagosomes into late phagosomes is characterized by an exchange between Rabs, such as Rab5 into Rab7. The phagolysosome has an acidic environment due to the presence of proton-pumping V-ATPases, as well as a set of different enzymes to carry out the degradative capacity of the phagolysosomal structure, such as cathepsins. Created with BioRender. Adapted from Kishore U, Grinstein S, Sørensen Dalgaard T, Rosales carosal C, Uribe-Querol

E, Rosales C. Phagocytosis: Our Current Understanding of a Universal Biological Process. Front Immunol.2020;1:1066.

1.1.3. Endosomal traffic

After internalization, vesicles containing cargo, receptors and mediator proteins, enter the endosomal system, a complex and effective network where vesicles travel on microtubules between different cell compartments[16]. After uptake from the extracellular environment, independently of the type of endocytosis, all endocytic cargo targeted for degradation culminates in the EEs[12,16]. EEs can fuse with other EEs by both homo- and heterotypic fusion, regulated by a complex set of proteins that include soluble NSF (N-ethylmaleimide sensitive factor) attachment receptors (SNAREs). Regardless of fusion type, this process seems to be regulated predominately by the Rab5 protein[12,22]. Rab5 is present since the formation of EEs until their maturation, being part of the conversion to late endosomes[23]. The components of these vesicles can have different fates: recycle back to the plasma membrane, reach the Golgi network, or be signalled to the lysosomes for degradation[16]. While moving along the pathway, early endosomes start to mature into different vesicles, each one with its own identity, a process tightly regulated by multiple proteins of the Rab family.

1.1.4. Recycling of endocytosed vesicles

Given the large amount of membrane that is incorporated within the cell when cargo is endocytosed, it is of extreme importance to recycle key components back to the plasma membrane, such as receptors, while the ligands are further proceeded along the endo-lysosomal pathway. This process is thought to be regulated by the small GTPase Rab4 by a direct and rapid recycling pathway or by Rab11, an indirect recycling pathway[12].

1.1.5. Endosome maturation

The maturation from EEs to LEs is mediated by specific molecular changes, one of the most evident is the decrease in pH from around ~6.2 in EEs to ~5.5/5.0 in LEs and the increase of vesicular area. EEs start accumulating intraluminal vesicles (ILVs) and through a series of inward membrane evaginations, which then detaches from EEs and become free multivesicular bodies (MVBs). These MVBs can then fuse with LEs[12,24]. At this point, LEs have two main routes for further maturation, they can either continue in the endo-lysosomal pathway and fuse with lysosomes or fuse with the plasma membrane and release the ILVs into the extracellular space, termed exosomes[12], **Figure 6.**

The switch from EE to LE is known as Rab5 to Rab7 conversion or Rab switch, a process that occurs on the membranes of MVBs. This conversion is crucial for a well-defined border between EE and LE[12]. Before a new LE arises, Rab7 needs to be recruited by Rab5 to the EE, forming a transient form denominated hybrid Rab5/7 endosome. The form by which the new LEs separate themselves from the hybrid forms remains unclear, but there are two theories. The first entails a Rab5 conversion to its inactive form followed by a vesicle dissociation and the second a fission between the LEs positive for Rab7 from the hybrid endosome[23,25].

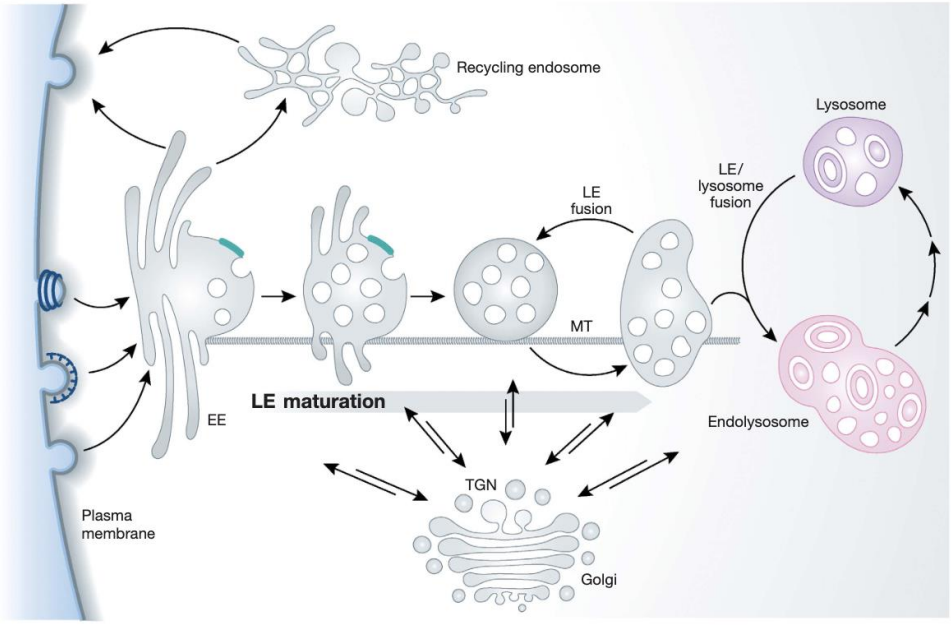

Figure 6. Pathway of endosome maturation. The pathway begins with the incorporation of extracellular contents into early endosomes, which can be recycled back to the plasma membrane. Early endosomes can mature into late endosomes by incorporating the contents of early endosomes and newly synthetized lysosomal hydrolases. Late endosomes present a higher size and accumulate intraluminal vesicles by various fusion events with other late endosome vesicles. Late endosomes can then fuse with lysosomes forming a hybrid organelle, the endolysosome, where extracellular components are degraded. Adapted from Huotari J, Helenius A. Endosome maturation. EMBO J. 2011 Aug 31;30(17):3481–500.

After the switch and the formation of a new LEs, the process of maturation continues. These changes include a shift to the perinuclear region, further alterations of membrane components, decrease in luminal pH and acquisition of lysosomal traits, such as hydrolases, inhibition of fusion with EEs and increase in size[23]. The acquisition of lysosomal features requires the presence of a membrane strong enough to sustained the presence of acid hydrolases, and this is achieved by the acquisition of lysosomal-associated membrane proteins 1 (LAMP1) and 2 (LAMP2)[23].

1.1.6. Late endosome/lysosome – the undistinguishable vesicles

To this day, no exclusive molecular difference between LEs and lysosomes have been described, meaning that no lysosome marker is also not found in LEs. Both vesicles present the most common markers, LAMP1 and LAMP2. However, it is still possible to distinguish both vesicles by structural methods[12]. LEs have a diameter of 250-1000 nm and the lumen contains a diverse set of ILVs with a diameter of 50-100 nm[23].

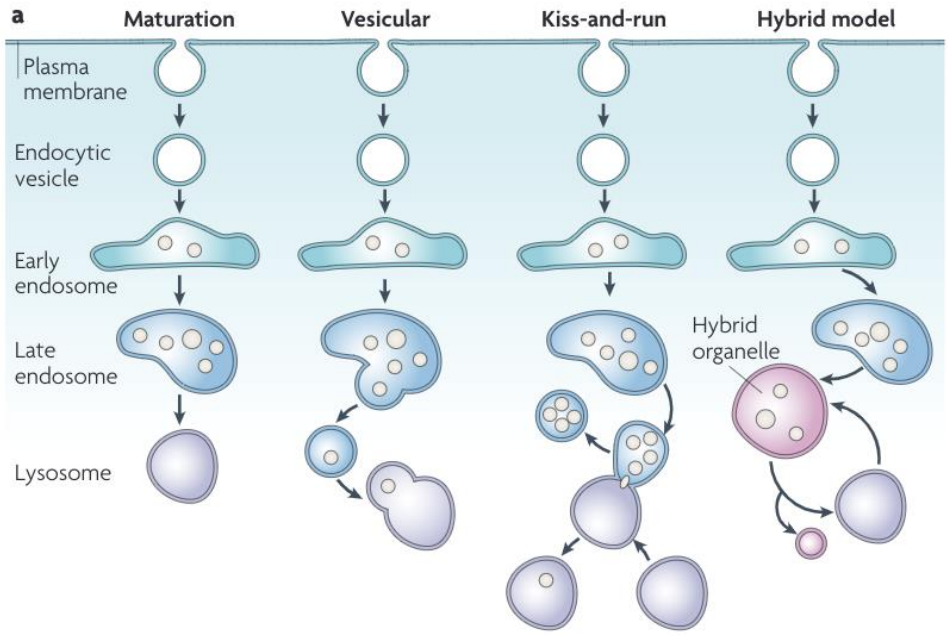

Figure 7. Different models of late endosomes and lysosomes fusion. After endocytosis and vesicle maturation, late endosomes are produced, and the internalized cargo is delivered to the lysosomes. Different possibilities have been proposed to explain how late endosome and lysosome fusion occurs. The first model proposes a gradual maturation of late endosomes into lysosomes, where lysosome characteristics are acquired, and late endosome are lost. The second is the vesicular model, where vesicles erupt from the late endosome that then fuse with lysosomes. In the third model, both late endosomes and lysosome move towards each other exchanging components and then move away (kiss-and-run movements). The last model, termed the hybrid model, entails a fusion between late endosomes and lysosomes creating a hybrid structure. Adapted from Luzio JP, Pryor PR, Bright NA. Lysosomes: fusion and function. Nat Rev Mol Cell Biol 2007 88;8(8):622–32.

Different models have been proposed to explain the fusion between LEs and lysosomes, using techniques such as immunoelectron microscopy in early studies as well as live-cell confocal microscopy, as described in **Figure 7**. The first model entails a maturation of late endosomes into mature lysosomes by acquiring lysosomal characteristics, such as decrease in pH and acid hydrolases. The second, defends the existence of small vesicles that travel between the two compartment to deliver content from LEs to lysosomes. The third, was denominated kiss-and-run, LEs temporarily fuse with lysosomes. Lastly, the hybrid model defends the fusion of both LEs and lysosomes to form a hybrid vesicle containing features of both vesicles[26].

1.1.7. Lysosomes – much more than a degradation hub

Lysosomes were first described in 1955 by Christian de Duve[27] as intracellular spots full of enzymatic species and later found to be membrane enclosed organelles. Since then, lysosomes have been known to be degradation endpoints for a variety of molecules from both intracellular and extracellular space[28]. Mammalian cells are enriched in this organelle, with numbers raging from 50-1000 lysosomes per cell, depending on the cell type. In recent years, lysosomes have been shown to have new and important functions, such as metabolic signalling, gene regulation, immunity, plasma membrane repair, cell adhesion and migration[29].

Aging is defined by the World Health Organization (WHO) as the accumulation of several molecular and cellular damages over time, increasing the risk of developing several diseases[30]. Different hallmarks have been appointed as causes for aging, one of them is a decrease in proteostasis efficacy. To have correct proteostasis, healthy proteome, proteins need to be degraded with high efficiency through the many pathways available, one of the most important being, the autophagic pathway, that utilizes the degradative capacity of lysosomes. Therefore, lysosomes are constantly challenged in the clearing of non-essential material, and many conditions have been described to have as an underlying cause lysosome dysfunction; thus it is of great importance to uncover new methods to manipulate lysosomal function to maintain correct cellular homeostasis[31].

A few diseases also have their origin in lysosome dysfunction. One of the most well-known of these diseases are the lysosome storage disorders (LSDs), which are a family of conditions whose aetiology are inherited genetic mutations in genes essential for lysosomal homeostasis. Examples of LSDs are Niemann-Pick disease type C1 (NPC1) and Pompe disease, which lead to an accumulation of cholesterol in the liver and glycogen in skeletal muscle, respectively[32].

1.2. The retina

The retina is composed of many layers and is responsible for focusing the light that enters the eye. This light is then converted into electric signals that move through the optic nerve and are focused on the visual part of the brain. Given the many layers present in the retina, a variety of cell types are found in this complex structure, including two types of photoreceptor cells (rods and cones), horizontal cells, bipolar cells, amacrine cells and ganglion cells that compose the nerve layer[33,34], as represented in **Figure 8**.

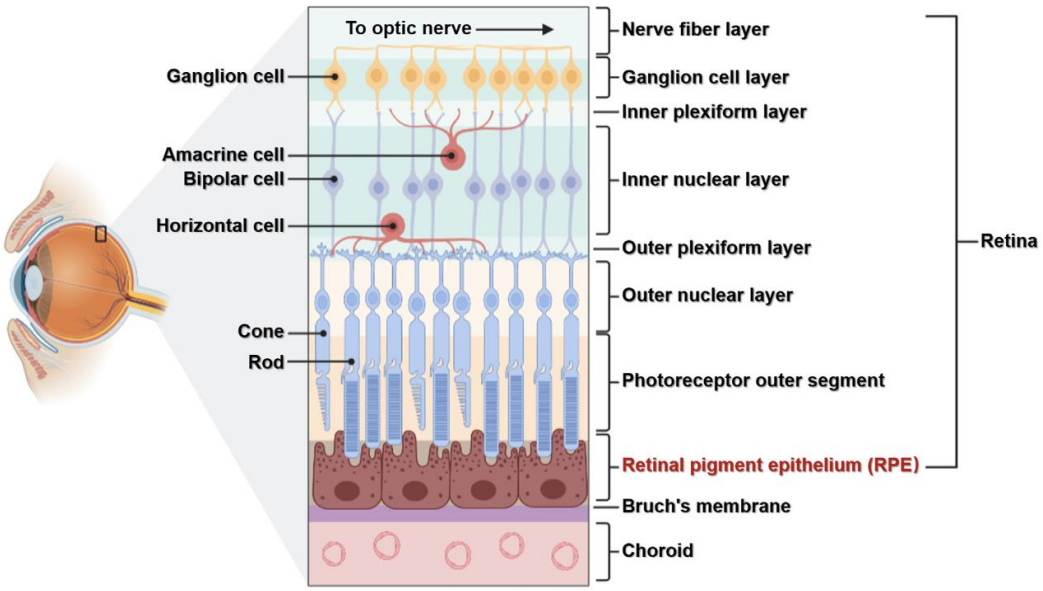

Figure 8. The structure of the eye retina. The retina is composed by many different layers and cell types, such as ganglion, amacrine, bipolar, horizontal and photoreceptor cells, which comprise the neural retina. The retinal pigment epithelium (RPE) is a nonneuronal cell type that forms a tight monolayer which contacts the choroidal vasculature through the Bruch's membrane. Adapted from Yang S, Zhou J, Li D. Functions and Diseases of the Retinal Pigment Epithelium.

1.2.1. Retinal pigment epithelium (RPE)

The retinal pigment epithelium (RPE) is one of the many layers present in the retina and consists of a tight single cell monolayer[2,33,35]. It is located between the photoreceptors and the choroidal vasculature. It is a post-mitotic polarized epithelia with a diverse set of crucial functions for a healthy vision. The basolateral side of the RPE is in contact with the Bruch's membrane and the choroid where nutrients, oxygen, glucose, toxic waste, and other substances are exchanged and distributed to and from the upper layers of the retina. The apical side of the RPE is responsible for the essential clearing of photoreceptor outer segments (POS) shed from the photoreceptors, a process that is performed daily by the RPE to renew the visual cycle products[2,33–35]. Other essential functions of the RPE include, renewal of retinoic acid (vitamin A) as well as maintaining a tight blood-retinal barrier[2], **Figure 9.**

Given its localization and importance in the maintenance of a healthy vision, many diseases have their basis in RPE alterations or functional impairment, such as retinitis pigmentosa (RP), age-related macular degeneration (AMD) and Stargardt disease (SD)[33,36,37].

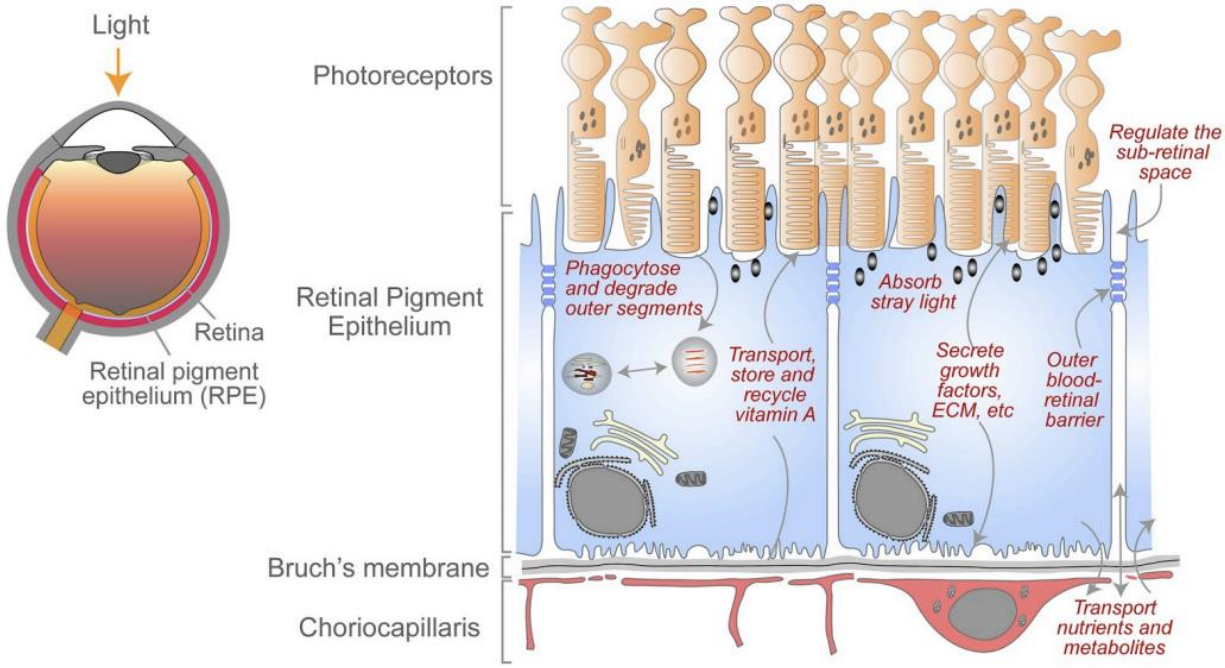

Figure 9. Functions of retinal pigment epithelium (RPE). RPE is responsible for the phagocytosis and degradation of photoreceptor outer segments (POS) to maintain a healthy visual cycle. RPE is also responsible for the transport, storage, and recycling of retinoic acid (vitamin A), as well as secretion of growth factors. The positioning of the RPE in the retina, below photoreceptors and above the choroidal vasculature, makes this cell type essential for the transportation of nutrients and metabolites. Adapted from Lakkaraju A, Umapathy A, Tan LX, Daniele L, Philp NJ, Boesze-Battaglia K, et al. The cell biology of the retinal pigment epithelium. Vol. 78, Progress in Retinal and Eye Research. Elsevier Ltd; 2020. p. 100846.

1.2.2. Photoreceptors

Photoreceptors are light sensitive cells located above the RPE. Just like the RPE, many diseases also include disfunctions of photoreceptors, such as Leber's Congenital Amaurosis (LCA), RP and AMD[36–39]. There are two different types of photoreceptor cells, rods, and cones, each one with its own role in visual function.

The cones are responsible for the majority of human vision, while rods are required under specific conditions, such as low light, also known as scotopic vision. Nonetheless, rods still contribute to 95% of all photoreceptors found in the human retina[40]. POS are a set of membranous discs enriched in opsins, integral membrane proteins which are light sensitivity due to the presence of the chromophore rhodopsin. When light enter the eye, it is focused on the neural retina, more specifically on photoreceptors, where rhodopsin suffers a bleaching reaction triggering the visual transduction pathway. With time and continuous light exposure, new discs are produced, and the old ones shed from the extremity of the photoreceptors[34]. The old discs are enriched in phosphatidylserine (PtdSer), which is essential for a correct recognition by the RPE[34].

1.2.3. Interaction between RPE and photoreceptors

Besides the phagocytosis of POS, RPE and photoreceptors interact by the bidirectional exchange of substances. One of the most important is the visual cycle, also known as retinoid cycle, represented in **Figure 10**. When rhodopsin in photoreceptors receive external light stimulus, the 11-cis-retinal is transformed into all-trans-retinal, which activates rhodopsin. Through a series of reactions involving different enzymes, all-trans-retinol is liberated from photoreceptors and taken up by the RPE. In the RPE, re-isomerization occurs with the help of chaperone proteins, such as RPE65. After isomerization, 11-cis-retinol is oxidized into 11-cis-retinal, which is then transported back to photoreceptors, a mechanism that remains poorly understood[41–44].

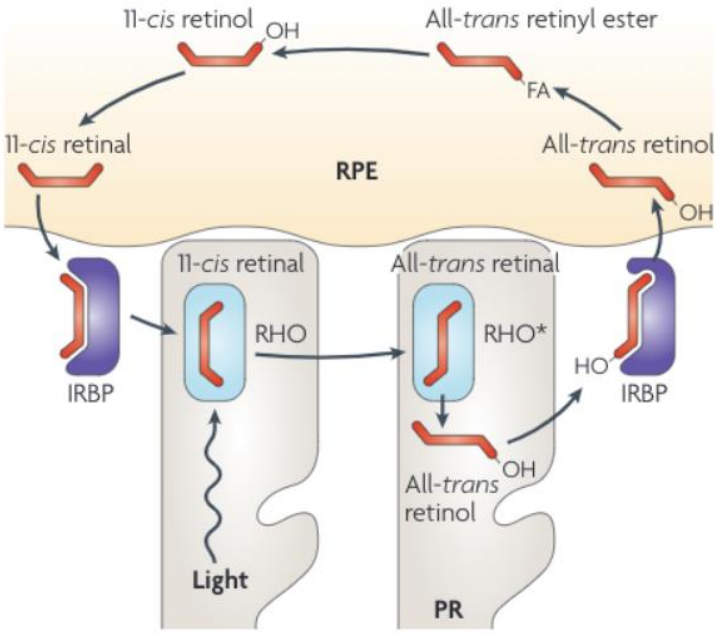

Figure 10. The visual cycle. Pathway that recycles retinoids used in light absorption in photoreceptor cells. Upon light exposure rhodopsin (RHO) is activated by the isomerization of 11-cis-retinal (present in the RHO molecule) to all-trans-retinal. This isoform unbinds from rhodopsin and binds to plasm membrane and is transported to the cytoplasm. A retinol dehydrogenase converts all-trans-retinal into all-trans retinol. This form is transported to the retinal pigment epithelium (RPE) where lecithin retinol acyltransferase (LRAT) esterifies all-trans-retinol into all-trans retinyl ester. The formed ester undergoes an isomerization into 11cis retinal and transported back to the photoreceptors, where it binds rhodopsin. Adapted from Wright AF, Chakarova CF, Abd El-Aziz MM, Bhattacharya SS. Photoreceptor degeneration: genetic and mechanistic dissection of a complex trait. 2010

1.2.3.1. RPE phagocytic capacity and the visual cycle

RPE are considered tissue resident specialized phagocytic cells that recognize POS from the adjacent photoreceptors with the objective to remove oxidized POS and regenerate visual cycle products[45]. Each RPE cell oversees the maintenance of around 30 photoreceptors and the phagocytic process involves three distinct steps; the first is the binding to POS, the second being the endocytosis of the soon-to-be degraded POS and lastly, their degradation[33,34]. Each day about 7-10% of POS are degraded by the RPE, meaning that in 2 weeks the elimination of all POS is achieved[34].

The phagocytosis of POS starts with the ensheathment of POS by the RPE microvilli. This step is followed by binding to MerTK receptors from the tyrosine kinase family, found on the membrane of RPE. This binding induces the activation of several proteins in a cascade of events that promote actin polymerization. Given the large amount of contact that each RPE cell has with photoreceptors, one cell engulfs at least 30 targets at once. The MerTK receptor also actives the PI3K pathway to ensure synchronized POS phagocytosis to avoid continuous polymerization/disassembly of actin[34]. On the membrane of RPE, $\alpha v\beta 5$ integrins are found to be activated following MerTK activation, therefore promoting the initiation of phagocytosis by MerTK[2,34,45], **Figure 11**.

The phagosomes formed are reported to have a size of 1-2 μm diameter and upon entering the RPE cells, a series of fusions and maturation events occur. With maturation, phagosomes start to acquire lysosomal characteristics, such as V-ATPases and enzymes. Rab5 is present in EPs and recruits EEA1. During maturation, Rab5 is gradually lost and substituted by Rab7, promoting fusion with lysosomes and the inward movement of vesicles, and the acquisition of LAMPs, markers of LP[34].

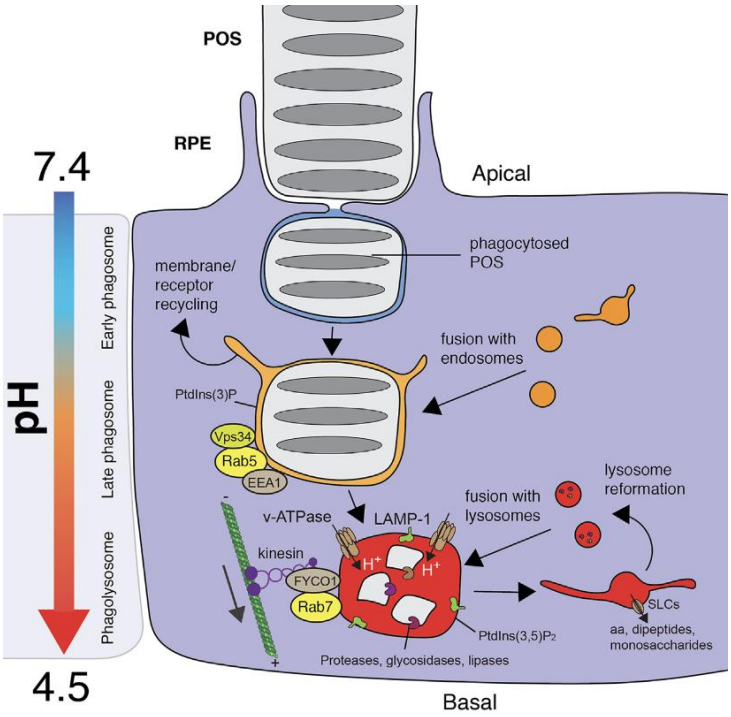

Figure 11. Photoreceptor outer segments (POS) phagocytosis and degradation. POS are phagocytosed into early phagosomes which go through a series of maturation steps into late phagosomes and finally fusion with lysosomes. The maturation process is regulated by different Rab GTPases and the movements along

microtubules with a switch in Rab5 to Rab7. Additionally, a drop in pH Is also achieved, as well as activation of enzymes that include proteases, lipases, and hydrolases. In the phagolysosome, phagocytosed POS are degraded. Adapted from Kwon W, Freeman SA. Phagocytosis by the Retinal Pigment Epithelium: Recognition, Resolution, Recycling. Front Immunol. 2020 Nov 13;11:2985.

One of the most important steps is the proper acidification of the lumen of phagosomes due to the activity of V-ATPases, proton pumps that rapidly acidify the luminal region using the energy from ATP. Although this process is observed in the RPE, its molecular mechanisms remain largely unknown. This acidification is crucial for the correct functioning of hydrolases, whose activity is dependent on low pH. Studies where V-ATPases were ablated, POS digestion was inhibited, resulting in swollen phagolysosomes full of undegraded materials. With time, toxic material starts accumulating between the RPE and choroid, called drusen, a pathological observation in AMD[34].

Concomitantly to phagosome acidification, its content is degraded by enzymes present in phagolysosomes, such as proteases, glycosidases, and lipases. Incorporated POS are thought to be composed of around 70% glycosylated opsin and 30% lipids. The enzymes responsible for the degradation of proteins into peptides and aminoacids are cathepsins, the most abundant being cathepsin D. This specific protease is highly expressed in RPE, and its absence is responsible for the accumulation of undigested POS[46]. Not all POS contents is degraded in the lysosome, for example, cholesterol present in POS is transported to the Golgi, endoplasmic reticulum or plasma membrane to be recycled back to photoreceptors[34].

In healthy RPE, an accumulation of highly oxidized proteins (30-70%), lipids (20-50%), sugars and metals (2%), create what is known as lipofuscin, a post-mitotic "age pigment"[34,47,48]. With time and the continuous burden of phagocytosis, RPE exponentially accumulate lipofuscin granules and given the post-mitotic state of RPE, the impairment in the resolution of lipofuscin is at the source of several retinopathies[34,48]. Given its nature, lipofuscin cannot be degraded, so it accumulates inside lysosomes and the cytoplasm in post-mitotic cells, such as the RPE[47]. Besides the RPE, lipofuscin granules are also known to accumulate in heart, skeletal muscle and neuronal cells, contributing to the development of neurogenerative diseases[47,49–51].

1.3. Choroideremia: a rare condition

Choroideremia (CHM) is a monogenic X-linked form of retinal degeneration with a recessive hereditary pattern and is to this day an incurable rare retinopathy[52,53]. The *CHM* gene is composed of 15 exons and encodes a 653 aminoacid protein[54,55]. CHM was first described by the Austrian ophthalmologist Ludwig Mauthner in 1872[56,57]. Given its X-linked aetiology, CHM has a prevalence of 1 in 50 000 male individuals. It is characterized by a progressive degeneration of three of the most important layers in the retina; choroid, photoreceptors and RPE[52,54,56,58–60].

Clinically, CHM manifests in the first decade of life with night blindness and a decrease in the visual field, symptoms that gradually progress into loss of peripheral vision which inevitably leads to legal blindness around the fifth or seventh decade[15,56,58–60]. At the molecular level, there is no consensus in the order of retina layer degeneration; evidence seems to point to an initial RPE degeneration concomitantly with

photoreceptor degeneration followed by choroid layer atrophy, while others defend the opposite with primary photoreceptor degeneration followed by RPE and choroidal atrophy[15,56,58,59]. Females can be carriers with the majority being asymptomatic, however, in rare cases, affected females can present different degrees of RPE degeneration, possibly due to random X-chromosome inactivation, similar to CHM in male patients[15,56,58–60].

1.3.1. Genetic background of CHM

Monogenic mutations, of which 280 have been identified on the *CHM* gene located on chromosome X at position q21.2, may have different origins, such as translocations, point mutations, sequence variations, deletions, insertions, nonsense, and frameshift. The last two mutations are responsible for around 70% of the mutations found in *CHM,* another 30% are due to splicing impairments. Despite the wide variety of mutations that can occur on the *CHM gene*, most are null mutations, meaning that the REP1 protein produced can be truncated and therefore not functional, as well as fully absent[15,53,56,58–60].

1.3.2. CHM pathophysiology

The *CHM* gene encodes for the Rab escort protein 1 (REP1), which is essential for the correct prenylation of Rab GTPases as mentioned above, and therefore a key regulator of membrane traffic in RPE cells[15,58,61]. REP1 protein is ubiquitously expressed and guides Rab GTPase proteins to the catalytic site of RGGT enzyme for the prenylation reaction, followed by transportation of the newly prenylated Rab to the target membrane [15,59,60,62].

The molecular effect of REP1 absence in RPE cells remains poorly understood. One of the most important functions of the RPE relies on the phagocytosis and degradation of shed POS, a process largely dependent and regulated by Rab proteins[60].

Through the years different studies have pointed to key molecular defects in CHM deficient cells. One study showed that in both zebrafish and mouse models, undigested phagocytosed POS accumulate, and an impairment in the transport of melanosomes along the RPE was observed[56]. In 2009, Strunnikova et.al demonstrated that in peripheral cells (fibroblasts and monocytes) from CHM patients, lysosomes show an increase in pH, a reduced rate of proteolytic degradation and a change in the pattern of cytokine secretion[63]. The following year, RPE cells silenced for the *CHM* gene revealed a reduction in the acidification of POS-containing phagosomes as well as a decrease in POS clearance. No changes were seen in the capacity to internalize POS. Additionally, there was a decrease in the interaction of POS-containing phagosomes with late endosome markers, such as Rab7 and LAMP1[64]. Three years later in 2013, Wavre-Shapton and colleagues developed a mouse model of CHM to study the *in vivo* alterations resulting from REP1 absence in the eye. The study revealed an accumulation of granules of lipofuscin and melanolipofuscin inside RPE cells, with an increase in the thickening of Bruch's membrane in the extracellular environment. Moreover, the number of melanosomes in the apical side of the RPE was decreased, proving that REP1 indeed has a role in the movement of melanin containing granules to the apical side of RPE cells, which is dependent on the function

of Rab27a. Although both pathways reveal dysfunction, some melanosomes do reach the apical side and some POS are degraded, meaning that the absence of REP1 causes only a partial dysfunction[65–67].

Further studies uncovered a *CHM-Like* (*CHML*) gene, present on chromosome 1q42, which encodes REP2, a REP1 homologue with 90% similarity and that is ubiquitously expressed. In every tissue, except the eye, the absence of REP1 is compensated by REP2, meaning that the CHM phenotype observed in the RPE is not just due to the absence of REP1 but also due to the inability to be compensated by REP2. Furthermore, there are varying degrees of affinity between Rab proteins and REP1/REP2, specifically it is known that Rab27a which has a key role in the retina, is preferentially prenylated by REP1 over REP2, explaining some of the tissue specific compensation[54,56,57,60,66,68].

1.3.3. Treatments available for CHM

In the last decade, many advances have been made in order to better understand CHM, as well as to uncover new therapies. Being CHM a form of inherited retinal disease (IRDs), researchers are focused on six main paths of treatment, **Figure 12** [69].

The first is based on gene therapy with the objective to recover REP1 expression by employing vectors such as natural adeno-associated virus (AAVs), next generation AAVs vectors or non-viral vectors, to reduce the immune response of viral vectors. One of the most common developments is the use of AAVs as a means for gene therapy[58,59]. In 2014, the first clinical trial employing gene therapy for CHM resulted in an increase in visual acuity 6 months after treatment[1,58]. However, there are still many challenges using gene therapy as a treatment for CHM; currently only patients in later stages of the disease are being accepted into clinical trials meaning that the effect of AAV gene therapy are still not known for early stages of CHM[58,69].

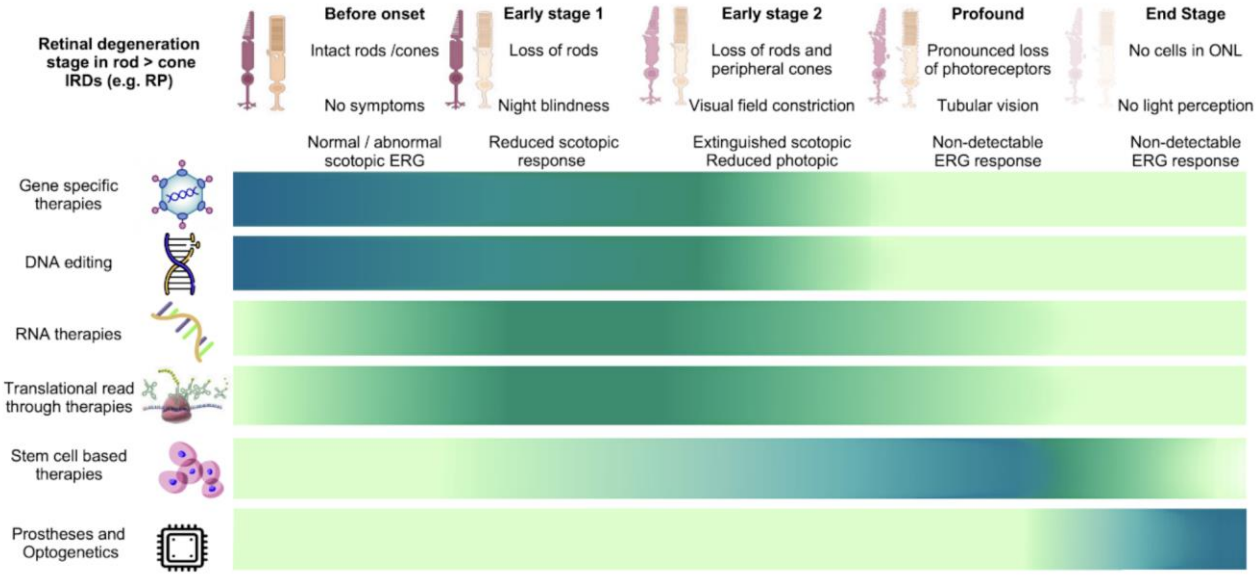

Figure 12. Evolving therapies on Inherited Retinal Diseases (IRDs). Current research has been focused in six different paths of therapies, each with its preferential target stage of disease. 1) Gene specific therapies. 2) DNA editing strategies making use of the CRISPR/Cas9 technology for early stages of disease. 3) RNA therapies which intend to ameliorate the permanent effects of DNA editing. 4) Translational read through therapies that aim to misread the premature codon and produce a functional protein, a strategy that can be used in the final period of the early stages. 5) Stem cell-based therapies which can be employed in late stages

of disease. 6) Prostheses and optogenetics therapies that are focused on restoring visual defects in end-stage patients. Adapted from CureCHM – Choroideremia Research Foundation.

The second approach is based on genome editing by making use of CRISPR/Cas9 technology, however this method is still being tested for its safety and effectiveness in the treatment of human diseases. Nevertheless, DNA editing is permanent and can have side-effects, so researchers are also focusing on RNA editing techniques, which are reversible and low-cost compared to DNA editing[69,70]. The fourth approach is based on therapies focused on the premature stop codon in RNA by inducing a translation readthrough of the premature stop codon using pharmaceutical compounds, by promoting misreading of the premature stop and the incorporation of a similar aminoacid to create REP1 protein, however this therapy still poses many risks and its efficiency is still being tested[69,71].

In recent years, human induced pluripotent stem cells (hiPSc) have been gaining a lot of attention as models to study several diseases, such as choroideremia, further explored in the next section. Besides the use of hiPSc in research to better understand the mechanisms underlying human diseases, they are also being used as treatment, as hiPSc can be harvested either from a healthy donor or a patient, differentiated into any cell type such as RPE, grown as a scaffold layer and transplanted into the eye of patients. However, this technique is still very challenging and costly[69,72].

The final approach is focused on manipulating light perception in the brain in order to overcome visual effects of CHM and other IRDs using prosthetics and optogenetics. The prosthetics are microchips that can be implanted in the eye, absorb light, and converts into signals that are sent through neurons to the brain, however there are still limitations based on the temperature these chips reach that limit the number of signals[56,69]. Optogenetics employs gene therapy to modify retinal neurons by inducing the expression of a light responsive protein, such as rhodopsin. Currently, the images and light being sent to stimulate these neurons is controlled using a special glass that convert images or video into a code and neurons send these coded signals to the brain. This approach is gaining more attention since researcher believe that such approach could potential cure the blindness caused by CHM[69,73].

1.4. Models to study the retina layers – a focus on the RPE and CHM pathophysiology

1.4.1. *In vivo* models for CHM

To better understand the molecular mechanisms underlying retinal conditions, a suitable model needs to be employed. Currently, a diverse span of models has been developed from *in vivo*, *in vitro* to *ex vivo*. Before describing the current best models, it is important to consider that, despite the set of advantages a model has it never fully reproduces the human eye, the retina, and its connections at both molecular and cellular level. Specifically for the eye, the animal models available have limitations, since mouse eyes have a clear size difference, optical properties, as well as cellular distribution[74,75]. The model that most closely resembles the anatomy of the human eye belongs to primate models, followed closely by porcine eyes, which share size, morphology and function with the human retina[74,76]. It is also possible to produce primary RPE culture from porcine eye explants and, given the size of the pig eyes, more than one culture can be set up

with each isolation procedure, greatly reducing the need for a large numbers of animals and the availability of freshly extracted eyes from available slaughterhouses[74,77–79]. Regarding the use of mouse models, it is by far the most used animal model in biomedical research due to their short reproductive cycles and easily genetic manipulation[74,80–82].

In 1997, van den Hurk and colleagues developed an animal model for CHM, a mouse where REP1 gene was mutated in exon 8 resulting in the addition of a premature termination codon, a nonsense mutation. The expression product, if expressed, was tested for its ability to prenylate Rab protein GTPases, and results showed that REP1 proteins lacking 70 C-terminal amino acids were inefficient in guiding the geranylgeranylation of Rab GTPases and thus non-functional. However, affected males were not viable, a significant difference from what happens in human which may indicate differences in the prenylation systems between mice and humans. Examination of carrier females revealed a loss of photoreceptors in the retina of the modified mice, thus indicating that the absence of REP1 somewhat contributes to photoreceptor degeneration[83]. Ten years later, a zebrafish model of CHM was developed by Krock et al. Evidence showed that absence of REP1 led to impairment in the maturation of melanosomes and the degradation of POS accompanied by a degeneration of both RPE and photoreceptors. However, since REP2 is not expressed in zebrafish, the absence of REP1 is more pronounced and severe than in human CHM[84].

In 2010, a different model of CHM arose, based on cell-type specific knockout mouse, where a mouse line with a conditional allele *Chm*^{Flox} was crossed with a transgenic line to achieve a full CHM knockout specific to the RPE cells. Results revealed defects in photoreceptors and RPE, with evidence pointing to an accelerated photoreceptor degeneration when RPE is already compromised[85]. The same model was used in a 2013 study, which resulted in decreased numbers of melanosomes in the apical side of RPE cells as well as an impairment in phagosome degradation. Additionally, in 6-months, the RPE acquired age-related changes, such as accumulation of lipofuscin granules, as well as extracellular accumulation of deposits, which contribute to a better understanding of AMD pathogenesis[67].

Although animal models present a great set of advantages in research, such as proximity to humans and systemic input, measures have been taken to reduce the use of animals in research, with the aim to eliminate the need of mammals by the year of 2035, according to the United States environmental protection agency (US-EPA)[74]. Additionally, despite the advantages that animal models present, they are not ideal models to mimic human diseases. For example, a study using genetically engineered mice to model Parkinson's disease showed that despite genetic mutations mice did not show key Parkinson's features, such as trembling and rigidity in body movement. Other examples regarding Alzheimer's disease, where genetic mouse models' brains were analysis, the hallmark amyloid plaques were missing.[86] So, more often than not, depending on the biological problem, animal models pose more constraints than benefits and scientists find themselves using *in vitro* models.

1.4.2. *In vitro* models for CHM

So, to overcome the constraints in the use of animal models, researchers developed RPE cell cultures models, from the simplest to the more complex. One of the most common is the use of immortalized cell lines, namely ARPE-19. It was produced from a 19-year-old donor, is an epithelial model showing no signs of pigmentation. This cell line is an advantage when a high yield is necessary and cellular pathways are being investigated[74,87,88].

Besides the RPE, other cell lines have been developed to target specific cells from the retina, such as 661W cell line that resembles cone photoreceptors and RGC-5 which mimics ganglion cells, established in 2001. However, in 2013 the RGC-5 cell line was demonstrated to not express key retinal ganglion cell markers and all studies involving this cell line were reconsidered. The MIO-M1 cell line is used to study Müller cells[74,89–92].

If the aim is to better study what happens in the human retina, then primary cells are often a better choice over immortalized cell lines. Contrary to ARPE-19, primary RPE cultures present several characteristics of RPE cells in the human eye, such as polarization and pigmentation, however the retrieval of these cells remains a big obstacle since the prolonged *in vitro* growth of these cells induces dedifferentiation into mesenchymal tissue, with a loss of pigmentation[74,93–96]. Recently, the use of stem-cells derived cultures have been gaining more interest, with the use of human embryonic stem cells (hESCs) and human induced pluripotent stem cells (hiPSc). The production of hiPSc cells from somatic cells, such as fibroblasts, peripheral blood cells and urine is achieved by expression/repression of genes to acquire a pluripotent state. Then, hiPS cells can be differentiated into a wide variety of cell types. For instance, hiPSc cells can be differentiated into beta islet cells of the pancreas to treat diabetes. The use of hiPSc is currently more well accepted than hESCs given ethical issues and the possibility to use patient cells[74,97–105].

Gordiyenko et al. used human fetal RPE (hfRPE) treated with siRNA for the knockdown of REP1 expression and assessed the effects in both phagocytic and secretory pathways in RPE cells. Results pointed to a difficulty in phagosomal acidification, accumulation of POS, as well as a decrease in the interaction between phagosomes containing POS and late endosome markers, such as LAMP1 and Rab7[64].

Cereso et al. used fibroblasts from patient with CHM, which were reprogrammed into induced pluripotent stem cells (iPSCs), which were later differentiation into RPE. The cell model was challenged with two different AAVs gene therapy methods, AAV2/2 and AAV2/5, the latter showed higher expression levels than the ones achieved with AAV2/2, proving that hiPSc-RPE represent a good model to reduce the use of animal models but still maintain the proximity to human RPE[106]. A recent study from 2018, also produced hiPSc-RPE from somatic patient cells and tested for different CHM-related phenotypes, such as prenylation capacity of Rabs, phagosomal degradation capacity (by using pHRODO Bioparticles to mimic phagocytosis), which was shown to be reduced as well as an impairment in membrane traffic in RPE cells[107].

One of the most important functions of the RPE in the retina is to form a tight epithelial monolayer exerting a blood-retina barrier to control both the influx/efflux of a variety of substances. The transepithelial

electrical resistance (TER) is employed to measure the flow of ions across the epithelial cells, increasing proportionally with cell barrier effectiveness Higher levels of TER mean stronger polarization, higher confluency and tight junction between cells, all key characteristics of healthy RPE. Therefore, it is important that cultures of RPE cells acquire a good value of TER. The human retinal RPE achieves about 150 W cm^2, with cultured RPE ranging from 25-500 W cm^2 [108]. However, immortalized cultures tend to achieve only low values of TER, suggesting that their barrier function is not as strong as with primary cells. Nonetheless, TER values in hfRPE reach higher levels than expected since fetal RPE have higher TER than adult RPE[2]. Thus, to choose which model is best to answer each biological questions relating to RPE biology, it is important to consider the advantages/disadvantages that each model presents.

1.5. Hypothesis and objectives

In CHM, the absence of REP1 leads to a reduction in the overall prenylation state of Rab GTPases, specially Rab27a[109]. Current evidence from different models of CHM suggest a reduced rate of proteolytic degradation with an accumulation of undegraded POS, increase in lysosome pH with no changes verified in POS internalization[56,63–67].

Given the role of Rab GTPases in the endocytic-lysosomal pathway and the observations mentioned above, we intend to make a full characterization of cellular organelles and pathways to dissect possible cellular defects, with a focus on the endo-lysosomal pathway, as well as the impact of unprocessed POS accumulation in CHM RPE cells. To develop this project, we proposed three main tasks the first is to characterize lysosomal function in the context of REP1 loss, the second is to dissect the endocytic pathway, and the final and third is to access POS phagocytosis and degradation in CHM cells.

To perform this work, we will employ human induced pluripotent stem cells (hiPSc-RPE) from healthy and CHM patient donors, which we will differentiate using a previously established protocol[110]. Additionally, we will also use an RPE immortalized cell line, ARPE-19, genetically engineered to have a null mutation in *CHM* gene.

In order to investigate lysosomal function in the context of REP1 we will focus on the quantification of lysosome numbers and size by fixed immunofluorescence, as well as live imaging techniques. Lysosomal activity will also be explored by focusing on cathepsin activity. Other components of the endo-lysosomal pathway, such as early endosomes and MVBs will also be analysed in terms of numbers and size. Finally, CHM RPE cells will be challenged with POS to access accumulation and interaction with components from the endo-lysosomal pathway, as represented in **Figure 13.**

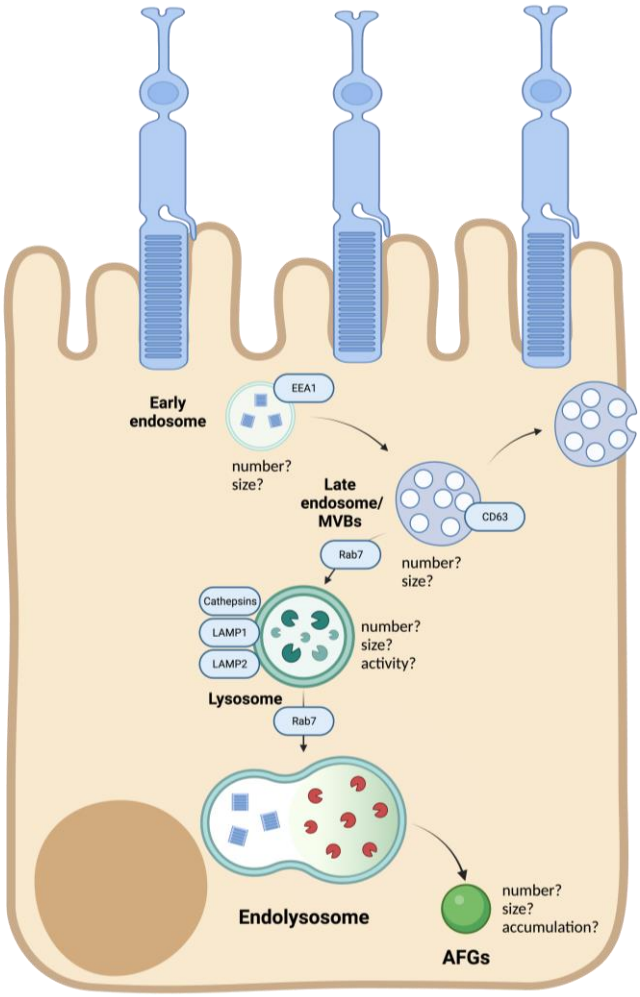

Figure 13. Graphical hypothesis - Characterization of the endo-lysosomal pathway. 1)Quantification of both number and size of early stages of the pathway by EEA1 staining, late stages of the pathway by CD63, LAMP1, LAMP2 and Cathepsin staining. 2) Quantification of AFGs accumulation in number and size.

Chapter 2 – Materials and Methods

2.1. *In vitro* models of RPE in the context of choroideremia

2.1.1. Immortalized cell model – ARPE-19

2.1.1.1. Thawing

ARPE-19 (ATCC) cells stored at either -80°C or -150°C were defrosted by submerging cryovial into pre-warmed 37°C water bath and rapidly plated into a 25cm^2 flask (t25) with Dulbecco's Modified Eagle Medium/Nutrient Mixture F-12 with GlutaMax (DMEM/F-12, GlutaMAX™, Cat #10565018, Gibco™) supplemented with fetal bovine serum (FBS, Cat #10500-064, Gibco™) and Penicillin-Streptomycin (PenStrep, Cat #15070063, Gibco™) to a final concentration of 10% and 1%, respectively. Cells were stored at 37°C and 5% CO_2 incubator. Media was changed the following day and cells are passed when confluency is reached.

2.1.1.2. Maintenance and Passage

When confluency is reached, ARPE-19 cells were passed by washing cells with a phosphate buffered saline (PBS, Cat #20012-068, Gibco™) and incubated with TrypLE™ Express Enzyme (TrypLE™, Cat #12604021, Gibco™) for 5 minutes at 37°C and 5% CO_2 incubator. Cells are then collected in a 15 mL of medium and centrifuged for 3 minutes at 1200 rpm. The supernatant is discarded, and the pellet resuspended in DMEM/F-12 media. Using a Neubauer counting chamber, cells were counted and plated according to the experimental use, Table 1. Cells were then incubated at 37°C and 5% CO_2 incubator.

Table 1. Cell density according to experimental need

Experiment	Plate type	Number of cells/well
Immunofluorescence	24-well	30x10^3
WB	6-well	250-350x10^3
Immunofluorescence POS	24-well	120x10^3
FACS POS	48-well	60x10^3
Live imaging	8-well microchamber	15x10^3
Live imaging POS	8-well microchamber	35x10^3
Maintenance	25 cm^2 flask (t25)	250x10^3

2.1.1.3. Cryopreservation

ARPE-19 cells are washed with PBS and incubated with TrypLE™ for 5 minutes at 3°C and 5% CO_2 incubator. DMEM/F-12 GlutaMAX™ is added to inactive TrypLE™ and cells are centrifuged for 3 min at 1200 rpm and counted using a Neubauer counting chamber. One million cells are resuspended in a solution containing 10% DMSO and 90% FBS and stored at -80°C or -150°C.

2.1.2. Pluripotent stem cell model – hiPSc-RPE

2.1.2.1. Cell lines information

To develop this project, we employed three different lines of human induced pluripotent stem cells (hiPSc). RBI001-A hiPSc line is commercially available and generated from fibroblasts of dermis of a Caucasian healthy man with age range of 45-49 years. A second line is from a CHM (Patient CHM$^{c.808C>T}$), obtained in collaboration with David Gamm Lab (Wisconsin University). Finally, a CRISPR/Cas9 generated isogenic mutant of RBi001-A, denominated RBi001-CHM$^{c.809insC}$ was used. Additionally, isogenic controls that were previously generated in the lab by Daniela Oliveira using CRISPR/Cas9 technology were sequenced and tested for the presence of REP1 (Clone 2_1_8; Clone 2_1_9; Clone 4_3).

2.1.2.2. Thawing and cryopreservation

Human induced pluripotent stem cells stored at either -150°C or -80°C were briefly thawed in a 37°C water bath, and the vial content added to 3 mL of StemFlex™ medium (Cat #A33493-01, Gibco™) and centrifuged for 5 min at 200xg. The supernatant was discarded, and pellet resuspended in 2 mL of StemFlex medium supplemented with 10 μM of ROCK Inhibitor (ROCKi, Cat #10-2301, Focus Biomolecules). The suspension was plated onto previously coated 6-well plate (Cat #734-1596, Corning®Costar®) with 0.2 mg/well of Corning® Matrigel Growth Factor Reduced Basement Membrane Matrix (Matrigel, Cat #354230, Corning®). hiPSc were grown in a 5% CO_2 ad 37°C incubator. Media was changed 24 hours later to remove cell debris and excess ROCKi.

To cryopreserve hiPSc, cells needed to reach an 80% confluency in a 6-well plate. Cells were washed with Dulbeccos's phosphate-buffered saline (DPBS, Cat #14190094, Gibco™) and lifted using 500 μL of a non-enzymatic cell dissociation reagent Versene (Cat #15040033, Gibco™) for 2 min. Cells were then resuspended in 1 mL of CryoStor® CS10 freeze media (Cat #07930, Stemcell Technologies), the vials were wrapped in paper to slowly freeze samples and vials stored at either -80°C and -150°C.

2.1.2.3. Maintenance and Passage

StemFlex media was changed every other day and cell morphology observed using a brightfield microscope. When confluency reached 80%, hiPSc were passed for either expansion, cryopreservation or for differentiation. To pass hiPSc, cells were washed with 1 mL of DPBS to remove cellular debris and incubated for 2 min at 37°C with 500 μL of Versene. The Versene was aspirated, and cells were resuspended in StemFlex medium with a split ratio of 1:4 to new pre-coated plates. Cells were maintained in a 5% CO_2 and 37°C incubator.

2.1.2.4. hiPSc 75-day differentiation protocol into RPE

The differentiation of hiPSc into RPE was performed accordingly to the Foltz & Clegg protocol[110]. When cells reach 80% confluency, 12-well plates (Cat #3512, Corning®Costar®) coated with Corning® Matrigel Non-Growth Factor Reduced Basement Membrane Matrix (NGFR-Matrigel, Cat #356237, Corning®) were prepared, and cells are washed with 1 mL of DPBS and lifted using 500 μL of Versene for 2 min at 37°C

and 5% CO_2 incubator. Retinal differentiation medium (RDM), which is composed of DMEM/F-12, GlutaMAX™, with 100x N2 (Cat #17502048, Gibco™), 50x B27 (Cat #17504044) and 100x non-essential amino acid (NEAA, Cat #11140050, Gibco™) was used throughout the 14 days of differentiation. Cells are then resuspended in previously prepared RDM with specific growth factors of day 0 according to the schedule in **Figure 14**. Cells were then plated onto 12-well plates in a 1:4 split ratio (one well of a 6-well plate plated onto four wells of a 12-well plate). During the 14-day differentiation, RDM is changed with the appropriate growth factors and inhibitors to obtain differentiated RPE culture, **Figure 14**. A checkpoint is performed on day 4, if cells do not show the expected confluency, differentiation is stopped.

When cells reach the end of the differentiation period, they are washed with DPBS and lifted with Versene for 2 min in the conditions previously mentioned. Versene is then removed and using a cell scarper, cells are lifted and resuspended in X-VIVO™-10 medium (TheraPEAK™ X-VIVO™-10 Serum-free Hematopoietic Cell Medium, Cat #BEBP04-743Q, Lonza) supplemented with 100x antibiotic-antimycotic (Cat #15240062, Gibco™). To remove cellular clamps formed during differentiation, cells were passed through a 40 μm pore strainer (Cat #431750, Corning®) and plated onto previously coated with Biolaminin 521 LN (hrLaminin 521, Cat #LN521-05, BioLamina) 6-well plates in a ratio of 1:4. The first 4-7 days, X-VIVO medium was supplemented with 10 μM of ROCKi. Medium was changed every 2-3 days and cells were allowed to growth for 30 days, achieving passage 0. Cells were then lifted and plated onto new plates according with experimental need and allowed to mature for 30 days achieving passage 1 and are considered ready to use. An additional passage can also be performed.

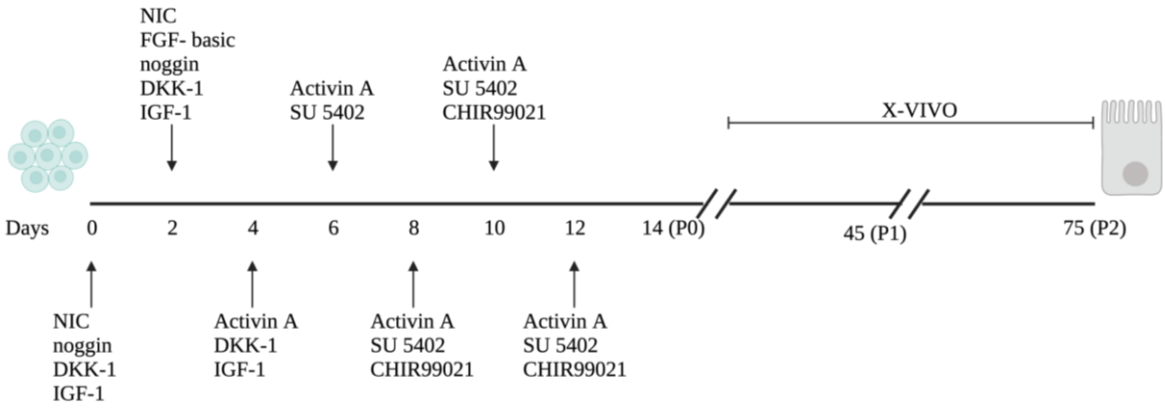

Figure 14. 75-day differentiation protocol timeline. Retinal differentiation medium (RDM) was added for 12 days with the respective growth factors and inhibitors. At day 14 and day 45 cells were passed to new plates and maintained in X-VIVO medium until day 75. Adapted from Filipa D, Oliveira C De. BSc in Biotechnology iPS Cell modelling of Choroideremia disease: Insights into trafficking pathways and necroptosis. 2021.

2.1.2.5. Transepithelial electrical resistance (TER)

hiPSc-RPE grown on Biolaminin 521 LN coated plates with transwells inserts (Cat #3470, Corning®Costar®) for or 30-days (P1) were used to measure the TER. TER was measured using a volt-ohmmeter following manufacturer's instructions (World Precision Instruments). TER was calculated by subtracting background TER of the laminin coated transwell, followed by recording both control and CHM

clones three times. The value obtained was then multiplied by 0.33 (area of transwell) and the final value represented by Ω cm^2.

2.1.2.6. Genomic DNA isolation

In order to confirm the correction of the genetic mutation in *CHM* gene in patient $CHM^{c.808C>T}$ cells and the isogenic control clones produced previously by Daniela Oliveira[111], hiPSc cells were thawed and plated onto 6-well plates and when they reached confluency, cells were washed with DPBS and the NZY Tissue gDNA Isolation kit (Cat #MB13502, NZYTech) according to the manufacturer's instructions. The genomic DNA was quantified using NanoDrop™ 2000 (ThermoFisher Scientific) spectrophotometer and either used for PCR or stored at -20°C.

2.1.2.7. Polymerase chain reaction, electrophoresis, and sequencing

The genomic DNA isolated from hiPSc was used for polymerase chain reaction (PCR) in order to amplify the exon 6 of CHM gene, the sequence targeted by the sgRNA used in genetic manipulation experiments. Amplification was achieved using 200 ng of genomic DNA with 25 μL of DreamTaq Green PCR Master Mix (2X) (Cat #K1081, ThermoFisher Scientific), 10 μM of forward (5' TCAGCTAATCAATTCTGAGCCTGT 3') and reverse (5' AAATCACCACGGAGGACTGG 3') primers, finalized with UltraPure™ DNase/RNase-Free Distilled Water (Cat #10977035, Invitrogen™) to achieve a final volume of 50 μL. The amplification was performed using T100™ Thermal Cycler (Cat #1861096, BioRad), with a reaction protocol of 30 cycles of 95°C for 30s, 60°C for 30s and 72°C for 1 min. The PCR product was then visualized in an agarose gel electrophoresis to confirm correct amplification of the target sequence. Agarose solution was prepared to achieve a final concentration of 1.5% w/v agarose (Cat #MB02703, NZYTech)/Tris-acetate-EDTA (TAE) buffer (Cat #161-0773, NZYTech). The mixture was heated until agarose was dissolved. A mixture was prepared and loaded onto the gel using 10 μL of PCR product and 1 μL of Xpert Green DNA Stain direct (Cat #GS02.0001, GRiSP) with one lane with 5 μL of O'GeneRuler 1kb DNA Ladder (Cat #SM1163, ThermoFisher Scientific) and 1 μL of Xpert Green DNA Stain. Electrophoresis was revealed under UV light using a ChemiDoc™ imaging system. PCR products were then purified using NZY Gelpure purification kit (Cat #MB01102, NZYTech) following manufactures indications and DNA quantified using NanoDrop™ 2000. After confirmation of the PCR product length and genomic DNA purification samples were sent for sequencing by StabVida™.

2.2. Immunofluorescence

2.2.1. Fixed cell imaging – ARPE-19

After 5 days post-passage, cells coated on glass coverslips were fixed with either 4% paraformaldehyde (PFA, Cat #43368, Alpha Aesar) or ice-cold methanol for 15 minutes at room temperature or -20°C, respectively. After fixation, cells were washed 3 times with PBS 1x and incubated with 50 μL of permeabilization/blocking solution containing 1% BSA (Cat #MB04603, NZYTech) and 0.05% saponin (Cat #47036-50G-F) in PBS solution for 30 minutes at room temperature. Cells were then incubated with 50 uL of primary antibody prepared in permeabilization/blocking solution in a 1:100 dilution for 1 hour at room

temperature. Afterwards, cells were washed in a PBS solution for about 15-20 seconds and incubated with 50 uL of secondary antibody previously prepared in a PBS solution in a 1:500 ratio with limited light exposure for 30 min at RT. Lastly, coverslips were incubated with a DAPI (Cat #D9542-5MG, Sigma-Aldrich) solution (1:10 000) for 1 minute at room temperature. Coverslips were generously washed for 15-20 seconds and mounted onto a glass slide with MOIWOL mounting media. Glass slides were left to dry into a flat surface with limited light exposure overnight at room temperature. The primary and secondary antibodies used are listed in **Table 2.**

2.2.2. Live cell imaging – ARPE-19

ARPE-19 cells were plated into 8-well Lab-Tek chambered coverglass (Cat #155411, ThermoFisher Scientific) and after 5-days cells were ready to be imaged. The dyes and respective dilutions are shown in **Table 2**. Images and videos were acquired using LSM980 (Zeiss) confocal microscope previously warmed to 37°C. Images were taken as Z stacks and videos using time series taken every 2 seconds for 1 or 2 minutes**.**

2.2.3. Antibodies and dyes – ARPE-19

Table 2. Primary and secondary antibodies used for fixed, and dyes used for live cell imaging in ARPE-19 cells. Respective host species, catalog number, brand, fixation method and dilutions.

Primary Antibody Live dyes	Host species	Catalog number	Brand	Fixation Method	Dilution
Anti- Cathepsin B	Goat	AF953	R&D	Methanol	1:100
Anti- Cathepsin D	Goat	AF1014	R&D	PFA	1:100
Anti- Cathepsin D	Goat	AB0043-200	SicGen	Methanol	1:100
Anti- CD63	Mouse	sc-5275	Santa Cruz	PFA	1:100
Anti- EEA1	Mouse	#610456	BDT	PFA	1:100
Anti- LAMP1 488 (H4A3)	Mouse	328610	Biolegend	PFA	1:100
Anti- LAMP1 647 (H4A3)	Mouse	328612	Biolegend	PFA	1:100
Anti- LAMP2 (H4B4)	Mouse	sc-18822	Santa Cruz	PFA	1:100
Anti- Rab7	Goat	AB0033-200	SicGen	PFA	1:100
Anti- TOM20	Rabbit	Ab186734	Abcam	PFA	1:100
Anti- Zonula Occludin-1	Rabbit	40-2300	Invitrogen (Zymed)	Methanol	1:100
Lysotracker red DND-99	-	L7528	ThermoFisher Scientific	-	1:10 000
Magic Red Cathepsin B	-	6134	ImmunoChemistry Technologies	-	1:250
Magic Red Cathepsin L	-	6138	ImmunoChemistry Technologies	-	1:250
Phalloidin Alexa Fluor™ 568	-	A12380	Invitrogen	PFA	1:100
pHrodo red Dextran	-	P10361	Invitrogen	-	1:25
SiR-lysosome	-		Spyrochrome	PFA	1 μM
Secondary Antibody	**Host species**	**Catalog Number**	**Brand**		**Dilution**
Anti- goat 488	Chicken	A21467	Invitrogen	-	1:500
Anti- mouse 488	Donkey	A21202	Invitrogen	-	1:500
Anti- mouse 488	Goat	A11029	Invitrogen	-	1:500
Anti- mouse 647	Goat	A21235	Invitrogen	-	1:500
Anti- rabbit 488	Goat	A11034	Invitrogen	-	1:500
Anti- rabbit 488	Donkey	A21206	Invitrogen	-	1:500

2.2.4. Microscope acquisition

Immunofluorescence images were acquired in LSM980 (Zeiss) confocal microscope. Images were obtained using 63x objective with immersive Oil. Images of the endo-lysosomal pathway markers (EEA1, CD63, LAMP1, LAMP2, Rab7, CTSD, CTSB) were obtained with 3.0x zoom, while POS feeding experiments were visualized using 1.0x zoom. ZO-1 was visualized with 1.0x zoom. All images were acquired as Z stacks

and analysed using Fiji. Quantifications were carried out using macros and automated segmentation in Fiji software.

2.2.5. Fixed cell imaging – hiPSc-RPE

Cells plated on laminin coated coverslips in 24-well plates for 30 days were washed twice with PBS and fixed with 500 μL of ice cooled methanol or 4% paraformaldehyde for 15 min on ice or room temperature, respectively. After fixation, cells were washed three times with PBS and permeabilized and blocked with 500 μL with a PBS solution with 0.05% v/v Triton-X100 (Cat #85111, ThermoFisher Scientific) and 10% v/v Donkey serum (Cat #S30-100ML, Sigma-Aldrich) for 1h at room temperature. After permeabilization and blocking, cells were incubated with primary antibody, prepared in the previous solution for 2h at room temperature. Cells were then washed with PBS four times for 10 minutes with gentle shaking and then incubated with the appropriate secondary antibody also prepared in the PBS solution mentioned above for 1h at room temperature. Cells were once again washed four times for 10 min with gentle rocking and incubated with DAPI for 2 min at room temperature. Coverslips were mounted using VECTASHIELD® Antifade Mounting medium (Cat #H-1000-10, Vector laboratories) and stored at 4°C with limited light exposure until analysis. The primary and secondary antibodies used are listed in **Table 3.**

2.2.6. Antibodies – hiPSc-RPE

Table 3. Primary and secondary antibodies used for fixed cell imaging in hiPSc-RPE cells. Respective host species, catalog number, brand, fixation method and dilutions.

Primary Antibody	**Host species**	**Catalog number**	**Brand**	**Fixation Method**	**Dilution**
Anti- Cathepsin D	Mouse	#6100801	BDT	Methanol	1:100
Anti- Claudin-19	Mouse	365967	Santa Cruz	Methanol	1:100
Anti- CD63	Mouse	sc-5275	Santa Cruz	PFA	1:100
Anti- EEA1	Rabbit	2411S	Cell Signalling	PFA	1:100
Anti- LAMP1	Rabbit	3243S	Cell Signalling	PFA	1:100
Anti- LAMP2 (H4B4)	Mouse	sc-18822	Santa Cruz	PFA	1:100
Anti- PMEL	Mouse	M0634	Dako	PFA	1:100
Anti- Zonula Occludin-1	Rabbit	40-2300	Invitrogen (Zymed)	Methanol	1:100
Secondary Antibody	Host species	Catalog Number	Brand		Dilution
Anti- mouse 488	Donkey	#A21447	Invitrogen	-	1:500
Anti- mouse 488	Goat			-	1:500
Anti- rabbit 488	Goat			-	1:500
Anti- rabbit 488	Donkey	#A21206	Invitrogen	-	1:500

2.2.7. Microscope acquisition

Immunofluorescence images were acquired in LSM980 (Zeiss) confocal microscope. Images were obtained using 63x objective with immersive Oil. Images of the endo-lysosomal pathway markers (EEA1, CD63, LAMP1, LAMP2, Rab7, CTSD, CTSB) were obtained with 4.0x zoom. ZO-1, Claudin-19 and Premelanosomal protein (PMEL) were visualized with 1.0x zoom. All images were acquired as Z stacks and analysed using Fiji. Quantifications were carried out using macros and automated segmentation in Fiji software.

2.3. Immunoblotting experiments

2.3.1. Protein extraction and quantification

Cells grown on 6-well plates with a density of $250x10^3$-$350x10^3$ cells/well were grown until confluency was reached. Cells were washed two times with PBS and 110 uL of lysis buffer with 100x Protease and Phosphatase Inhibitor Cocktail (Cat #78444, ThermoFisher Scientific) was added to each well and plates were placed at -80°C for at least 20 minutes. Cells were then scraped off the plate using a bend tip, collected into a 1.5 mL eppendorf, and centrifuged for 10 minutes, at 13.000 rpm at 4°C in a previously cooled centrifuge. Supernatant were collected into a clean 1.5 mL eppendorf. Protein was quantified using Pierce™ BCA Protein Assay Kit (Cat #23227, ThermoFisher Scientific), following manufacturer's instructions. Samples were then prepared using 1:4 ratio of protein sample buffer (PBS, Tris-HCL 250 mM pH=6.8, SDS 8%, Glycerol 40%, β-mercaptoetanol 20%, Bromophenol blue 0.08%) and, denatured at 95°C for 5 minutes and stored at -20°C until use.

2.3.2. SDS-PAGE gel electrophoresis and Western blot

SDS-PAGE gels were prepared with either 8%, 10%, 12% or 15% of acrylamide in a Tris-HCl buffer for the resolving component, with a 4% of acrylamide for the stacking portion in a Tris-HCl buffer. The same amount of protein was loaded in the gel, ranging from 15-30 ug. The gel was run at 90 V until the samples reached the resolving gel and then, the voltage was increased to 120 V until the running front reached the bottom of the gel. Afterwards, gels were transferred to a 0.2 um nitrocellulose membrane (Cat #1704159, BioRad) using the Trans-Blot Turbo™ Transfer System (Cat #1704150, BioRad). Membranes were then incubated with 5% dried milk in Tris buffered saline (TBS, 20 mM Tris, 140 mM NaCl, pH=7.6) solution with 0.1% of Tween-20 (TBS-T) for 1h at RT. The primary antibody, previously prepared in 5% BSA with the desired dilution (Table 4), was added to the membranes and incubated ON at 4°C. Afterwards, membranes were washed 3 times for 10 min with TBS-T. Secondary antibodies conjugated to HRP were prepared in freshly made 5% dried milk in TBS-T and incubated for 1h at RT. Nitrocellulose membranes were washed for at least 45 min, with TBS-T changes every 5-10 min. Proteins were detected using the ChemiDoc™ Imaging System, making use of the ECL Prime Western Blotting Detection Reagent (Cat #RPN2232, GE Healthcare). The primary and secondary antibodies used are listed in Table 4.

2.3.3. Antibodies

Table 4. Primary and secondary antibodies used for Western Blot analysis. Respective host species, catalog number, brand, and dilutions.

Primary Antibody	Host species	Catalog number	Brand	Dilution
Anti- β-actin HRP-conjugated	Mouse	#A3854	Sigma Aldrich	1:25 000
Anti- Calnexin	Goat	AB0041-20	SicGen	1:2000
Anti- Cathepsin D	Goat	AB0043-200	SicGen	1:1000
Anti- Cathepsin D	Rabbit	Ab75852	Abcam	1:1000
Anti- Cathepsin L	Goat	AF952	R&D	1:1000
Anti- Claudin-19	Mouse	365967	Santa Cruz	1:100
Anti- CD63	Goat	AB0047	SicGen	1:1000
Anti- EEA1	Rabbit	2411S	Cell Signalling	1:1000
Anti- LAMP1	Rabbit	3243S	Cell Signalling	1:1500
Anti- LAMP2 (H4B4)	Mouse	sc-18822	Santa Cruz	1:1500
Anti- Nanog	Goat	#134218	R&D	1:1000
Anti- OCT 3/4	Mouse	#5279	Santa Cruz	1:500
Anti- REP1	Goat	AB0123	SicGen	1:500
Anti- TOM20	Rabbit	Ab186734	Abcam	1:1000
Secondary Antibody	**Host species**	**Catalog Number**	**Brand**	**Dilution**
Anti- Goat IgG	Donkey	#A16005	ThermoFisher Scientific	1:5000
Anti- Mouse IgG	Sheep	#554002	BD Pharmingen	1:5000
Anti- Rabbit igG	Donkey	#NA934	GE Healthcare	1:5000

2.4. Photoreceptor outer segments (POS) experiments

2.4.1. POS isolation and extraction

POS were isolated from porcine eyes following Parinot et al[112] with some modifications. Porcine eyes are obtained from a slaughterhouse and kept on ice. Eyeballs are cleaned of remaining tissue and washed in a 1% Pen/Strep in PBS solution for 5 minutes. Afterwards, eyes were opened using a scalpel and placed in 12-well plate facing up. The inside of the eye was washed with PBS and the neural retinal carefully removed and collected into a conical tube that contains a homogenization solution (20% sucrose, 20 mM tris acetate pH 7.2, 2 mM $MgCl_2$, 10 mM glucose, 5 mM taurine). The mixture was filtered through a gauze and added to a sucrose continuous gradient (25%-60% sucrose, 20 mM tris acetate pH 7.2, 10 mM glucose, 5 mM taurine). Next, a centrifugation at 25 000 rpm for 120 minutes in a swing rotor was carried out. Afterwards, a single orange band should be seen in the upper section of the gradient, which corresponds to the POS. This band was aspirated and washed three times by sequential centrifugations (5000 rpm for 10 minutes at 4°C) with

different solutions (wash 1: 20 mM tris acetate pH 7.2, 5 mM taurine; wash 2: 10% sucrose, 20 mM tris acetate pH 7.2, 5 mM taurine; wash 3: 10% sucrose, 20 mM sodium phosphate pH 7.2, 5 mM taurine). After each centrifugation the pellet was resuspended. POS were then washed in PBS and protein content measured using BCA Protein Assay Kit. POS was also counted in a cell counting chamber, aliquoted and stored (concentration: 2000 μg/mL) at -80°C in a solution containing 10%FBS, 2.5% sucrose, 0.04% sodium azide, and 1%Pen/Strep[46].

2.4.2. POS preparation and feeding

Aliquots of previously extracted and isolated POS stored at -80°C were thawed and centrifuged for 10 min, 5000 rpm at 4°C in a previously cooled centrifuge. In a cell culture hood, supernatant is discarded, and the pellet resuspended in 1 ml of sterile PBS 1x. The sample is once again centrifuged for 10 min 5000 rpm at 4°C, and the pellet resuspended in PBS 1x and stored at 4°C with limited light exposure. To feed cells with POS, media is removed from each well and diluted POS are added in the following ratio: 30 uL + 220 uL media in 48-well plate and 60 uL + 440 uL media in 24-well plate for 4h, so that the final concentration is always $5x10^5$ POS per cm^2. After the 4h pulse, each well is vigorously washed with media to remove membrane attached POS that were not incorporated by the cells. After washing, the chase time starts counting from 0h forward and cells are collected and used for experiments in the time points indicated.

2.5. FACS experiments

2.5.1. Sample preparation and acquisition

ARPE-19 cells plated onto 48-well plates and fed with POS for 4 hours and chased during 72h were harvested and washed with PBS. Cells were then incubated with 50 μL of Tryple solution for 10-15 min at 37°C, afterwards 300 μL of FACS buffer (PBS, 1% FBS and 2 mM EDTA) was used to resuspend cells which were then centrifuged for 5 min at 1200 rpm and 4°C. The supernatant was discarded, and the pellet resuspended in 300 μL of FACS buffer. Of note, FACS buffer was only used when cold. Data acquisition was obtained using FACS Canto II (BD Biosciences). Following sample preparation, gates were created to detect only 488 positive cells. We aimed to acquire 1×10^4 events per condition and had triplicate or quadruplicate samples per conditions in each experiment.

2.6. Statistical Analysis

Results are presented as Mean ± Standard Error of the Mean (SEM) for independent experiments and Mean ± Standard deviation (SD) for technical replicates within independent experiments. Statistical analyses were performed using the GraphPad Prism 9.0.1. software. Normal distribution was assess using the Shapiro-Wilk test and, if results were verified to have a normal distribution, statistical comparisons were analysed for their homoscedasticity using the Bartlett test. If homoscedasticity an unpaired Student's t test was applied and if not an unpaired t test with Welch's correction was chosen. If normal distribution is not verified, a Mann-Whitney test was applied. Differences were considered significant as: *$p<0.05$, *$p<0.01$, ***$p<0.005$ and ****$p<0.001$.

Chapter 3 – Results

3.1. ARPE-19 as a model for choroideremia

3.1.1. Characterization of ARPE-19 as a cell model of choroideremia

In order to characterize the endo-lysosomal pathway in the context of a CHM RPE cell model, we decided to use a commonly used RPE immortalized cell line, ARPE-19, due to its rapid replication rates and high yield, as well as the ability to analyse phagocytic events in cellular context. To reproduce the CHM cellular environment, we used a CRISPR-Cas9 genetically modified cell line where a mutation in the REP1 gene was introduced, a cell line previously produced and established in our lab[111] (more information in **Supplementary Figure 1**), hereafter termed $CHM^{-/-}$.

Western blot analysis of both WT and $CHM^{-/-}$ ARPE-19 cells revealed the complete knockout of REP1, **Figure 15 C**. Both RPE cell lines were seen to form a tight monolayer, with defined borders between adjacent cells, as observed in the immunofluorescence images of the cytoskeleton marker, phalloidin, which stains filamentous actin, and zonula occludins-1 staining, ZO-1, which marks tight junctions between cells, **Figure 15 A and 15 B**.

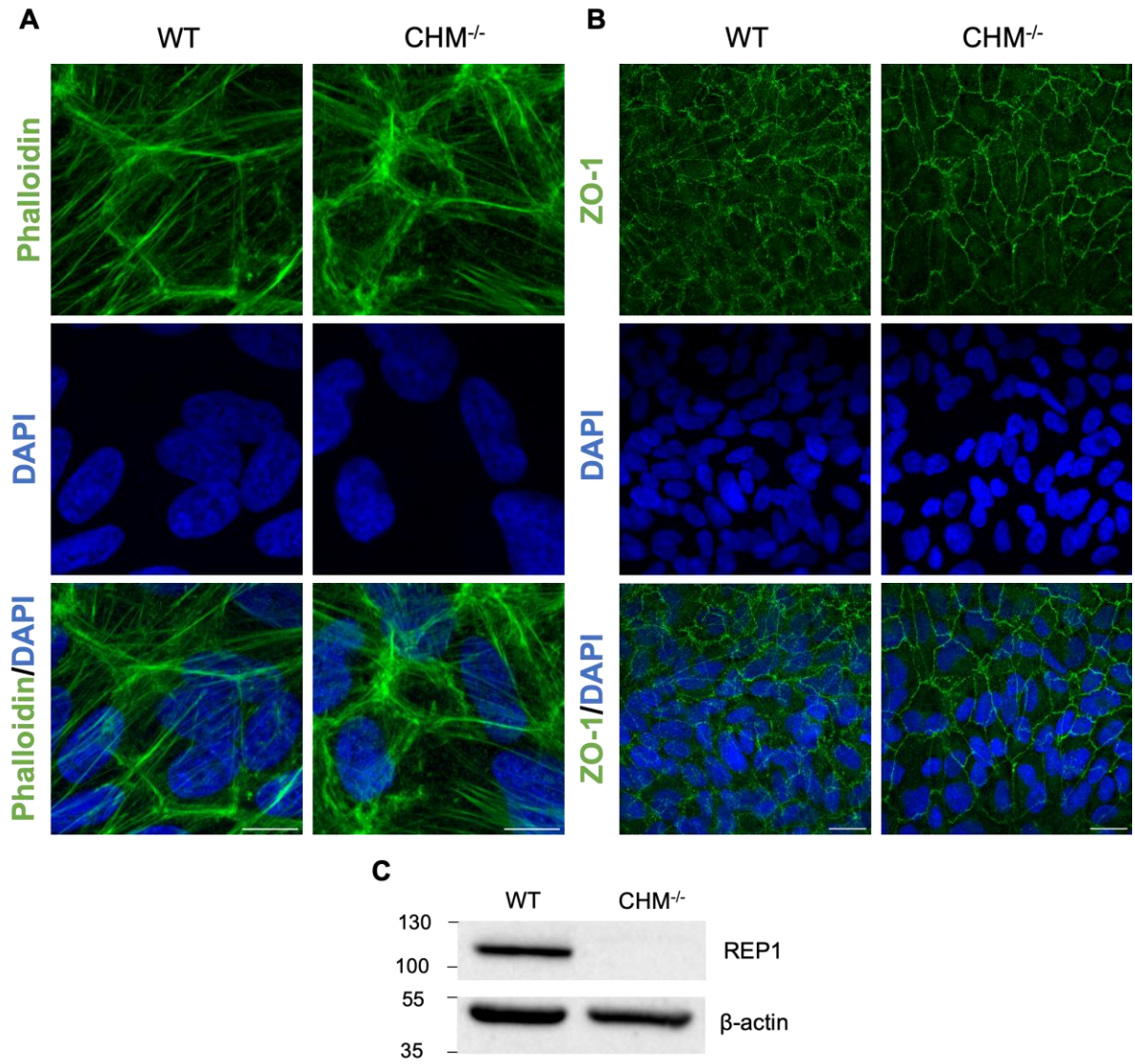

Figure 15. ARPE-19, immortalized cell model of CHM$^{-/-}$. A) Immunofluorescence staining of phalloidin, marker of F-actin (green). Scale bar 10 μm. **B)** Immunofluorescence staining of zonula occludins-1, ZO-1 (green). Scale bar 20 μm. **C)** Western blot analysis of REP1 expression in ARPE-19 cells. Data representative of n=3. Loading control: β-actin.

3.1.2. Characterizing the early endo-lysosomal pathway in ARPE-19

As a mean to uncover the effects of REP1 absence in the endocytic pathway, we decided to begin by focusing on its early stages, therefore we used an early endosome marker, EEA1. Immunofluorescent analysis of WT and CHM $^{-/-}$ cells using automatic image analysis and structure quantification revealed no difference in the numbers of EEA1+ vesicles per nuclei (p-value: 0.7038), with no difference in the average size (μm^2) of these vesicles (p-value:0.2236), **Figure 16 A, 16 B and 16 C**. The protein expression levels of EEA1, analysed by WB, showed no changes between WT and CHM $^{-/-}$ cells, **Figure 16 D and 16 E**.

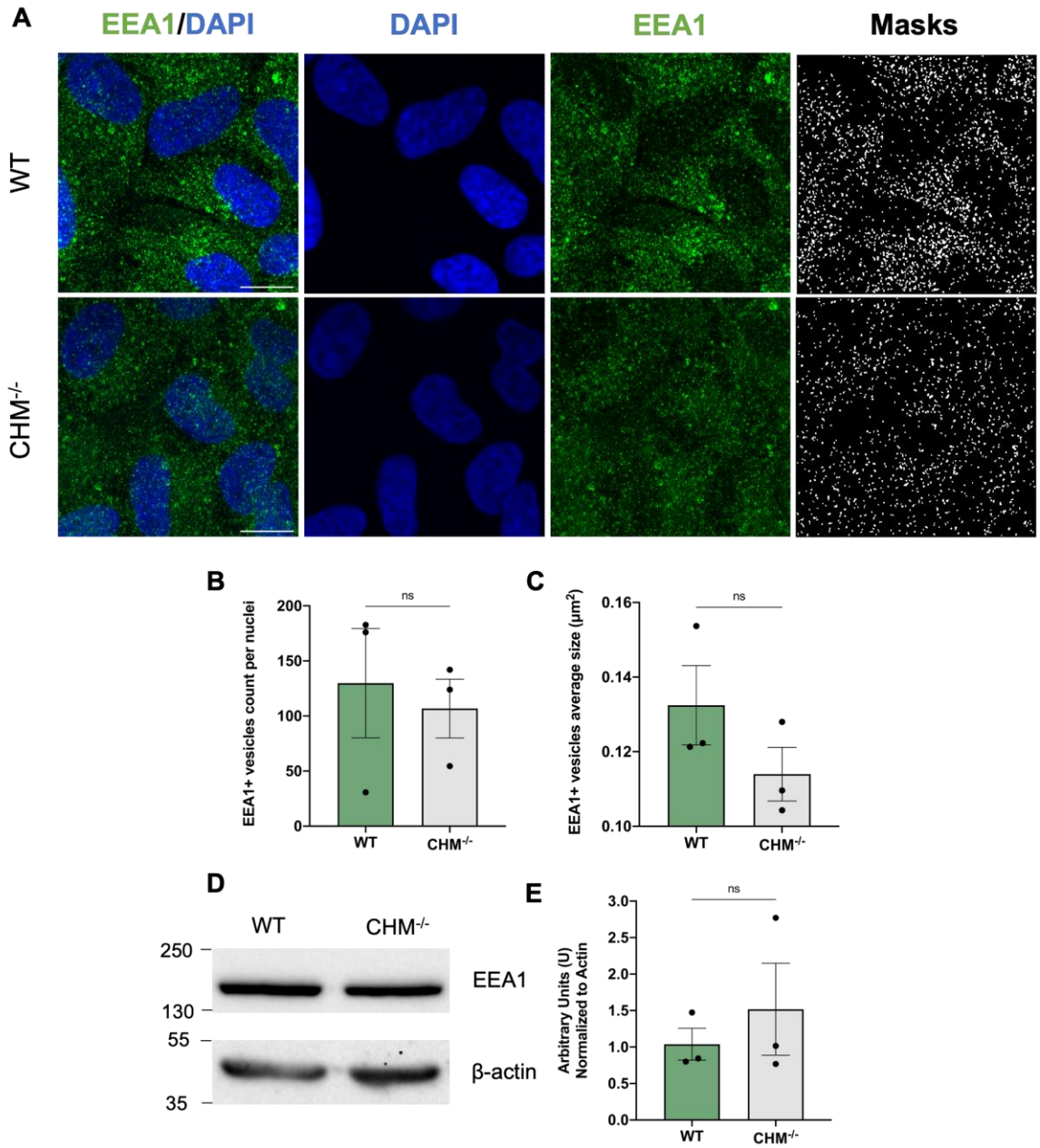

Figure 16. Early stages of the endo-lysosomal pathway in ARPE-19 cell model. **A)** Immunofluorescence images of early endosome marker, EEA1 (green) and nuclei stained with DAPI (blue). Scale bar 10 µm. **B)** Quantification of the number of EEA1+ vesicles per nuclei. Data is presented as Mean ± SEM, representative of n=3 independent experiments. Statistical comparisons were performed using unpaired t-test (ns, not significant). **C)** Average size of EEA1+ vesicles (µm^2). Data is presented as Mean ± SEM, representative of n=3 independent experiments. Statistical comparisons were performed using unpaired t-test (ns, not significant). **D)** Western blot analysis of EEA1 expression in whole cell lysates between WT and CHM$^{-/-}$ cells, representative of n=3 independent experiments. Loading control: β-actin. **E)** Graphical representation of WB quantification. Normalized to β-actin. Data is presented as Mean ± SEM, representative of n=3 independent experiments. Statistical comparisons were performed using unpaired t-test (ns, not significant).

3.1.3. Characterizing late endo-lysosomal pathway in ARPE-19

As early endosomal structures mature along the endo-lysosome pathway, they can diverge into two different faits; they can be recycled back and fuse with the plasma membrane, releasing ILVs in the form of extracellular vesicles (EVs), or fuse and mature into lysosomes. The fusion with already formed lysosomes is

regulated by multiple proteins, some of them being the Rab GTPases, thus the characterization of lysosomes in the absence of REP1 is of extreme importance to uncover the molecular consequences of dysfunctional Rab regulation.

To study lysosomes, we decided to assess the number of vesicles formed using common lysosomal marker, such as Lysosomal-associated membrane protein 1 (LAMP1). A significant increase (p-value: 0.0324) in the number of LAMP1+ vesicles was observed in cells absent for REP1 compared to healthy cells, **Figure 17 A and 17 B**. LAMP1+ vesicle average size showed no difference in CHM$^{-/-}$ cells when compared to WT, with average sizes of 0.2624 μm^2 and 0.2581 μm^2, respectively, **Figure 17 A and 17 C.**

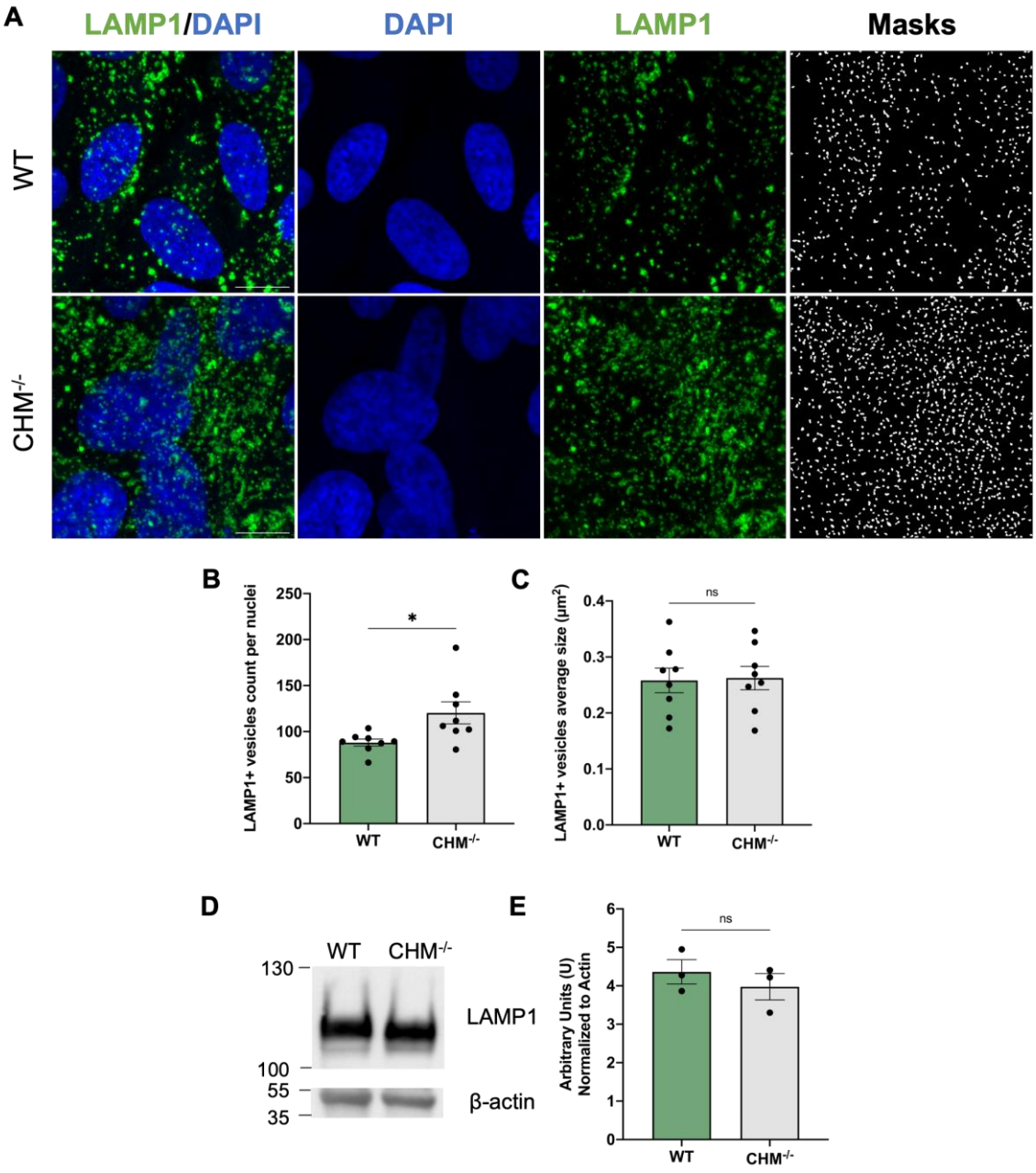

Figure 17. LAMP1+ vesicles are significantly increased in CHM$^{-/-}$ ARPE-19 cell model. **A)** Immunofluorescence images of lysosomal marker, LAMP1 (green) with nuclei stained with DAPI (blue). Scale bar 10 μm. **B)** Quantification of the number of LAMP1+ vesicles per nuclei. Data is presented as Mean ± SEM, representative of n=8 independent experiments. Statistical comparisons were performed using unpaired t-test with Welch's correction (* P<0.05). **C)** Average size of LAMP1+ vesicles (μm^2). Data is presented as Mean

± SEM, representative of n=8 independent experiments. Statistical comparisons were performed using unpaired t-test (ns, not significant). **D)** Western blot analysis of LAMP1 expression in whole cell lysates between WT and CHM$^{-/-}$ cells, representative of n=3 independent experiments. Loading control: β-actin. **E)** Graphical representation of WB quantification. Normalized to β-actin. Data is presented as Mean ± SEM, representative of n=3 independent experiments. Statistical comparisons were performed using unpaired t-test (ns, not significant).

The expression of LAMP1 protein did not show significant differences and seems to not be affected by the absence of REP1 in CHM$^{-/-}$ cells, as observed in **Figure 17 D and 17 E**, suggesting that the increased number of LAMP1+ vesicles is not due to an increase in the LAMP1 protein expression but more likely due to a change in the distribution of the protein and consequently its distribution of lysosomes throughout CHM$^{-/-}$ cells.

To further analyse the effects of REP1 absence in the lysosomal populations, we decided to evaluate two other markers, LAMP2 and Rab7, **Figure 18 and 19**. Immunofluorescent staining of LAMP2 shows a slight tendency for increased numbers of LAMP2+ vesicles in CHM$^{-/-}$ cells, however such difference is not significant (p-value: 0.5933), **Figure 18 A and 18 B**. The average size of LAMP2+ vesicles show no difference between WT and CHM$^{-/-}$ cells, with values of 0.2579 μm^2 and 0.2525 μm^2 respectively, **Figure 18 A and 18 C**.

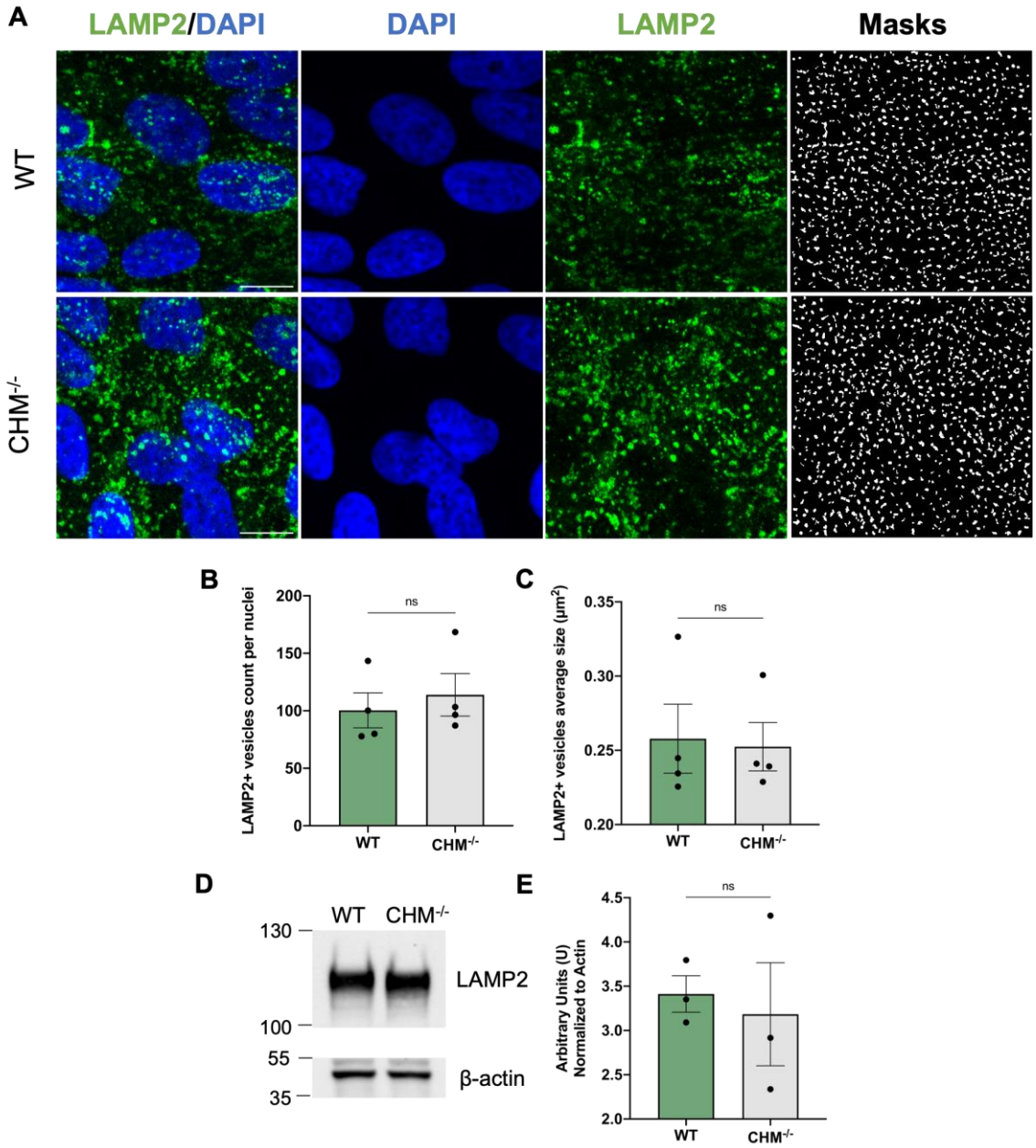

Figure 18. Characterization of LAMP2+ vesicles in CHM$^{-/-}$ ARPE-19 cell model. **A)** Immunofluorescence images of lysosomal marker, LAMP2 (green) with nuclei stained with DAPI (blue). Scale bar 10 µm. **B)** Quantification of the number of LAMP2+ vesicles per nuclei. Data is presented as Mean ± SEM, representative of n=4 independent experiments. Statistical comparisons were performed using unpaired t-test (ns, not significant). **C)** Average size of LAMP2+ vesicles (µm^2). Data is presented as Mean ± SEM, representative of n=4 independent experiments. Statistical comparisons were performed using unpaired t-test (ns, not significant). **D)** Western blot analysis of LAMP2 expression in whole cell lysates between WT and CHM$^{-/-}$ cells, representative of n=3 independent experiments. Loading control: β-actin. **E)** Graphical representation of WB quantification. Normalized to β-actin. Data is presented as Mean ± SEM, representative of n=3. Statistical comparisons were performed using unpaired t-test (ns, not significant).

The expression levels of LAMP2, just as LAMP1, did not show significant differences between WT and CHM$^{-/-}$ cells, **Figure 18 D and 18 E.**

Additionally, since REP1 influences the proper geranylgeranylation of Rab GTPases, we wanted to explore the localization of Rab7, a late endosome/lysosome marker. Immunofluorescence images of ARPE-19 reveal a significant increase (p-value: 0.0307) in the number of Rab7+ vesicles in CHM$^{-/-}$ cells, **Figure 19 A**

and 19 B. Regarding vesicle size, just as for LAMP1 and LAMP2, Rab7+ positive vesicles also show no difference in their average size when REP1 is absent, with sizes of 0.2533 μm^2 for WT cells and 0.2303 μm^2 for CHM$^{-/-}$ cells, **Figure 19 A and 19 C.** However, further experiments are needed to validate the observations.

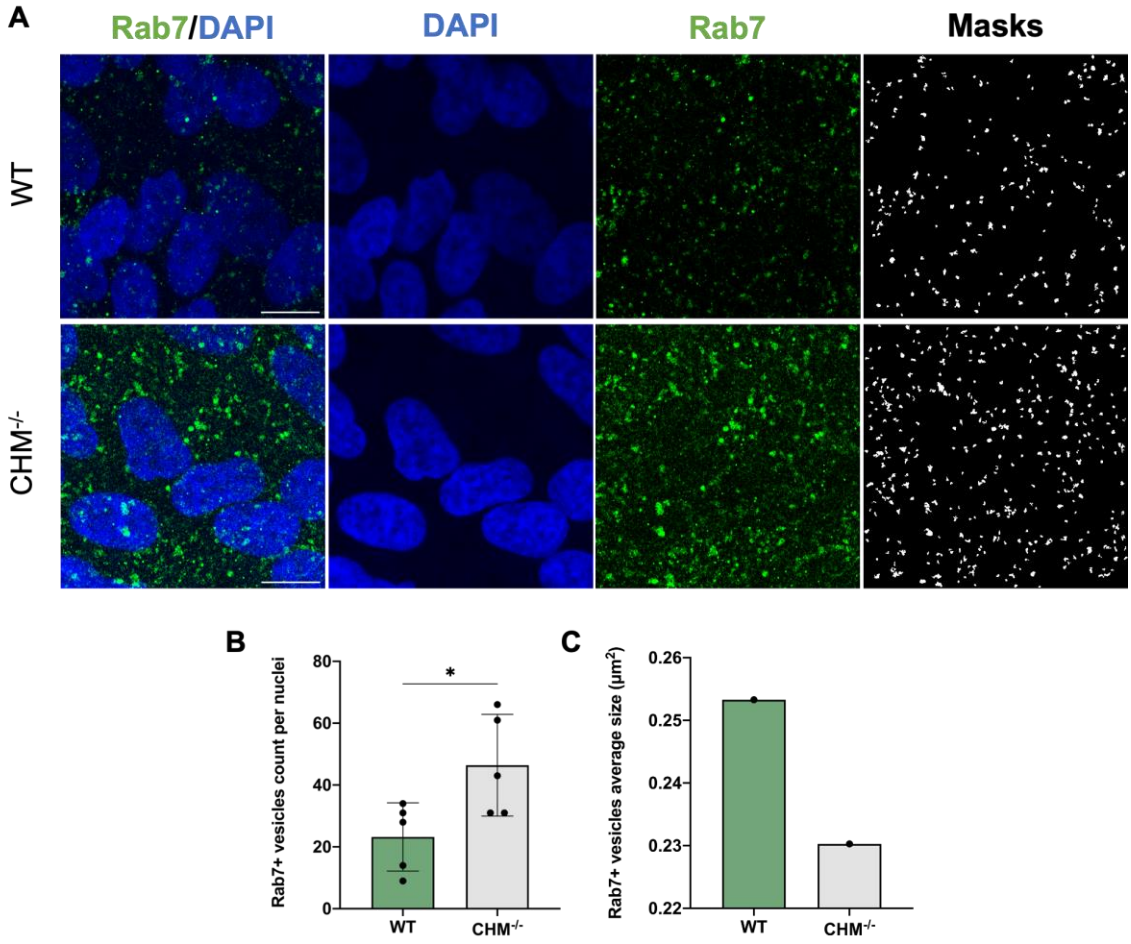

Figure 19. Characterization of late-stage regulatory Rab GTPase in CHM$^{-/-}$ ARPE-19 cell model. **A)** Immunofluorescence images of late-stage marker, Rab7 (green) with nuclei stained with DAPI (blue). Scale bar 10 μm. **B)** Quantification of the number of Rab7+ vesicles per nuclei. Data is presented as Mean ± SD, representative of n=1 independent experiment. Statistical comparisons were performed on technical replicates using unpaired t-test (* P<0.05). **C)** Average size of Rab7+ vesicles (μm^2). The mean vesicle size is presented, representative of n=1 independent experiment.

When early endosomes continuously mature, identified by the loss/addition of different protein markers, they form structures denominated by late endosomes. To analyse late endosomes in ARPE-19 we decided to use the CD63 marker, which is known to localize to MVBs, as well as the ILVs inside[113,114]. The quantification of CD63+ vesicles per nuclei, revealed a significant increase (p-value: 0.0132) in their number in CHM$^{-/-}$ mutants compared to WT, as presented in **Figure 20 A and 20 B.** Regarding vesicle size, CD63+ vesicles showed no difference between CHM$^{-/-}$ and WT cells, with mean size of 0.1979 μm^2 in CHM$^{-/-}$ and 0.1796 μm^2 in WT, **Figure 20 A and 20 C**.

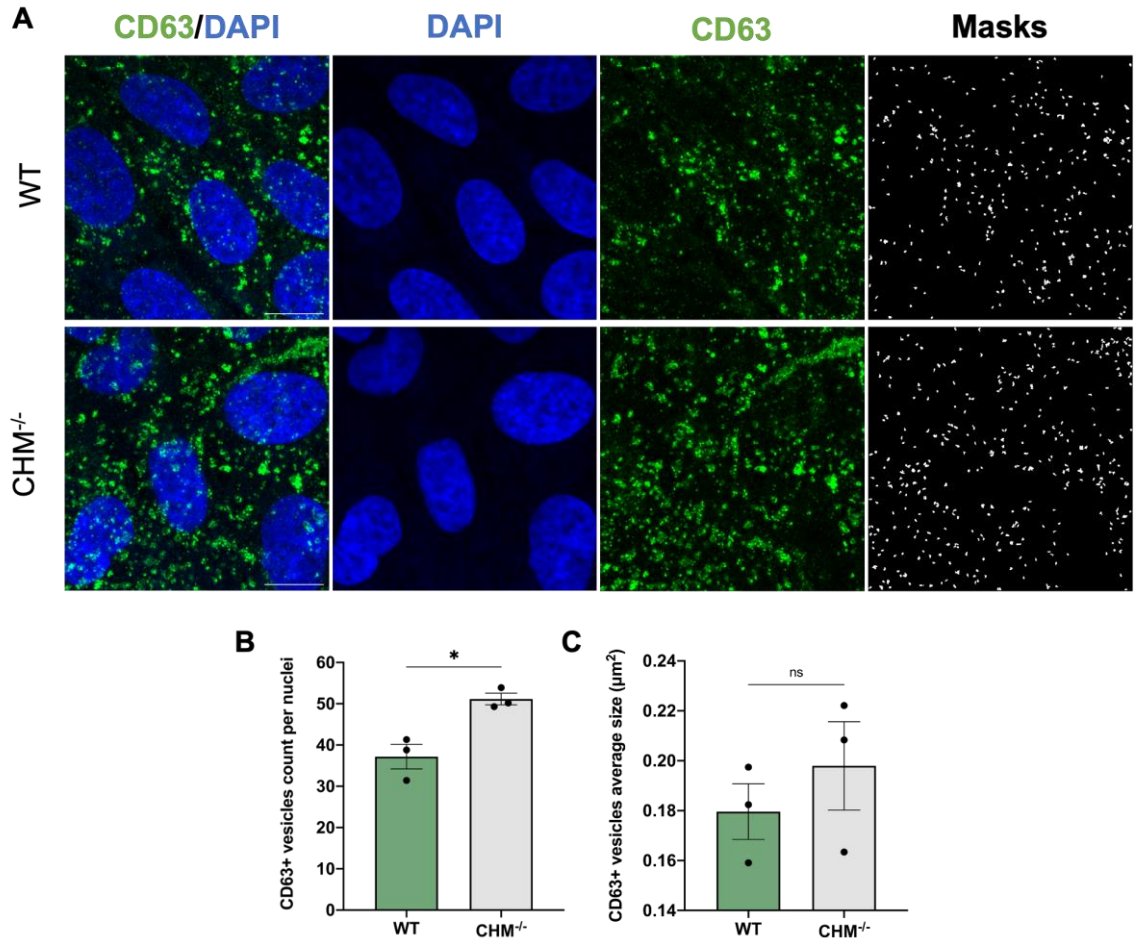

Figure 20. Characterization of late endosomes/MVBs in CHM$^{-/-}$ ARPE-19 cell model. **A)** Immunofluorescence images of multivesicular bodies (MVBs), CD63 (green) with nuclei stained with DAPI (blue). Scale bar 10 µm. **B)** Quantification of the number of CD63+ vesicles per nuclei. Data is presented as Mean ± SEM, representative of n=3 independent experiments. Statistical comparisons were performed using unpaired t-test (* P<0.05). **C)** Average size of CD63+ vesicles (µm^2). Data is presented as Mean ± SEM, representative of n=3 independent experiments. Statistical comparisons were performed using unpaired t-test (ns, not significant).

3.1.4. A deep dive into lysosomes: activity and function

Lysosomes are known as specialized degradation hubs for both extracellular and intracellular components, and to achieve this, they are equipped with multiple enzymes specialized in degrading different subsets of cellular waste, such as proteins and lipids. Some of the most common enzymes found in lysosomes are cathepsins, proteases found in highly acidic compartments within cells[115]. With our objective in mind, we decided to investigate the expression levels as well as numbers and sizes of the vesicles where these enzymes are found in both WT and CHM$^{-/-}$ cells.

Cells stained with an anti-cathepsin D antibody (from R&D) showed a tendency for an increase in the number of cathepsin D+ vesicles in CHM$^{-/-}$ cells, however more statistical power is needed to make further conclusions, **Figure 21 A and 21 B.** In terms of size, the tendency follows the one found for LAMP1, LAMP2 and Rab7, with no difference measured in CHM$^{-/-}$ cells when compared to controls (mean size of 0.3617 µm^2 and 0.4334 µm^2, respectively, **Figure 21 A and 21 C**. A different antibody for cathepsin D (from SicGen), was also tested, where the number of Cathepsin D+ vesicles also show a slight tendency towards higher numbers

in CHM$^{-/-}$ cells, but just like the previous results more independent experiments are needed to make further conclusions, **Figure 21 D and 21 E.** The average vesicles size shows no difference in CHM$^{-/-}$ cells when compared to WT (mean size of 0.2965 μm^2 and 0.3387 μm^2, respectively), **Figure, 21 D and 21 F.** Using this second antibody for cathepsin D (from SicGen), the expression levels of both inactive (procathepsin D) and active cathepsin D states were evaluated by western blot, **Figure 21 G and 21 H**. Results show that the ratio between pro and matured cathepsin D is not significantly different between WT and CHM$^{-/-}$ cells.

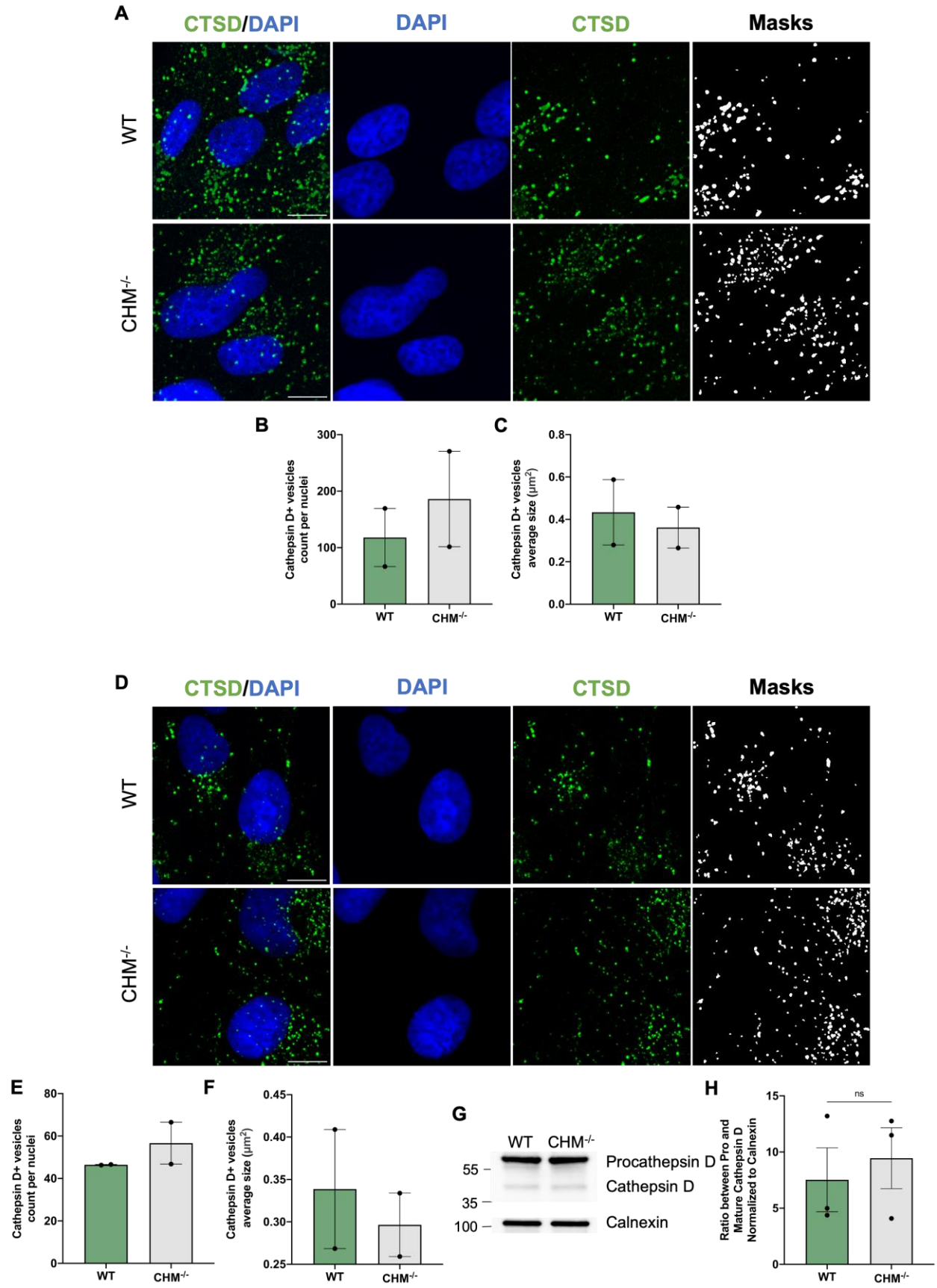

Figure 21. Characterization of lysosomal activity in CHM$^{-/-}$ ARPE-19 cell model. **A)** Immunofluorescence images of cathepsin D marker, CTSD from R&D (green) with nuclei stained with DAPI (blue). Scale bar 10 µm. **B)** Quantification of the number of CTSD+ vesicles per nuclei. Data is presented as Mean ± SEM, representative of n=2 independent experiments. **C)** Average size of CTSD+ vesicles (µm^2). Data is presented as Mean ± SEM, representative of n=2 independent experiments. **D)** Immunofluorescence images of

cathepsin D marker, CTSD from SicGen (green) with nuclei stained with DAPI (blue). Scale bar 10 μm. **E)** Quantification of the number of CTSD+ vesicles per nuclei. Data is presented as Mean ± SEM, representative of n=2 independent experiments. **F)** Average size of CTSD+ vesicles (μm^2). Data is presented as Mean ± SEM, representative of n=2 independent experiments. **G)** Western blot analysis of procathepsin D and cathepsin D (SicGen) expression in whole cell lysates between WT and $CHM^{-/-}$ cells, representative of n=3 independent experiments. Loading control: calnexin. **H)** Graphical representation of WB quantification. Graph of the ratio between pro- and matured cathepsin D normalized to calnexin. Data is presented as Mean ± SEM, representative of n=3. Statistical comparisons were performed using unpaired t-test (ns, not significant).

Lastly, ARPE-19 cells were stained with an anti-cathepsin B antibody, and quantification from immunofluorescence images reveals no difference in the number of puncta between WT and $CHM^{-/-}$ cells, **Figure 22 A and 22 B**, however a tendency for a decrease in the size of Cathepsin B+ vesicles in the $CHM^{-/-}$ cells was observed, with mean sizes of 0.5487 μm^2 and 0.3735 μm^2 for WT and $CHM^{-/-}$, respectively, **Figure 22 A and 22 C.** However, since the results only represent one independent experiments, no further conclusions can be drawn at this point.

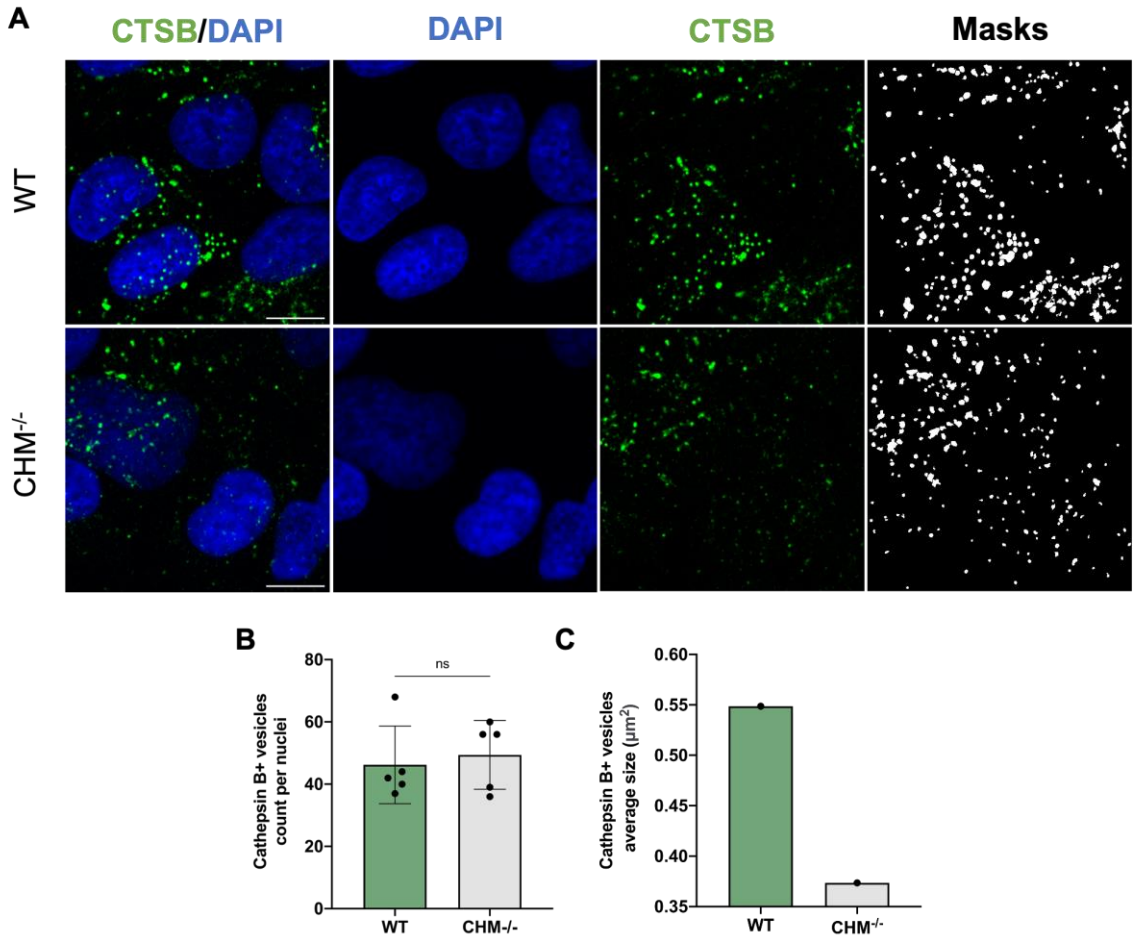

Figure 22. No difference in number and size of CTSB+ vesicles in $CHM^{-/-}$ ARPE-19 cell model. A) Immunofluorescence images of cathepsin B+ vesicles, CTSB (green) with nuclei stained with DAPI (blue). Scale bar 10 μm. **B)** Quantification of the number of cathepsin B+ vesicles per nuclei. Data is presented as Mean ± SD, representative of n=1 independent experiment. Statistical comparisons were performed on technical replicates using nonparametric Mann-Whitney test (ns, not significant). **C)** Average size of CTSB+ vesicles (μm^2). The mean vesicle size is presented, representative of n=1 independent experiments.

One of the biggest drawbacks in analysing the staining of cathepsins in fixed cells is the inability to differentiate between active and inactive states, since most antibodies mark the whole cell population of a specific cathepsin independently of its pro or cleaved state. To overcome this, we used a recently published fixable dye, SiR-lysosome[116], that binds specifically to active Cathepsin D and with a short twenty-minute incubation, stains cells in a rather distinguishable and quantifiable manner.

In Figure 23 A and 23 B, the number of active cathepsin D+ puncta were quantified per nuclei, revealing a significant increase (p-value: 0.0494) in CHM$^{-/-}$ cells, suggesting that somehow the absence of REP1 is increasing the number of vesicles with active cathepsin D. No difference is observed in the average size of active cathepsin D+ puncta, with sizes of 0.1913 μm^2 and 0.1956 μm^2 for WT and CHM$^{-/-}$, respectively, **Figure 23 A and 23 C.**

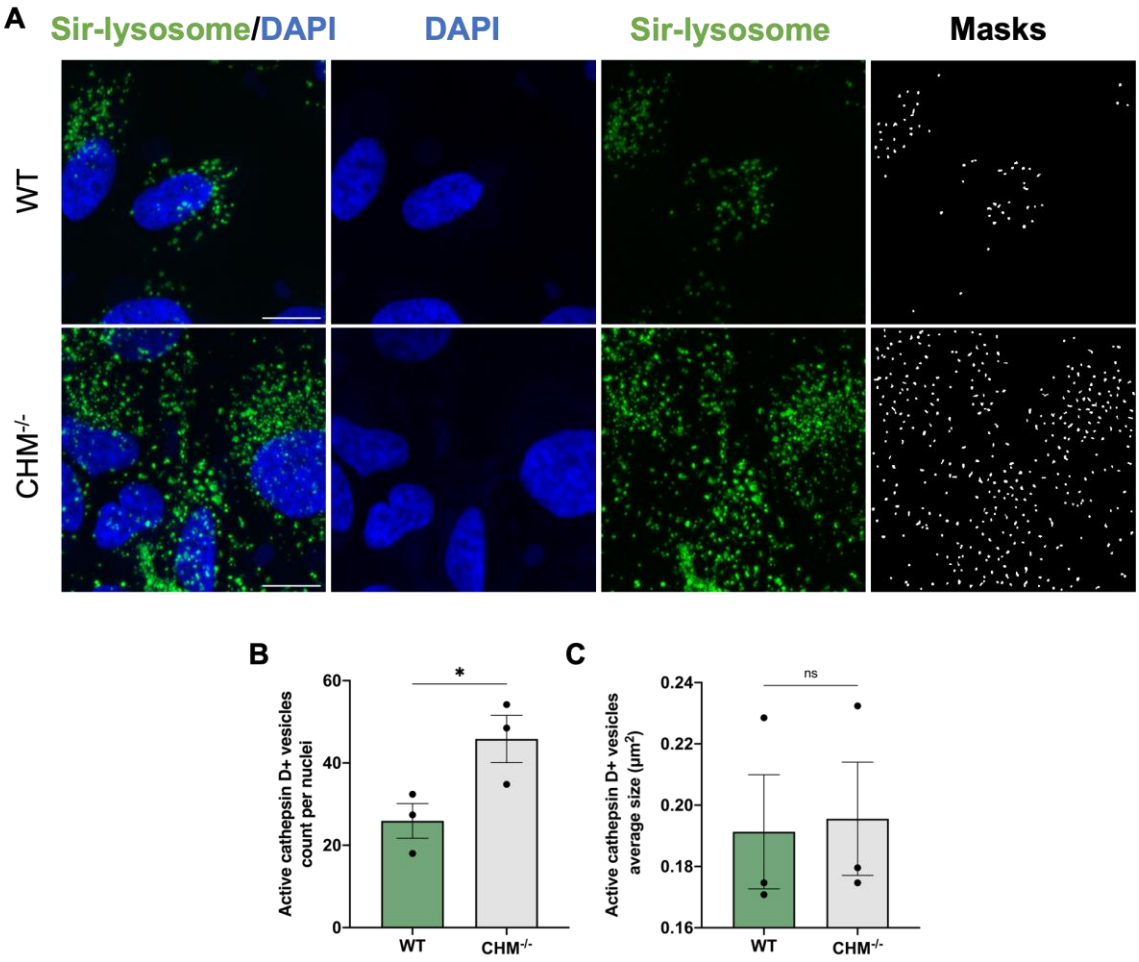

Figure 23. Increase in the levels of active cathepsin D+ vesicles in CHM$^{-/-}$ ARPE-19 cell model. **A)** Immunofluorescence images of active cathepsin D+ vesicles, SiR-lysosome (green) with nuclei stained with DAPI (blue). Scale bar 10 μm. **B)** Quantification of the number of active cathepsin D+ vesicles per nuclei. Data is presented as Mean ± SEM, representative of n=3 independent experiment. Statistical comparisons were performed using unpaired t-test (* P<0.05). **C)** Average size of active cathepsin D+ vesicles (μm^2). Data is presented as Mean ± SEM, representative of n=3 independent experiments. Statistical comparisons were performed using unpaired t-test (ns, not significant).

3.1.4.1. Live imaging observations for Lysosome activity/function in ARPE-19

One of the biggest advantages of ARPE-19 cell line is the ability to do live imaging microscopy to trace different live dyes throughout the cell. We decided to analyse two different dyes, Magic Red Cathepsin B and Magic Red Cathepsin L assay kits, where Magic Red substrate easily permeates the cell membrane as well as other compartments and if cleaved by the given cathepsin, fluoresces.

Cells stained with Magic Red Cathepsin B, **Figure 24 A and 24 B,** showed no difference in the number of active Cathepsin B+ puncta, which is in accordance with the analysis done using fixed cathepsin B antibody staining. Since the intensity of fluorescence is proportional to cathepsin activity within the cell, the maximum intensity was quantified for each positive vesicle, **Figure 24 A and 24 C**. No differences were observed between WT and $CHM^{-/-}$ cells. Regarding Magic Red Cathepsin L, there was no difference in the number of vesicles, however, to reach a definite conclusion more independent experiments are needed, **Figure 24 D and 24 E**. The maximum intensity of cathepsin L+ vesicles show a slight decrease in $CHM^{-/-}$ cells compared to WT cells; however, such results need to be repeated, **Figure 24 D and 24 F**. Western blot analysis of pro- and matured cathepsin L, revealed a slight tendency (although not significant) towards a higher ratio between pro- and matured cathepsin L, suggesting that $CHM^{-/-}$ cells may have higher levels of (inactive) Procathepsin L, **Figure 24 G and 24 H.**

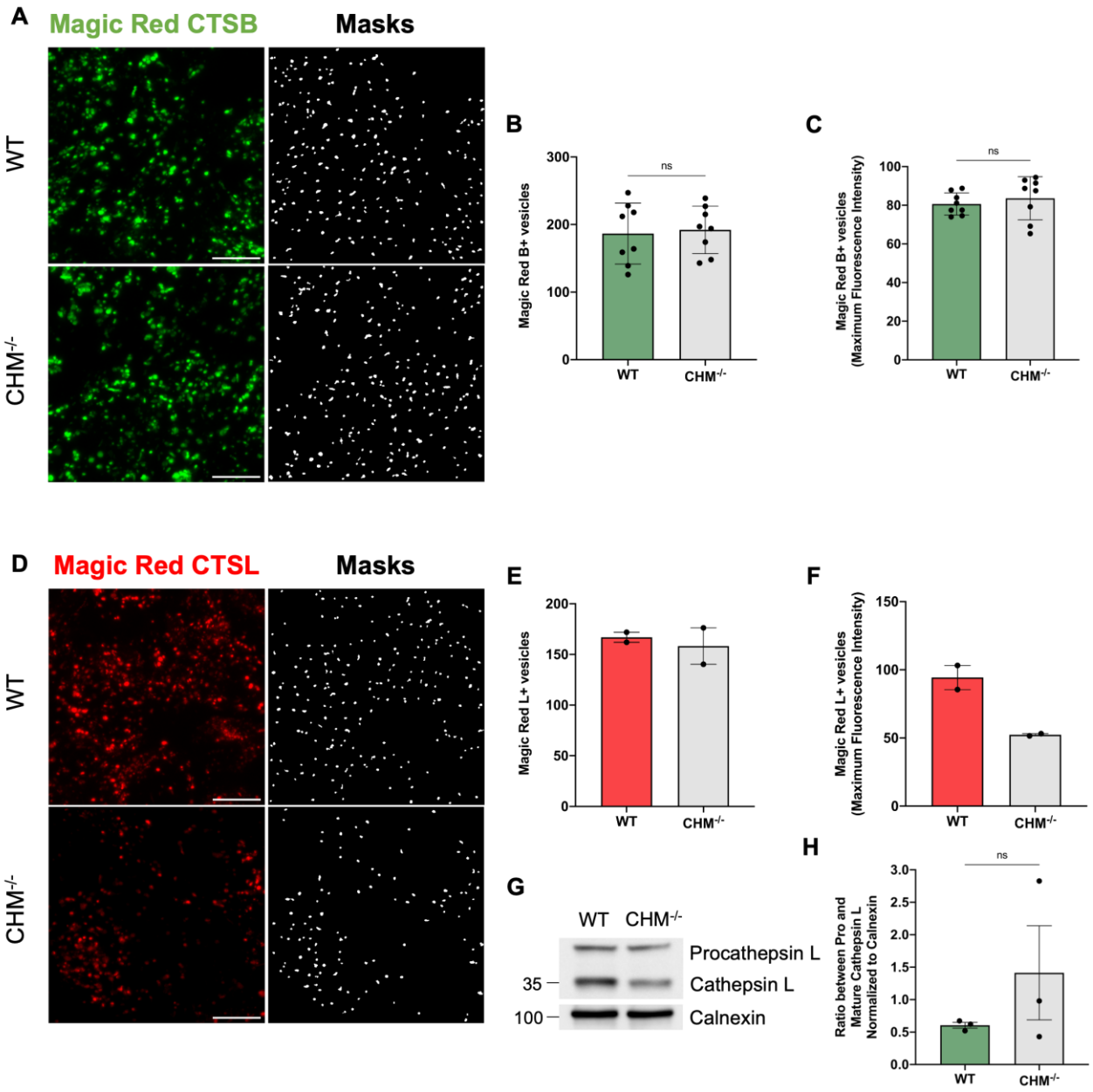

Figure 24. Live imaging analysis of lysosome activity in CHM$^{-/-}$ ARPE-19 cell model. **A)** Live imaging of active cathepsin B+ vesicles, marked with Magic Red CTSB (green). Scale bar 10 μm. **B)** Quantification of the number of active cathepsin B+ vesicles. Data is presented as Mean ± SD, representative of n=1 independent experiment. Statistical comparisons were performed on technical replicates using unpaired t-test (ns, not significant). **C)** Quantification of maximum fluorescence intensity of Magic Red B+ vesicles. Data is presented as Mean ± SD, representative of n=1 independent experiments. Statistical comparisons were performed on technical replicates using unpaired t-test (ns, not significant). **D)** Live imaging of active cathepsin L+ vesicles, marked with Magic Red CTSL (red). Scale bar 10 μm. **E)** Quantification of the number of active cathepsin L+ vesicles. Data is presented as Mean ± SEM, representative of n=2 independent experiment. **F)** Quantification of maximum fluorescence intensity of Magic Red L+ vesicles. Data is presented as Mean ± SEM, representative of n=2 independent experiments. **G)** Western blot analysis of procathepsin L and cathepsin L expression in whole cell lysates between WT and CHM$^{-/-}$ cells, representative of n=3 independent experiments. Loading control: calnexin. **H)** Graphical representation of WB quantification. Graph of ratio between pro- and matured cathepsin D normalized to calnexin Data is presented as Mean ± SEM, representative of n=3. Statistical comparisons were performed using unpaired t-test with Welch's correction (ns, not significant).

To ensure the correct functioning of cathepsins within lysosomes, the internal pH needs to be tightly regulated and maintained in the acidic range 4.5-5.5[117]. One of the most common lysosomal pH probes is LysoTracker, a fluorophore that permeates cellular membranes and fluoresces only in an acidic environment, thus allowing the staining and tracking of acidic vesicles within cells. However, one must be careful in using LysoTracker to study lysosomes since the total fluorescence seen may not all be seen within acidic lysosomes but could be within other acidic compartments[118], such as, other elements of the endo-lysosomal pathway, like mildly acidic late endosomes and secretory vesicles coming from the Golgi apparatus[119,120].

ARPE-19 cells cultured in microchamber slides and briefly incubated with LysoTracker, showed no difference in the number of puncta between WT and CHM$^{-/-}$ cells, suggesting that the total amount of acidic vesicles is not affected by the absence of REP1, **Figure 25 A and 25 B.**

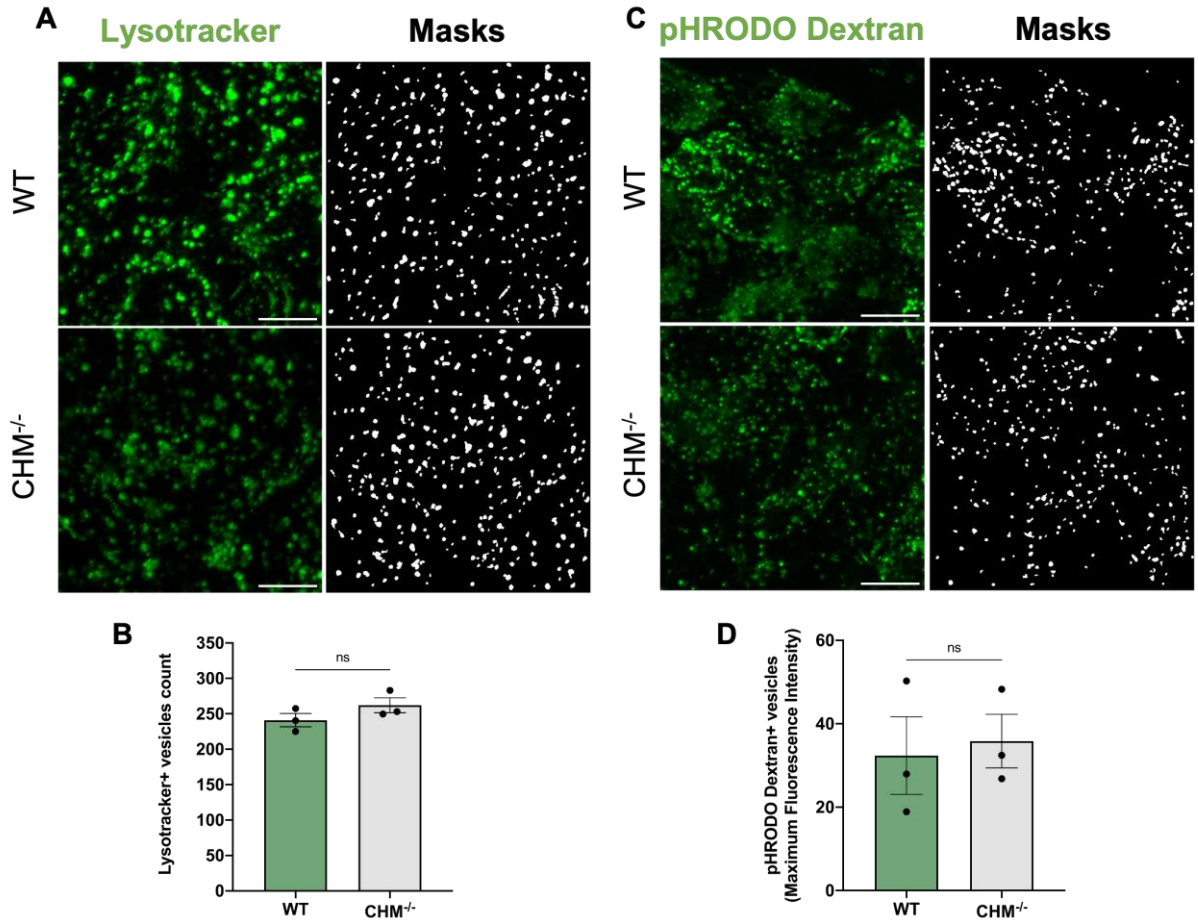

Figure 25. Characterization of vesicle acidity in CHM-/- ARPE-19 cell model. **A)** Live imaging analysis of whole cell acidic vesicles marked with LysoTracker (green). Scale bar 10 μm. **B)** Quantification of the number of LysoTracker+ vesicles. Data is presented as Mean ± SEM, representative of n=3 independent experiments. Statistical comparisons were performed using unpaired t-test (ns, not significant). **C)** Live imaging analysis of late endosomes/lysosomes marked with pHRODO Dextran (green) incubated overnight and chased for 3 hours before imaging. Scale bar 10 μm. **D)** Quantification of maximum fluorescence intensity of pHRODO Dextran+ vesicles. Data is presented as Mean ± SEM, representative of n=3 independent experiments. Statistical comparisons were performed using unpaired t-test (ns, not significant).

To overcome the difficulty of LysoTracker to exclusively stain lysosomes, we used pHRODO Dextran, a pH sensitive fluorophore conjugated with 10kDa Dextran that enters the cells via endocytosis. Thus, by choosing a specific chase time we can analyse the acidification of the lysosomal population exclusively. The

fluorescence intensity of pHRODO Dextran is also pH sensitive and increases with decreasing pH, allowing for the relative measurement of the pH within lysosomes. In **Figure 25 C**, cells were incubated overnight with pHRODO Dextran, washed, and chased for three hours before imaging, so that all the dye that entered the endo-lysosomal pathway accumulates only in lysosomes. The maximum intensity was measure for each individual vesicle observed and quantification revealed no significant difference (p-value: 0.7744) in fluorescence intensity in control and $CHM^{-/-}$ cells, with average values of 32.28 and 35.85 in WT and $CHM^{-/-}$, respectively, **Figure 25 C and 25 D.** Unlike previous quantifications where the number of positive vesicles was also analysed, in pHRODO Dextran live imaging experiments we decided to only look at the fluorescence intensity due to the nature of the dye and the structure it is staining, the lysosomes. With fixed live imaging we can have a clearer result in the number of vesicles per nuclei, whereas in live imaging experiments the absence of nuclei staining may generate bias in the results. Regarding size, we decided that the quantification of vesicle size in live imaging experiments could lead to error since, cells and organelles are constantly moving and although z-stacks are acquired in the fastest way possible, we feared that between frames some vesicles could move and appear as a line and therefore, not accurate for size measurement.

3.1.5. POS phagocytosis and elimination in ARPE-19 CHM model

One of the most important functions of the RPE is to daily phagocytose POS, a crucial step for a healthy vision. However, with time the continuously burden of phagocytosis causes strain to lysosomes leading to accumulation of lipofuscin granules, deposits of oxidized proteins, lipids, and metals. Such events are seen in conditions such as AMD. Given its genetic aetiology, CHM patient RPEs have, from the start, a disadvantage in the health of the endo-lysosomal pathway, thus we wanted to uncover the impact of REP1 loss in the degradation of POS. In our lab, POS isolated from porcine eyes [112] are fed at high amount to RPE cells, to ensure phagocytic system saturation[46.] Using this system, we observe the accumulation of endogenously produced autofluorescent granules, which arise from undigested POS. In contrast, in most other studies, POS are fluorescently labelled and traced within the cells[64,121]. Using this unique protocol, we can visualize and quantify autofluorescent granules (AFGs), which mimic *in vivo* lipofuscin, as early as just a few hours post –POS-feeding[46].

Thus, in order to establish if our $CHM^{-/-}$ model has defect in POS degradation, we performed experiments to observe AFG accumulation after being challenged with POS for 4 hours and chased for 72 hours, by FACS, **Figure 26 A**. Three independent experiments measuring the % of 488 positive cells revealed a 6-fold increase in $CHM^{-/-}$ cells compared to WT (when measured by FACS analysis), **Figure 26 B.** This result suggests that there is indeed a defect in the correct digestion of POS in our cell system as there was a significant increase in the number of cells with AFGs.

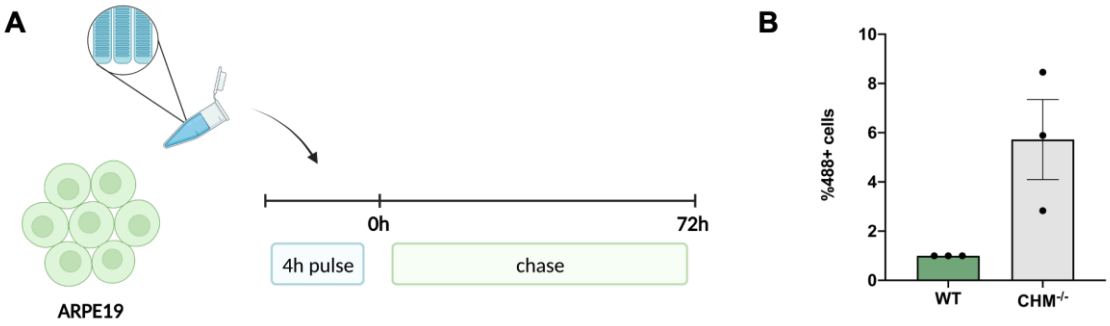

Figure 26. Accumulation of autofluorescent granules (AFGs) in CHM$^{-/-}$ ARPE-19 cell model. **A)** Schematic representation of photoreceptor outer segments (POS) feeding in ARPE-19. Cells are stimulated with POS for 4 hours, afterwards vigorously washed and chased for 72h. **B)** Quantification of % of 488+ cells using FACS. Data is presented as Mean ± SEM, representative of n=3 independent experiments (fold change).

3.1.5.1. Autofluorescent granules (AFGs) accumulation in CHM cells

After verifying that there were more cells with AFGs in them in CHM$^{-/-}$ cells when compared to WT, it was of great importance to be able to quantify the number of these granules, since RPE cells can have more than one granule. ARPE-19 cells were fed for 4 hours and chased for both 24 hours and 72 hours, **Figure 27 A**. The number of positive AFGs per nuclei was quantified in three independent experiments. At 24 hours, results show a significant increase in the AFGs count, **Figure 27 B.** Regarding size, CHM$^{-/-}$ cells have smaller AFG average sizes compared to WT, 0.8363 μm^2 and 1.053 μm^2, respectively, **Figure 27 C.** At 72 hours, the significant accumulation of AFGs in CHM$^{-/-}$ is maintained as well as the reduction in their size when compared to WT cells, 0.8284 μm^2 and 0.9687 μm^2, respectively, however this difference is not significant at this time point, **Figure 27 D and 27 E.**

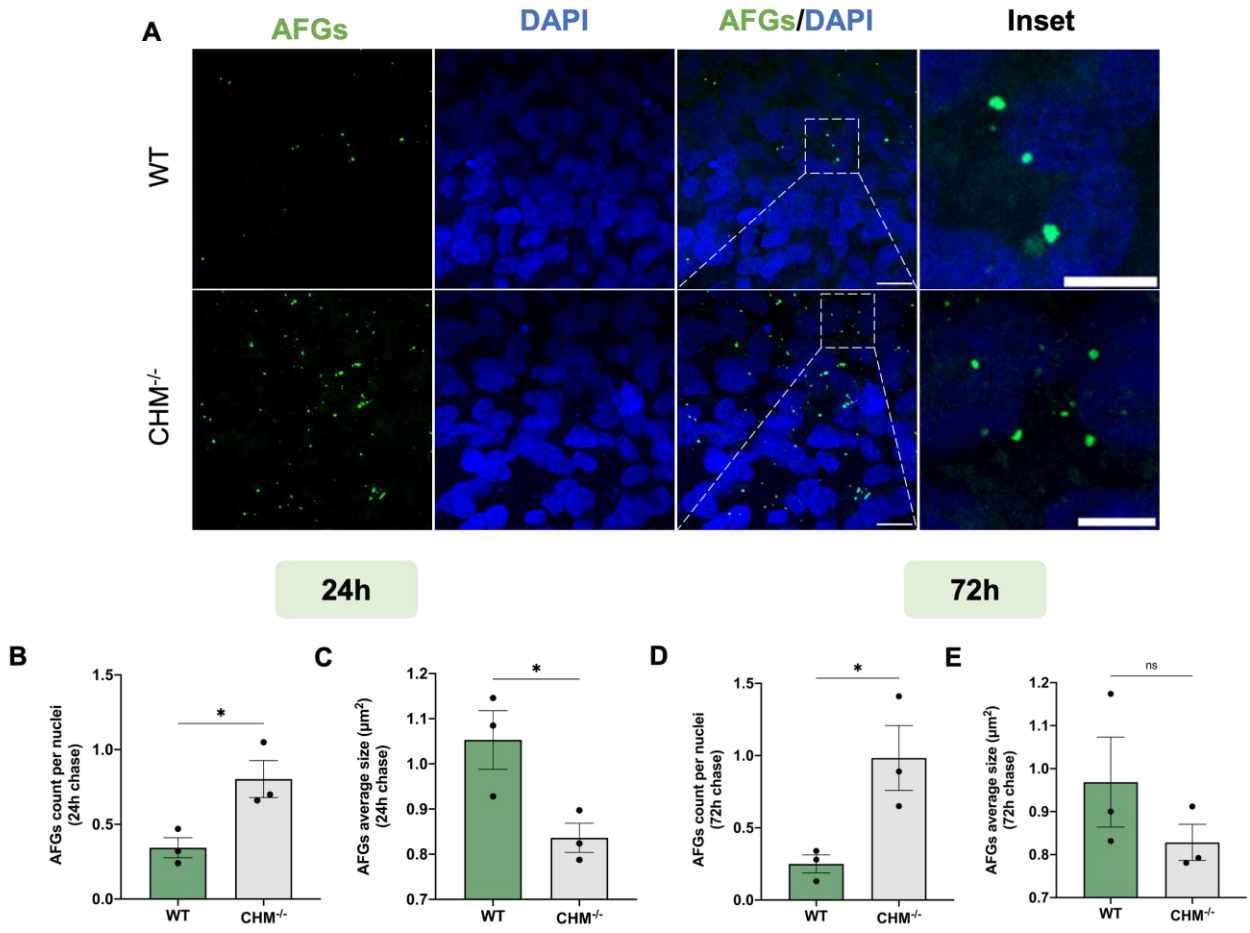

Figure 27. AFGs accumulate at 24h and 72h post-feeding in CHM$^{-/-}$ ARPE-19 cell model. **A)** Immunofluorescence images of AFGs (green) 72h post-feeding, with nuclei stained with DAPI (blue). Scale bar 20 μm. Inset Scale bar 10 μm. **B)** Quantification of the number of AFGs per nuclei 24h post-feeding. Data is presented as Mean ± SEM, representative of n=3 independent experiment. Statistical comparisons were performed using unpaired t-test (* P<0.05). **C)** Average size of AFGs (μm^2) 24h post-feeding. Data is presented as Mean ± SEM, representative of n=3 independent experiments. Statistical comparisons were performed using unpaired t-test (* P<0.05). **D)** Number of AFGs per nuclei 72h post-feeding. Data is presented as Mean ± SEM, representative of n=3 independent experiment. Statistical comparisons were performed using unpaired t-test (* P<0.05). **E)** Average size of AFGs (μm^2) 72h post-feeding. Data is presented as Mean ± SEM, representative of n=3 independent experiments. Statistical comparisons were performed using unpaired t-test (ns, not significant).

Knowing that at 24 hours a pronounced accumulation of AFGs is already observed in CHM$^{-/-}$ cells, we wanted to further investigate how long after feeding were CHM$^{-/-}$ cells burdened with the accumulation of these toxic granules. To do so, we performed an experiment where cells were fixed at different time-points after a 4-hour feeding, **Figure 28 A**. After a short 4-hours, AFGs are already observed and significantly accumulate in CHM$^{-/-}$ cells compared to WT, suggesting that the significant accumulation of AFGs occurs very early on during the phagocytosis process in CHM$^{-/-}$ ARPE-19 cells, **Figure 28 B-F.**

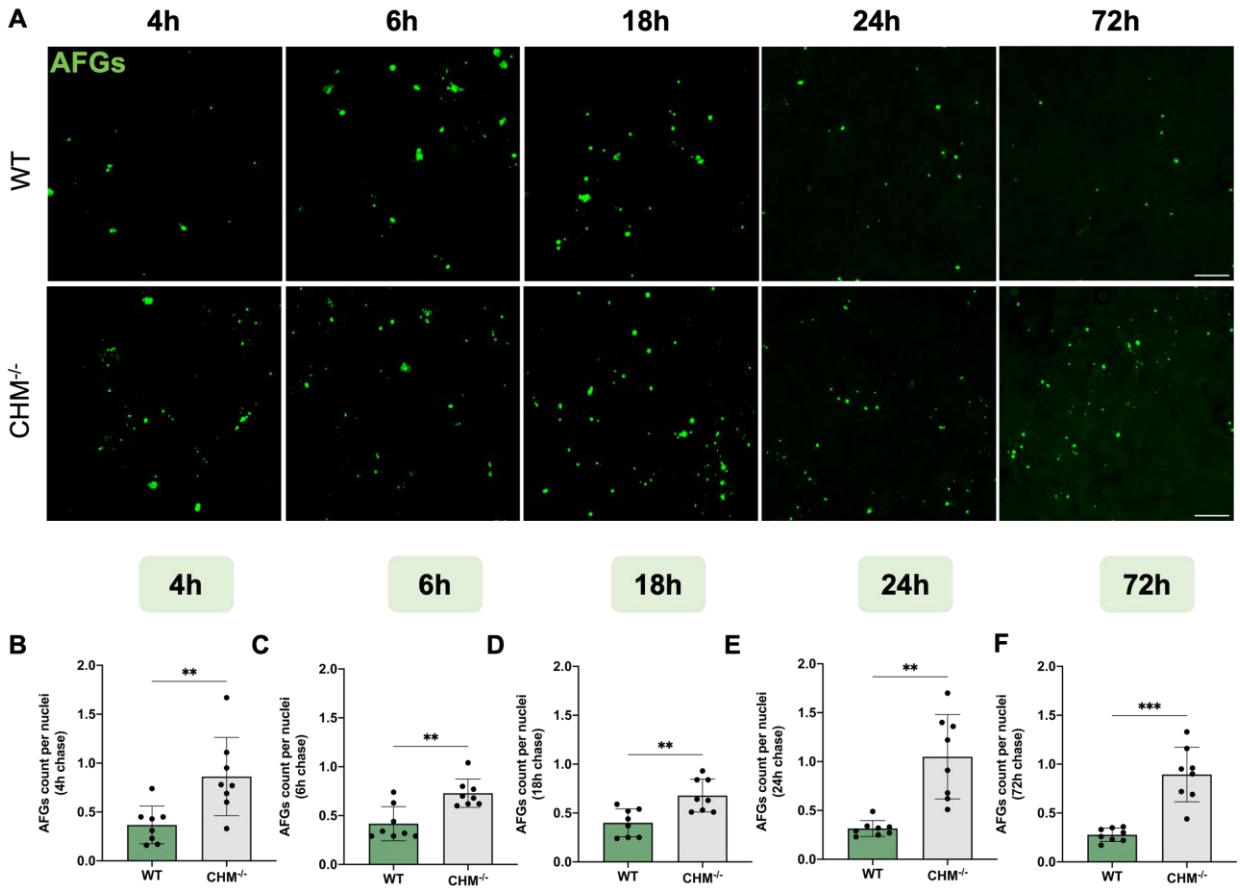

Figure 28. Accumulation of AFGs over time in CHM$^{-/-}$ ARPE-19 cell model. A) Immunofluorescence images of AFGs (green) in different post-feeding time points. Scale bar 20 μm. **B)** Quantification of the number of AFGs granules per nuclei 4h post-feeding. Data is presented as Mean ± SD, representative of n=1 independent experiment. Statistical comparisons were performed on technical replicates using unpaired t-test (** P<0.01). **C)** Number of AFGs granules per nuclei 6h post-feeding. Data is presented as Mean ± SD, representative of n=1 independent experiment. Statistical comparisons were performed on technical replicates using nonparametric Mann-Whitney test (** P<0.01). **D)** Number of AFGs granules per nuclei 18h post-feeding. Data is presented as Mean ± SD, representative of n=1 independent experiment. Statistical comparisons were performed on technical replicates using unpaired t-test (** P<0.01). **E)** Number of AFGs granules per nuclei 24h post-feeding. Data is presented as Mean ± SD, representative of n=1 independent experiment. Statistical comparisons were performed on technical replicates using unpaired t-test with Welch's correction (** P<0.01). **F)** Number of AFGs granules per nuclei 72h post-feeding. Data is presented as Mean ± SD, representative of n=1 independent experiment. Statistical comparisons were performed on technical replicates using unpaired t-test with Welch's correction (*** P<0.001).

3.1.5.2. AFGs interact with late stages of the endo-lysosomal pathway

After the accumulation of AFGs in CHM$^{-/-}$ cells was verified, we wanted to analyse the interaction between AFGs and different vesicles along the endo-lysosomal pathway, **Figure 29 A and 29 B.** An interaction is found between CD63+ vesicles and AFGs, **Figure 29 B**, as well as an interaction of LAMP1+ vesicles and AFGs in both WT and CHM$^{-/-}$ cells, **Figure 29 A**, suggesting that AFGs resultant from incomplete POS digestion are surrounded by lysosomes, even in CHM$^{-/-}$ cells. Such observation was also demonstrated in hfRPE cells which showed that AFGs contains marker of lysosomes, such as LAMP1 and cathepsin D[46].

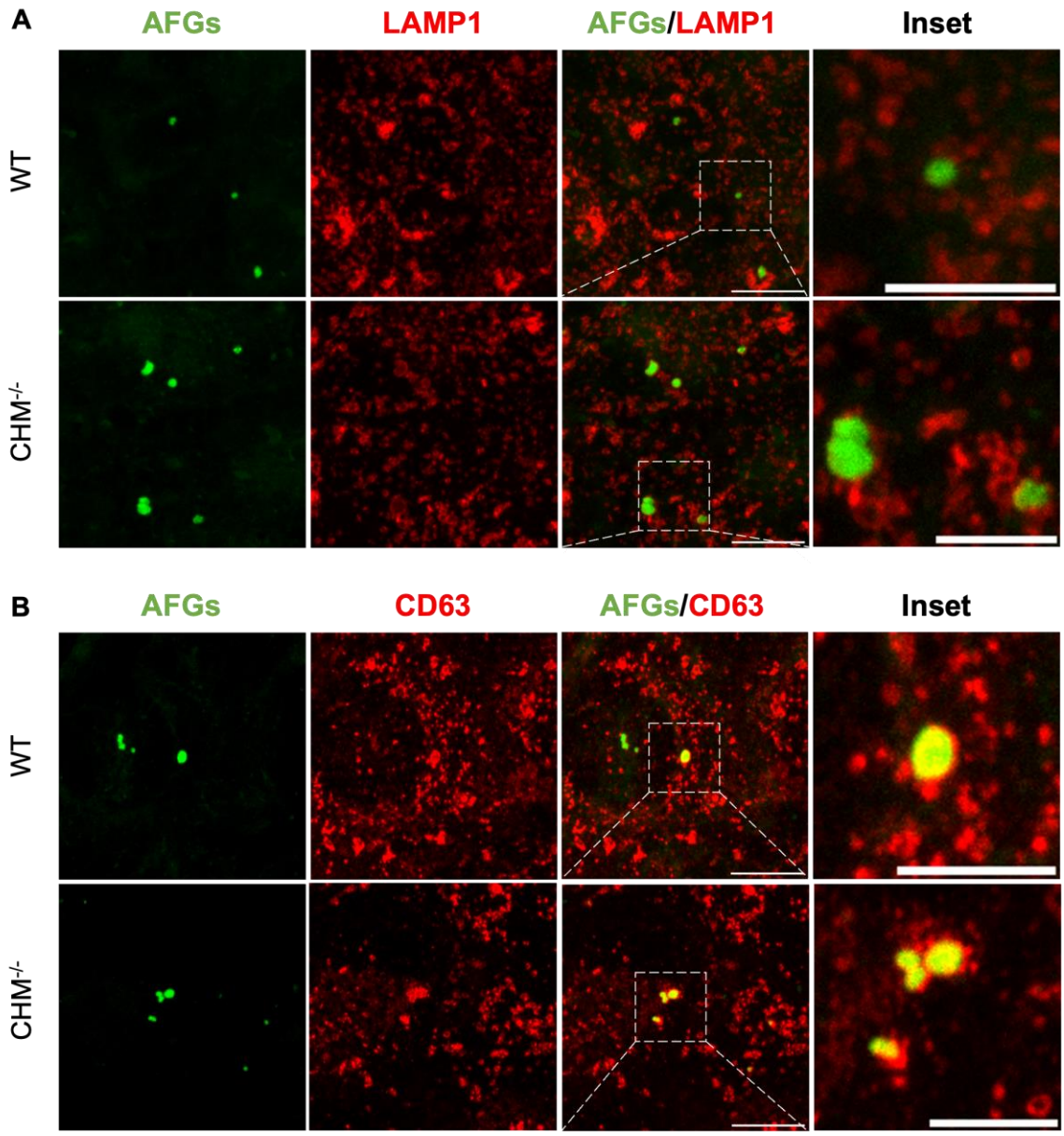

Figure 29. Interaction of AFGs with late endosome/lysosome markers in CHM$^{-/-}$ ARPE-19 cell model. **A)** Immunofluorescence images of AFGs (green) 72h post-feeding with lysosomal markers, LAMP1 (red). Scale bar 10 μm. Inset Scale bar 5 μm. **B)** Immunofluorescence images of AFGs (green) 72h post-feeding with multivesicular bodies (MVBs) marker, CD63 (red). Scale bar 10 μm. Inset Scale bar 5 μm.

To be able to visualize such interaction in more detail, a live imaging experiment was conducted where cells were fed with POS for 4 hours and then incubated with LysoTracker 72 hours post-feeding, **Figure 30 A**. Results show that LysoTracker+ vesicles are highly dynamic, moving quickly between 2 second frames, in both WT and CHM$^{-/-}$ cells. Also, LysoTracker+ vesicles showed a kiss-and-run type of movement, where vesicles touch the AFGs and quickly move away, represented by the white arrows, showing that acidic vesicles, such as lysosomes, present kiss-and-run movements, possibly indicating that the cell is continuously trying to resolve AFGs accumulation, but in some cases, in unable to do so.

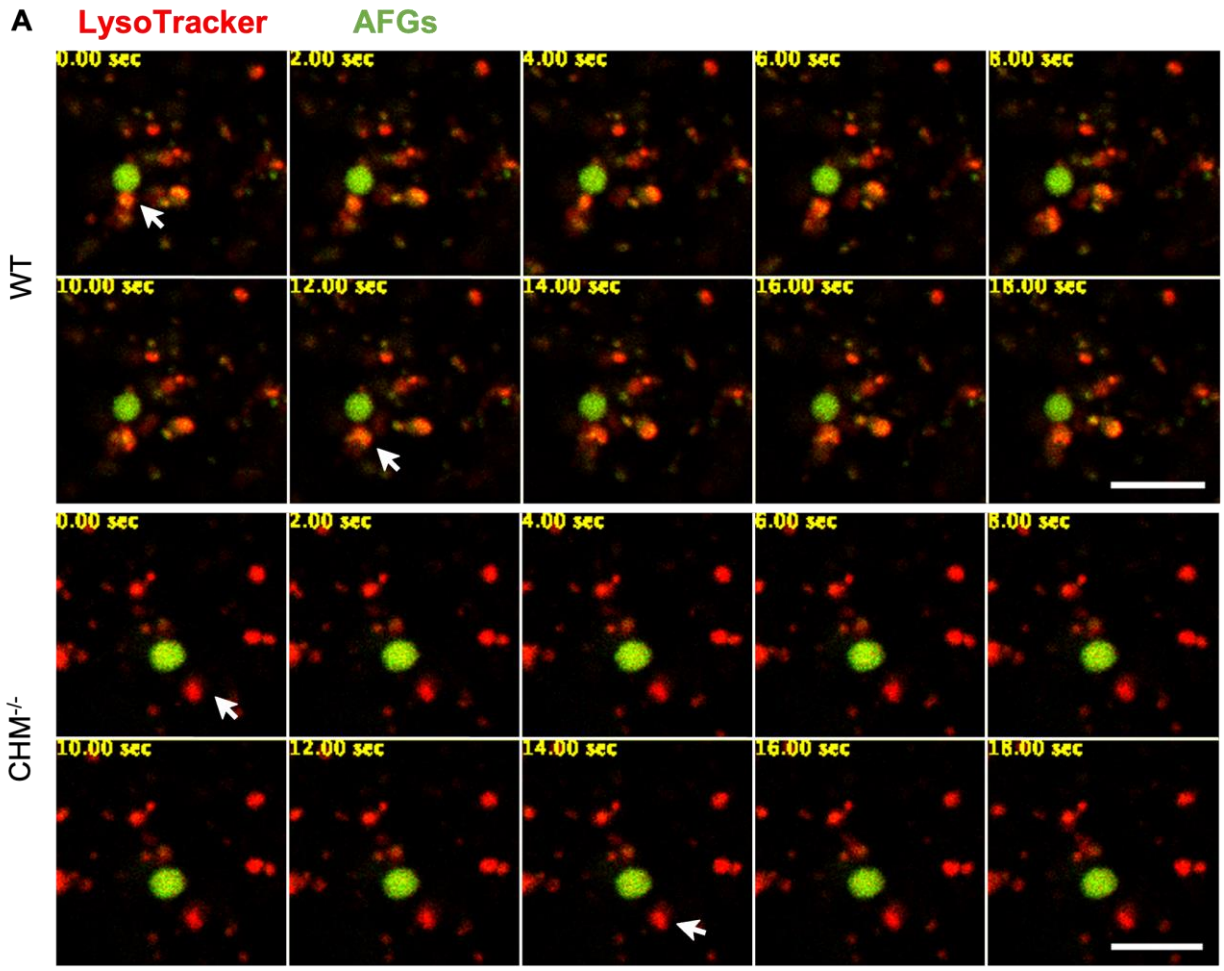

Figure 30. Live imaging of AFGs 72h post-feeding with LysoTracker+ vesicles in CHM$^{-/-}$ ARPE-19 cell model. **A)** Immunofluorescence images of AFGs (green) 72h post-feeding with cellular acidic vesicles marker, LysoTracker (red). Scale bar 5 μm.

3.1.6. CHM and other cellular organelles

Since REP1, the coding product of the *CHM* gene, is responsible for the prenylation of multiple Rab proteins, and is tightly correlated with the endocytic pathway in RPE as we have described in the previous sections, we also wanted to investigate whether CHM was affecting other cellular organelles, such as mitochondria, where correct Rab function is also important. A mitochondrial dysfunction disease, Kearns-Sayre syndrome (KSS), reveals retinal atrophy similar to late stages of CHM. This condition is caused by mitochondrial DNA deletions which results in defects in oxidative phosphorylation[56]. Thus, we wanted to check whether the mitochondrial network is affected by the absence of REP1. To do so, we stained both WT and CHM$^{-/-}$ cells with TOM20, a common mitochondrial marker and measured the total area occupied by the mitochondrial network, **Figure 31 A**. Quantification showed a tendency towards higher areas occupied in CHM$^{-/-}$ cell, with total areas of 46.69 μm^2 and 91.68 μm^2 in WT and CHM$^{-/-}$ cells, respectively, **Figure 31 A and 31 B,** suggesting that in CHM the mitochondrial network is more dispersed and that the absence of REP1could be affecting mitochondrial homeostasis. However, more experiments are needed to make further conclusions. Protein expression by western blot, **Figure 31 C and 31 D**, reveals no significant difference in the expression of TOM20 between WT and CHM$^{-/-}$ cells, suggesting that the higher total areas occupied by the

mitochondria network is not due to higher expression levels of TOM20 protein but to a change in the spatial organization of mitochondria within CHM$^{-/-}$ cells.

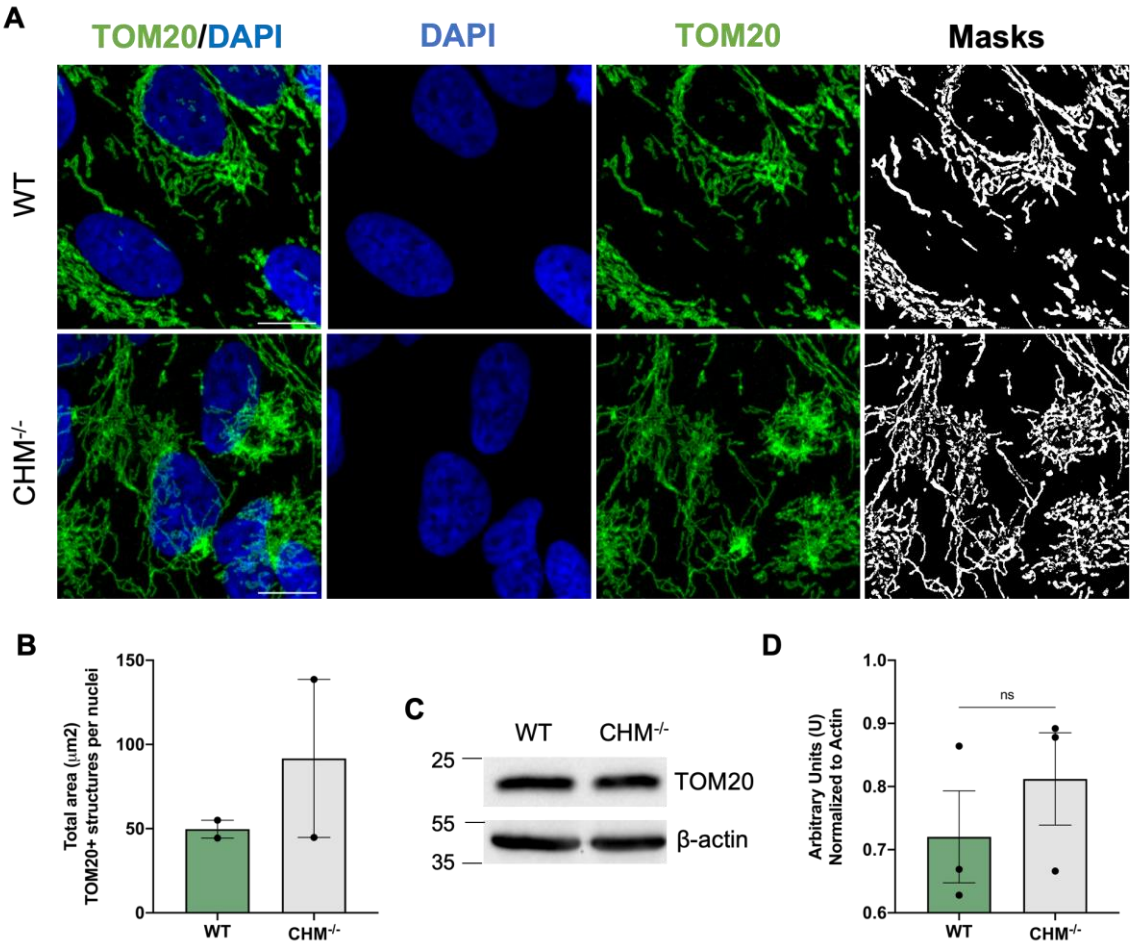

Figure 31. Effect of REP1 absence in the mitochondrial network in CHM$^{-/-}$ ARPE-19 cell model. **A)** Immunofluorescence images of mitochondrial marker, TOM20 (green) with nuclei stained with DAPI (blue). Scale bar 10 µm. **B)** Quantification of the total area (µm^2) occupied by the mitochondrial network per nuclei. Data is represented as Mean ± SEM, representative of n=2 independent experiment. **C)** Western blot analysis of TOM20 expression of whole cell lysates between WT and CHM$^{-/-}$ cells, representative of n=3 independent experiments. Loading control: β-actin. **D)** Graphical representation of WB quantification. Normalized to β-actin. Data is presented as Mean ± SEM, representative of n=3. Statistical comparisons were performed using unpaired t-test (ns, not significant).

3.2. hiPSc-RPE as a model for CHM

3.2.1. Characterization of hiPSc-RPE as a model for choroideremia

After observing striking phenotypes in the endo-lysosomal pathway in CHM ARPE-19 cells, we wanted to confirm such results in a model that more closely resembles the human RPE found in the retina. There are several alternatives available, and, in our lab, we implemented the Foltz & Clegg, 2017 protocol for the generation of human derived hiPSc-RPE cells within 75-days, with a 14-day differentiation stage. The use of differentiated RPE from hiPSc is a precise and technically challenging method with a low yield compared to that of the ARPE-19 cell model, however the generated RPE more closely resembles the morphological and functional characteristics of the human RPE cell, known as the 5 P´s rule: RPE cells need to have phagocytic capacity, a post-mitotic phenotype after differentiation, polarization between the apical and the basolateral side, pigmentation and a polygonal shape. The differentiation protocol implemented in our lab[110] has been checked for most of these characteristics, except POS phagocytosis (which needs to be optimized), making this an excellent cellular model of RPE[111].

To study CHM, we obtained hiPSc cells from a healthy donor (RBi001-A), a CHM patient (Patient CHM$^{c.808C>T}$), and in the lab with was also previously produced a CRISPR-Cas9 CHM knockout isogenic line generated from healthy cells (RBi001-A CHM$^{c.809insC}$). More recently, an isogenic line using patient cells with the corrected mutation has been developed previously by Daniela Oliveira[111] and is currently being tested to confirm the correct restauration of REP1 expression. The establishment of isogenic lines, in parallel to the use of a healthy and patient donor, is essential to guarantee some control of the genetic background of the cells used, to warrant that any phenotype found is due to the absence of REP1 and not due to polymorphisms between individuals.

In **Figure 32 A**, the sequencing results are shown for both healthy and patient hiPSc cells, as well as three clones which we wanted to confirm if they are indeed isogenic lines from patient cells with a corrected mutation. Sequencing results show that clone 2_1_9 and clone 4_3 have been successfully corrected in the CHM gene, and the REP1 protein is correctly produced as confirmed by WB analysis. However, the sequencing of clone 2_1_8 resulted in inconclusive results, with a complete change in the gene sequence of CHM. WB analysis also reveal a faint expression of REP1 compared to the other two clones, suggesting that the correction was not efficient. Regarding control and patient cells, as well as the previously established isogenic line, the presence/absence of REP1 was verified and confirmed, **Figure 32 B.**

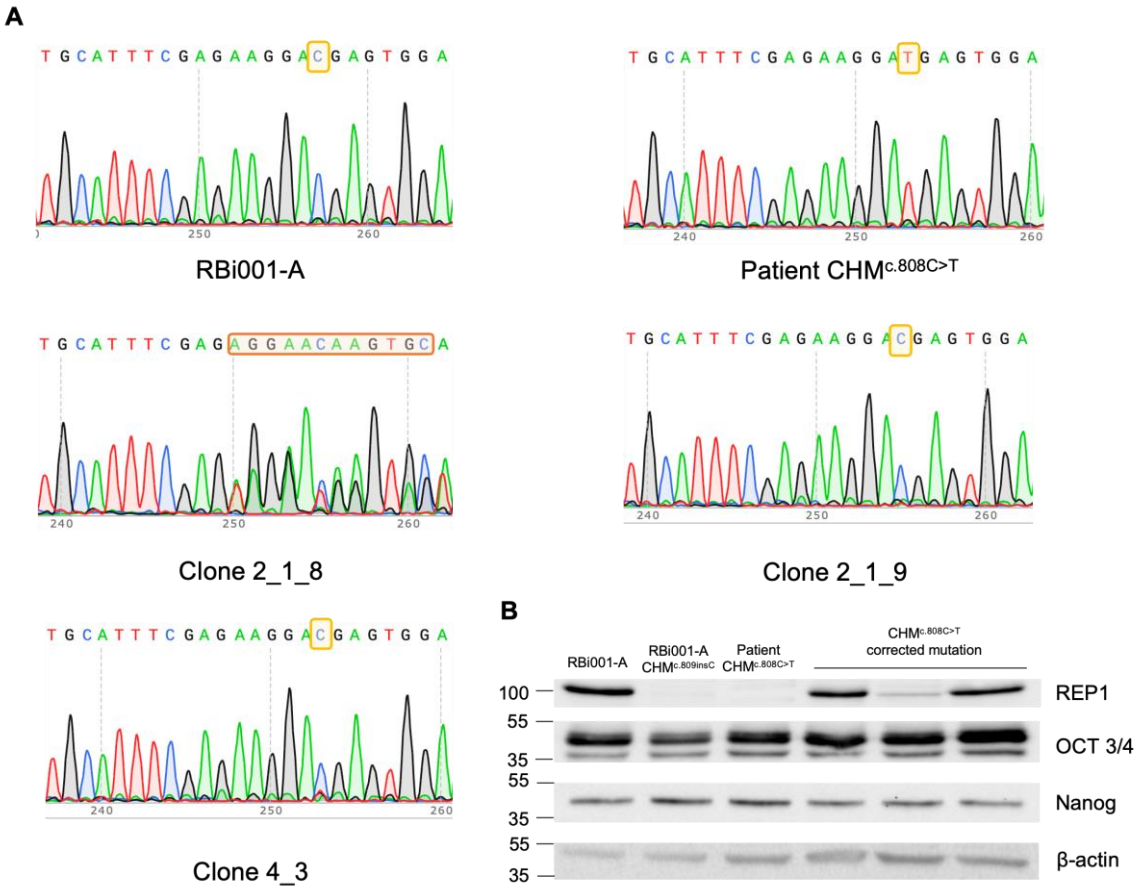

Figure 32. Characterization of CHM and control hiPSc cells. **A)** Schematic representation of Sanger sequencing of healthy hiPSc cells (RBi001-A), patient hiPSc (Patient CHM$^{c.808C>T}$) and isogenic controls generated with CRISPR/Cas9 corrected mutation derived from patient hiPSc cells (Clone 2_1_8, Clone 2_1_9 and Clone 4_3). **B)** Western blot analysis of REP1 and different pluripotent markers, OCT 3/4 and Nanog expression levels between the different hiPSc cell clones. Healthy cells (RBi001-A) in lane 1, isogenic mutant (RBi001-A CHM$^{c.809insC}$) in lane 2, CHM patient cells (Patient CHM$^{c.808C>T}$) in lane 3, isogenic control clone 4_3 in lane 4, isogenic control clone 2_1_8 in lane 5 and isogenic control clone 2_1_9 in lane 6. Data representative of n=1 independent experiment. Loading control: β-actin.

After differentiation, we tested different RPE characteristics starting with the pigmentation levels. To do so, we used PMEL antibody which stains the premelanosomal protein, which is found in the lumen of melanosomes[122], **Figure 33 A**. Previous results from Daniela Oliveira[111], showed a difference in the pigmentation state between control and CHM RPE cells when cells reached passage 1 in the differentiation protocol, however quantification of the fluorescence intensity of PMEL did not show a significant difference, **Figure 33 A and 33 B**. Thus, the visual difference observed may be due to different types of melanin. Additionally, the expression of REP1 is not affected by the differentiation protocol, with cells from healthy donors expressing REP1, and both patient and isogenic mutant cells showing an absence of REP1, **Figure 33 C.**

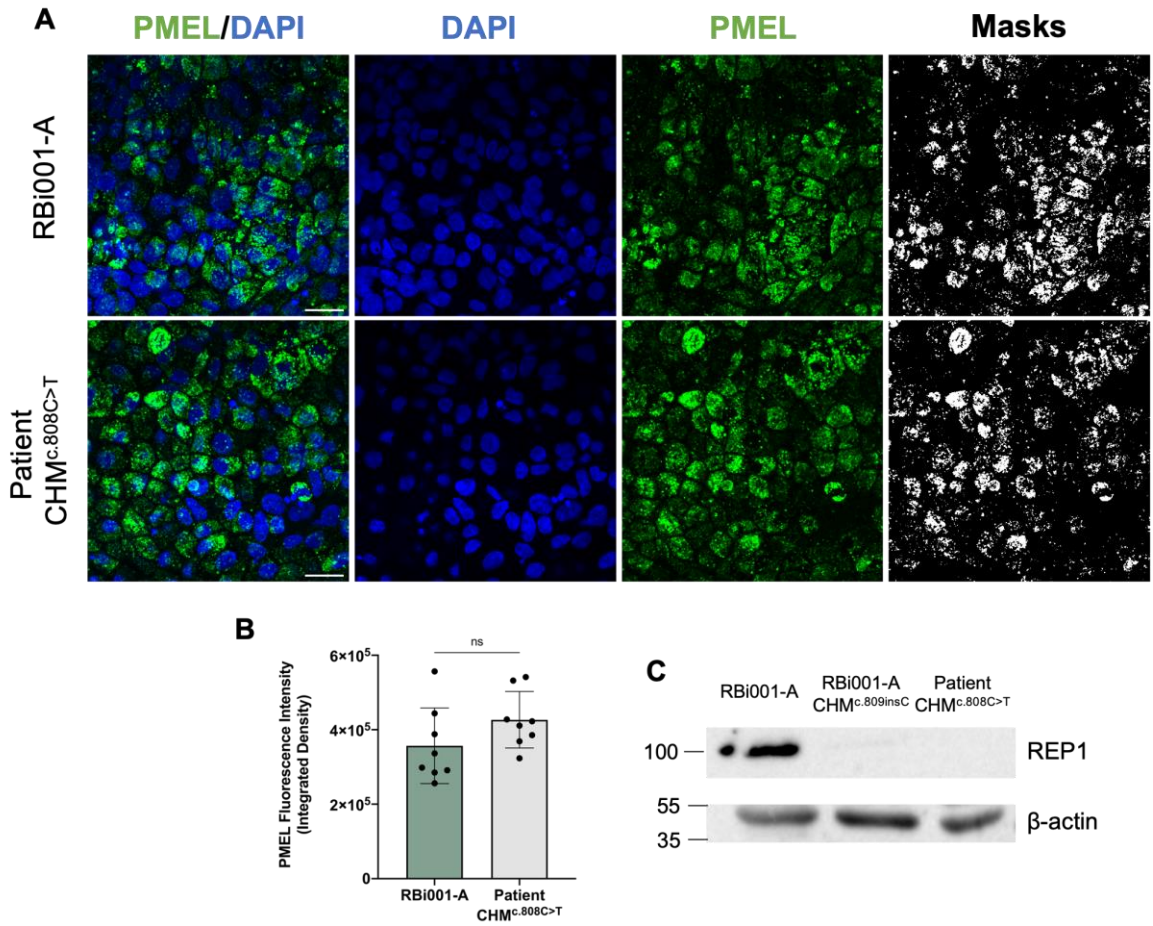

Figure 33. Characterization of differentiated hiPSc-RPE model in control and CHM cells. **A)** Immunofluorescence images of PMEL (green), marks premelanosomal protein within melanosomes, with nuclei stained with DAPI (blue). Scale bar 20 μm. **B)** Quantification of PMEL fluorescence intensity using integrated density. Data is represented as Mean ± SD, representative of n=1 independent experiment. Statistical comparisons were performed on technical replicates using unpaired t-test (ns, not significant). **C)** Western blot analysis of REP1 expression in whole cell lysates between healthy (RBi001-A) and CHM (RBi001-A CHM$^{c.809insC}$ and Patient CHM$^{c.808C>T}$) cells, representative of n=3 for RBi001-A and Patient CHM$^{c.808C>T}$ and n=1 for RBi001-A CHM$^{c.809insC}$. Loading control: β-actin.

Another important characteristic of RPE cells is their distinguishable morphology, showing polygonal shaped cells tightly joined together by tight junctions forming a continuous monolayer. Immunofluorescence images of the tight junctions' markers, zonula occludins-1 (ZO-1) and claudin-19, are shown in **Figure 34 A and 34 B**. It is possible to observe the polygonal shape of differentiated RPE cells and, interestingly, quantification of cell area using each marker revealed a tendency towards higher cellular area in CHM patient cells, with areas of 12.23 μm^2 and 12.74 μm^2 for ZO-1 and 12.74 μm^2 and 13.66 μm^2 for claudin-19 in healthy and patient cells, respectively, **Figure 34 A-D.** These results need to be further confirmed.

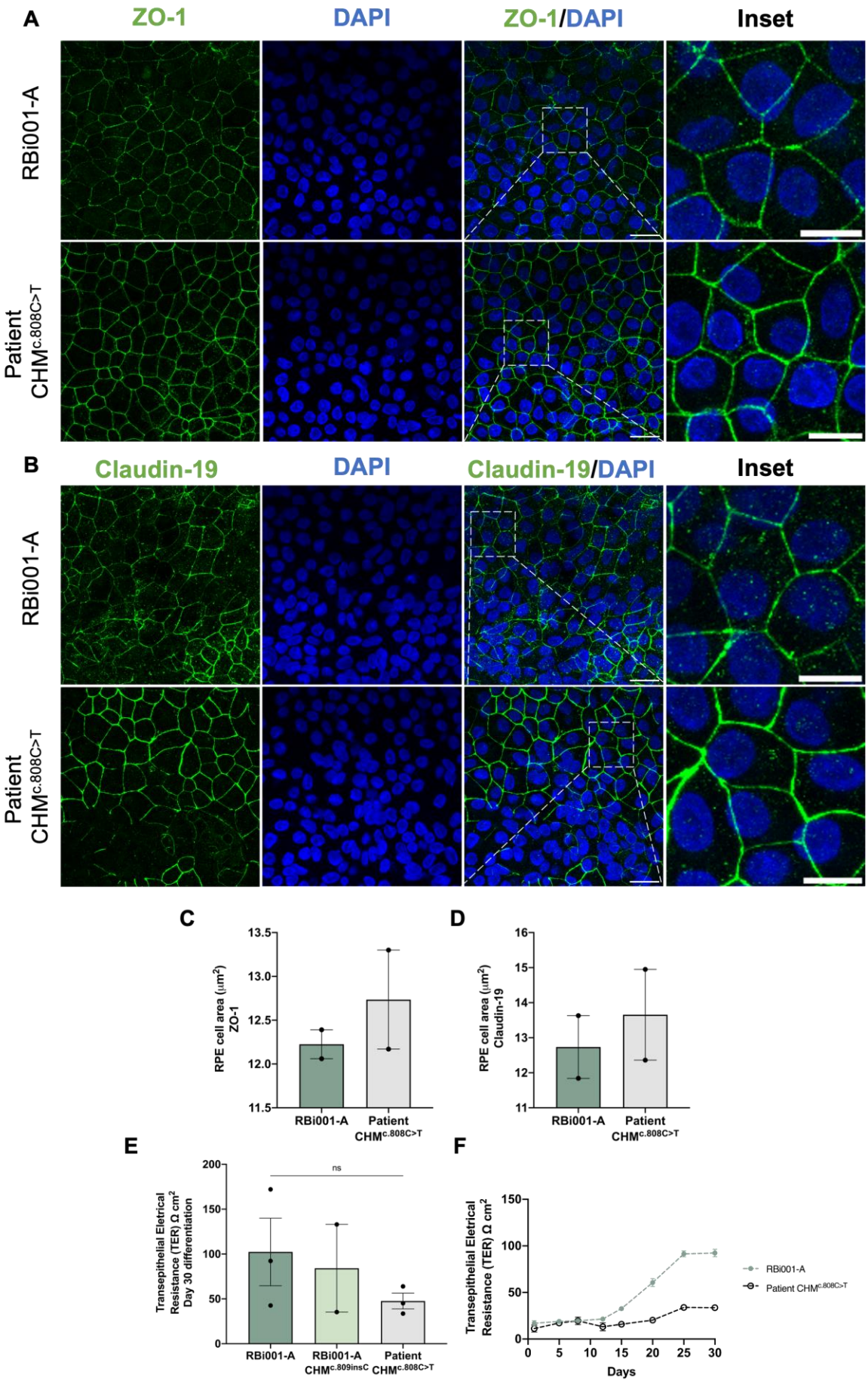

Figure 34. Characterization of differentiated hiPSc-RPE morphology and polarization. A) Immunofluorescence images of tight junctions' marker, zonula occludins-1 (ZO-1), green with nuclei stained

with DAPI (blue). Scale bar 20 μm. Inset Scale bar 10 μm. **B)** Immunofluorescence images of tight junctions' marker, Claudin-19 (green) with nuclei stained with DAPI (blue). Scale bar 20 μm. Inset Scale bar 10 μm. **C)** Quantification of RPE cell area (μm^2) using ZO-1 marker. Data is presented as Mean ± SEM, representative of n=2 independent experiments. **D)** RPE cell area (μm^2) with Claudin-19 marker. Data is presented as Mean ± SEM, representative of n=2 independent experiments. **E)** Trans-epithelial electrical resistance (TER) at day 30 of differentiation. Data is presented as Mean ± SEM, representative of n=3 independent experiments for RBi001-A and Patient CHM$^{c.808C>T}$ and n=2 independent experiments for RBi001-A CHM$^{c.809insC}$. Statistical comparisons were performed using unpaired t-test (ns, not significant). **F)** TER measured every five days of a 30-day differentiation. Data is presented as Mean ± SD, representative of n=1 independent experiments.

One more important aspect of RPE cells is the polarization between the apical and basolateral sides which confer to the RPE a unique role in the transfer of nutrients and waste between the choroidal structure and the layers above. To test the polarization state of RPE cells after differentiation we measured the TER, **Figure 34 E**. The TER after 30 days of differentiation shows higher values of electrical resistance in cells from healthy donor compared to both patient and isogenic mutant cells, **Figure 34 E.** To better understand the difference in TER between control and CHM cells, we measured TER every 5 days during a 30-day differentiation, **Figure 34 F**, and we see a clear difference after day 15, suggesting that the absence of REP1 is having subtle effects on both the morphology and the polarization state of RPE cells.

3.2.2. The early endo-lysosomal pathway in hiPSc-RPE model of CHM

Given the closer similarity of hiPSc-RPE with the human RPE, we decided to test several of the results found in ARPE-19 CHM cells. Starting with the early stages of the endo-lysosomal pathway we measured the number and size of EEA1+ vesicles, **Figure 35 A-C**. Quantification revealed no difference between healthy and patient derived RPE cells in both number and size, as was observed in ARPE-19 cells, however graphs represent two independent experiments and need to be further investigated to reach a significant conclusion. The expression levels of EEA1 are similar to the ones found in ARPE-19 cell model, with no significant differences observed between control and REP1 absent lines, **Figure 35 D and 35 E.**

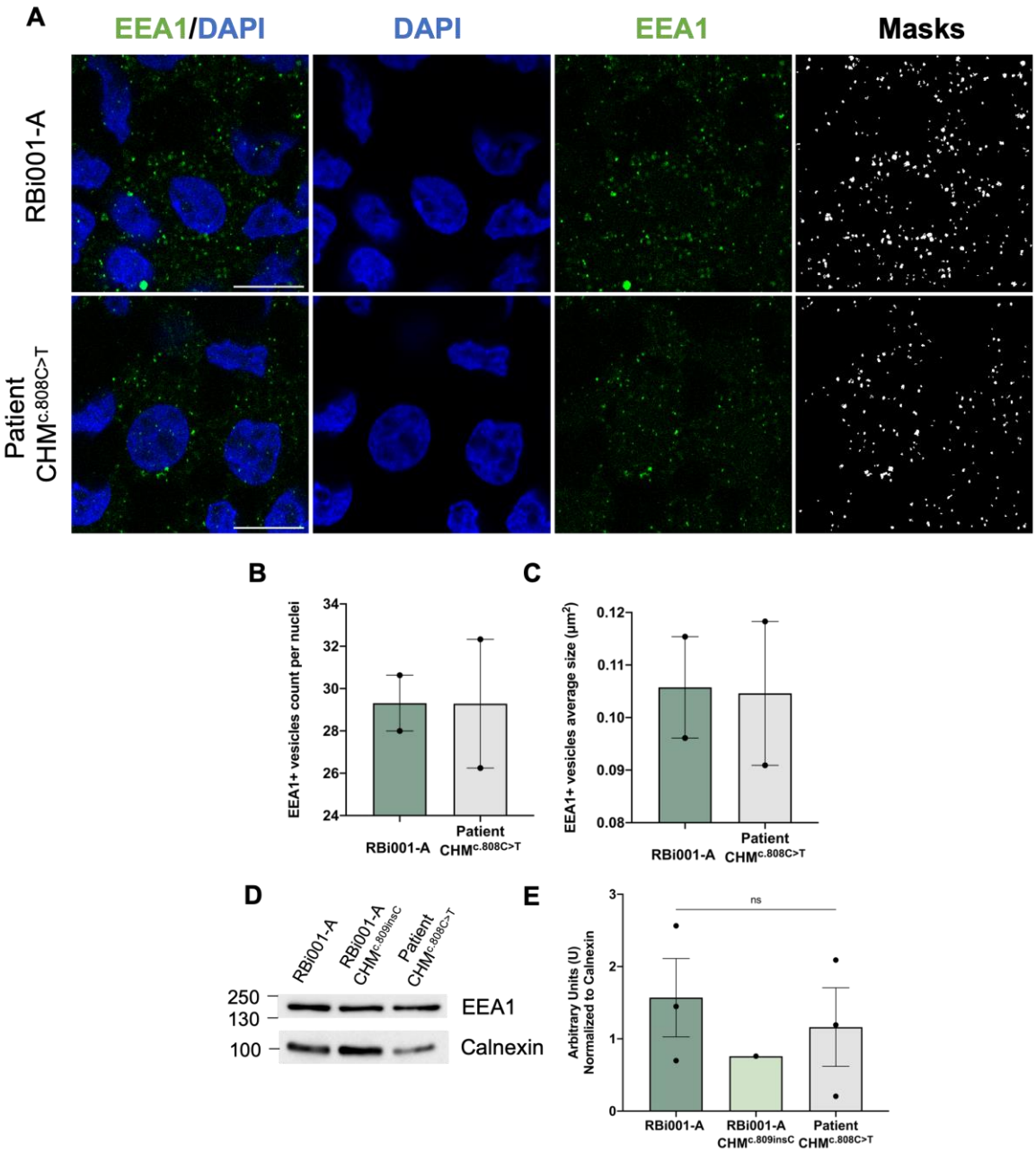

Figure 35. Early stages of the endo-lysosomal pathway in hiPSc-RPE cell model. **A)** Immunofluorescence images of early endosome marker, EEA1 (green), with nuclei stained with DAPI (blue). Scale bar 10 µm. **B)** Quantification of the number of EEA1+ vesicles per nuclei. Data is presented as Mean ± SEM, representative of n=2 independent experiments. **C)** Average size of EEA1+ vesicles (µm^2). Data is presented as Mean ± SEM, representative of n=2 independent experiments. **D)** Western blot analysis of EEA1 expression in whole cell lysates between healthy (RBi001-A) and CHM (RBi001-A CHM$^{c.809insC}$ and Patient CHM$^{c.808C>T}$) cells, representative of n=3 for RBi001-A and Patient CHM$^{c.808C>T}$ and n=1 for RBi001-A CHM$^{c.809insC}$. Loading control: calnexin. **E)** Graphical representation of WB quantification. Normalized to calnexin. Data is presented as Mean ± SEM, representative of n=3 for RBi001-A and Patient CHM$^{c.808C>T}$ and n=1 for Rbi001-A CHM$^{c.809insC}$. Statistical comparisons were performed using unpaired t-test (ns, not significant).

3.2.3. The late endo-lysosomal pathway in hiPSc-RPE model of CHM

To analyse if the phenotype found in ARPE-19, where CHM cells show higher levels of late endosome/lysosome markers, we stained hiPSc-RPE with LAMP1 and LAMP2 antibodies. **Figure 36 A** represents the staining of LAMP1, and quantification reveals an increase in the count of LAMP1+ vesicles in

CHM patient derived cells (p-value: 0.0511), just like the trend observed in ARPE-19 cells, **Figure 36 A and 36 B**. LAMP1+ vesicles size shows no significant difference between cell lines, just a slight tendency towards higher sizes in CHM models, isogenic mutant, and patient derived line, with values of 0.1097 μm^2, 0.1468 μm^2 and 0.1347 μm^2, respectively, **Figure 36 A and 36 C.** The expression levels found by WB, follows the trend observed in ARPE-19 with no significant differences between cell lines, **Figure 36 D and 36 E.**

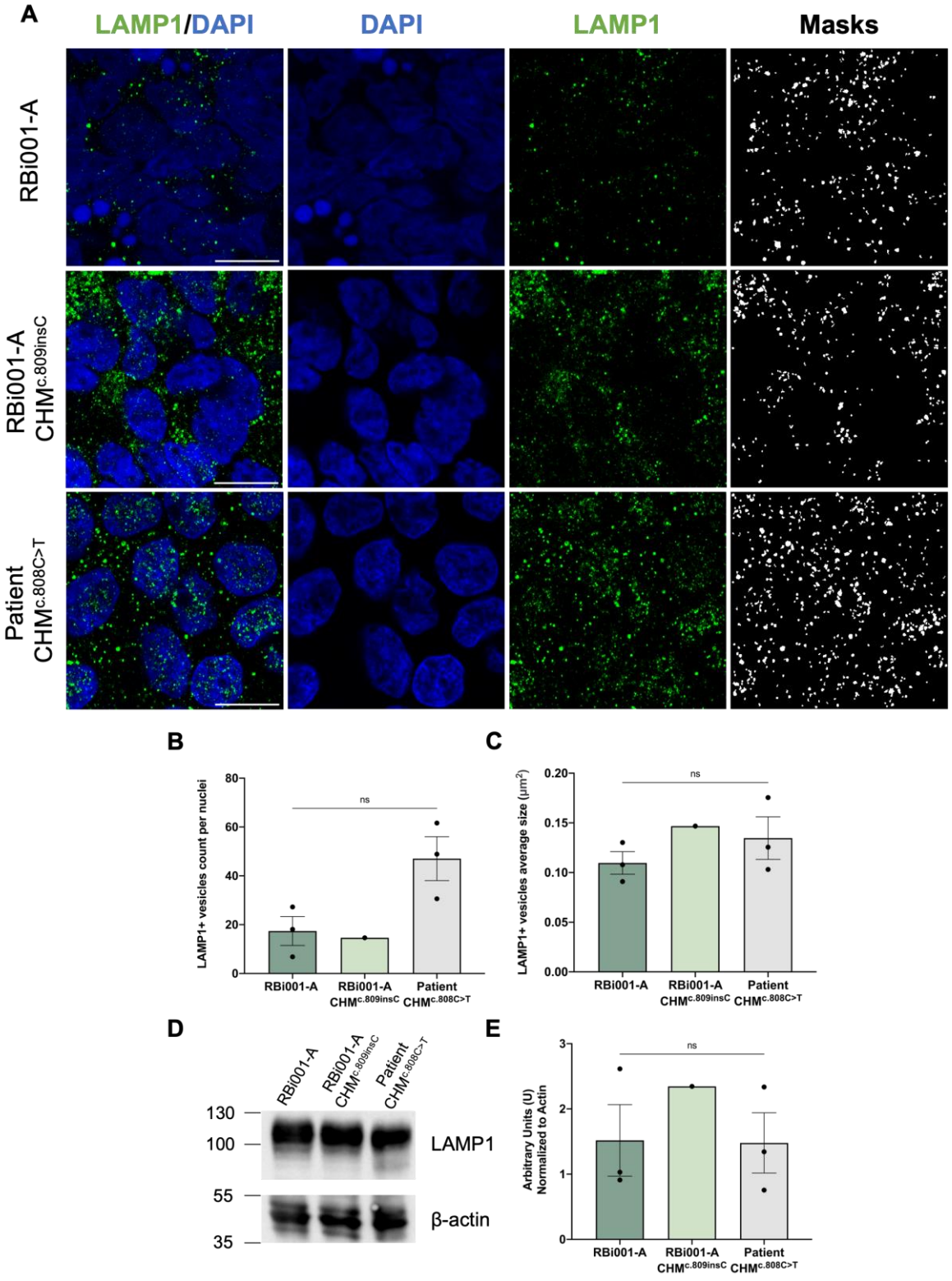

Figure 36. Characterization of LAMP1+ vesicles in hiPSc-RPE cell model of CHM. **A)** Immunofluorescence images of lysosomal marker, LAMP1 (green) with nuclei stained with DAPI (blue). Scale bar 10 μm. **B)**

Quantification of the number of LAMP1+ vesicles per nuclei. Data is presented as Mean ± SEM, representative of n=3 independent experiments for Rbi001-A and Patient CHM$^{c.808C>T}$ and n=1 for Rbi001-A CHM$^{c.809insC}$. Statistical comparisons were performed using unpaired t-test (ns, not significant). **C)** Average size of LAMP1+ vesicles (μm^2). Data is presented as Mean ± SEM, representative of n=3 for Rbi001-A and Patient CHM$^{c.808C>T}$ and n=1 for Rbi001-A CHM$^{c.809insC}$. Statistical comparisons were performed using unpaired t-test (ns, not significant). **D)** Western blot analysis of LAMP1 expression in whole cell lysates between healthy (Rbi001-A) and CHM (Rbi001-A CHM$^{c.809insC}$ and Patient CHM$^{c.808C>T}$) cells, representative of n=3 for Rbi001-A and Patient CHM$^{c.808C>T}$ and n=1 for Rbi001-A CHM$^{c.809insC}$. Loading control: β-actin. **E)** Graphical representation of WB quantification. Normalized to β-actin. Data is presented as Mean ± SEM, representative of n=3 for RBi001-A and Patient CHM$^{c.808C>T}$ and n=1 for RBi001-A CHM$^{c.809insC}$. Statistical comparisons were performed using unpaired t-test (ns, not significant).

The staining of LAMP2, showed a significant increase (p-value: 0.0261) in the number of LAMP2+ vesicles between healthy and patient derived cells, **Figure 37 A and 37 B**. There is also a slight tendency for larger vesicle sizes in mutant models, both isogenic mutant and patient line, compared to healthy cells, with average sizes of 0.2233 μm^2, 0.2145 μm^2 and 0.1417 μm^2, respectively, **Figure 37 A and 37 C**, however no significant differences were found. The expression levels analysed by WB show no difference between cell lines, **Figure 37 D and 37 E.**

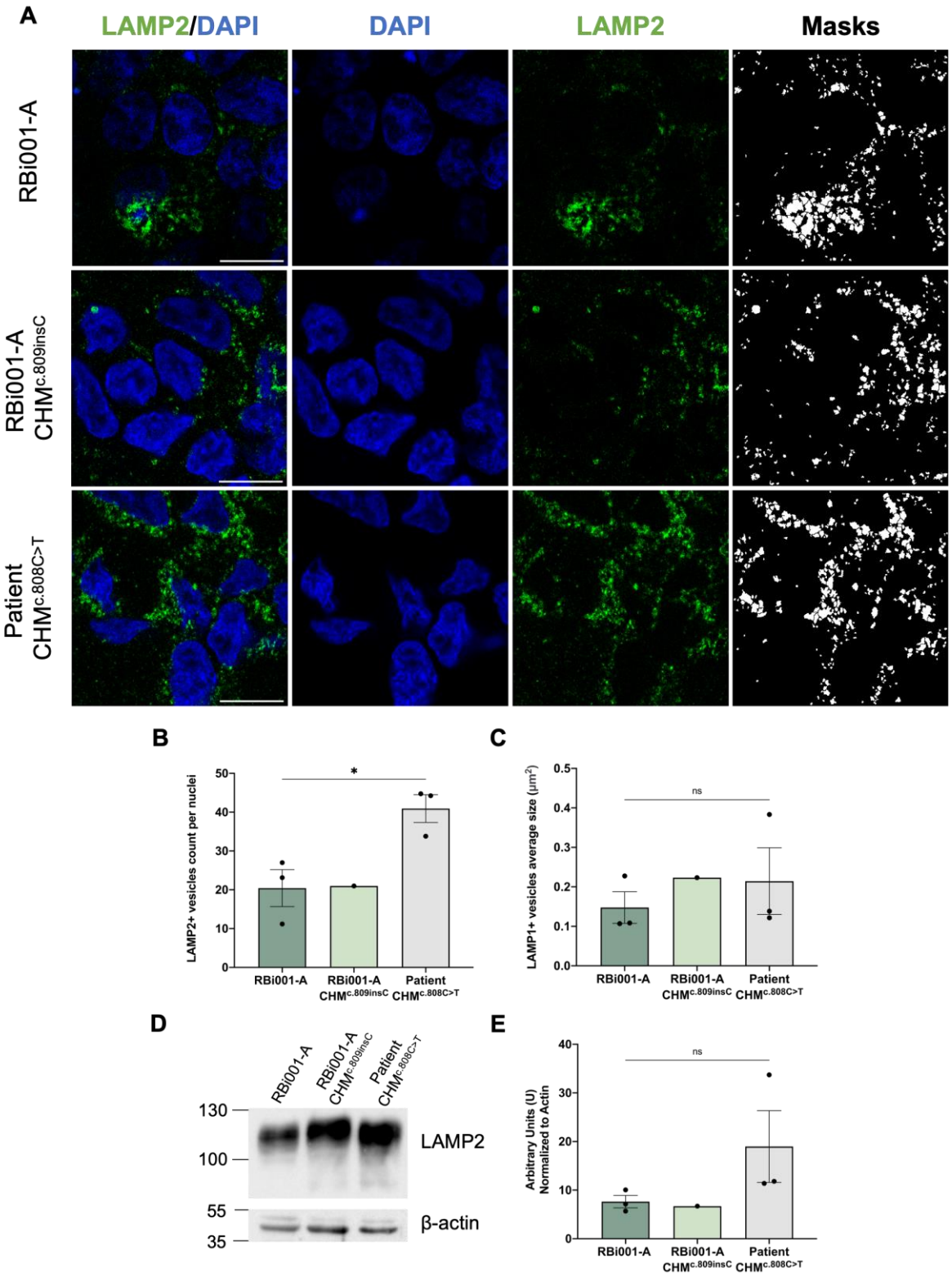

Figure 37. LAMP2+ vesicles are significantly increased in CHM cells in hiPSc-RPE cell model. **A)** Immunofluorescence images of lysosomal marker, LAMP2 (green) with nuclei stained with DAPI (blue). Scale bar 10 µm. **B)** Quantification of the number of LAMP2+ vesicles per nuclei. Data is presented as Mean ± SEM, representative of n=3 independent experiments for RBi001-A and Patient CHM$^{c.808C>T}$ and n=1 for RBi001-A CHM$^{c.809insC}$. Statistical comparisons were performed using unpaired t-test (* P<0.05). **C)** Average size of LAMP2+ vesicles (µm^2). Data is presented as Mean ± SEM, representative of n=3 for RBi001-A and Patient CHM$^{c.808C>T}$ and n=1 for RBi001-A CHM$^{c.809insC}$. Statistical comparisons were performed using nonparametric Mann-Whitney test (ns, not significant). **D)** Western blot analysis of LAMP2 expression in whole cell lysates between healthy (RBi001-A) and CHM (RBi001-A CHM$^{c.809insC}$ and Patient CHM$^{c.808C>T}$) cells, representative of n=3 for RBi001-A and Patient CHM$^{c.808C>T}$ and n=1 for RBi001-A CHM$^{c.809insC}$. Loading control: β-actin. **E)**

Graphical representation of WB quantification. Normalized to β-actin. Data is presented as Mean ± SEM, representative of n=3 for RBi001-A and Patient CHM$^{c.808C>T}$ and n=1 for RBi001-A CHM$^{c.809insC}$. Statistical comparisons were performed using unpaired t-test (ns, not significant).

Moving along the endo-lysosomal pathway we focused on late endosomes/MVBs by analysing CD63 staining and expression levels. The number of CD63+ vesicles reveal an increased tendency towards higher numbers in patient derived RPE cells, however such observation needs further investigation since it only represents two independent experiments, **Figure 38 A and 38 B**. The difference in size, unlike what was found in ARPE-19 where no significant difference was found, seems to show a slight tendency for increased size in CHM patient, however more experiments are needed to make further conclusions, **Figure 38 A and 38 C**. The expression levels of CD63 show no difference between healthy and both patient and isogenic mutant lines, **Figure 38 D and 38 E**.

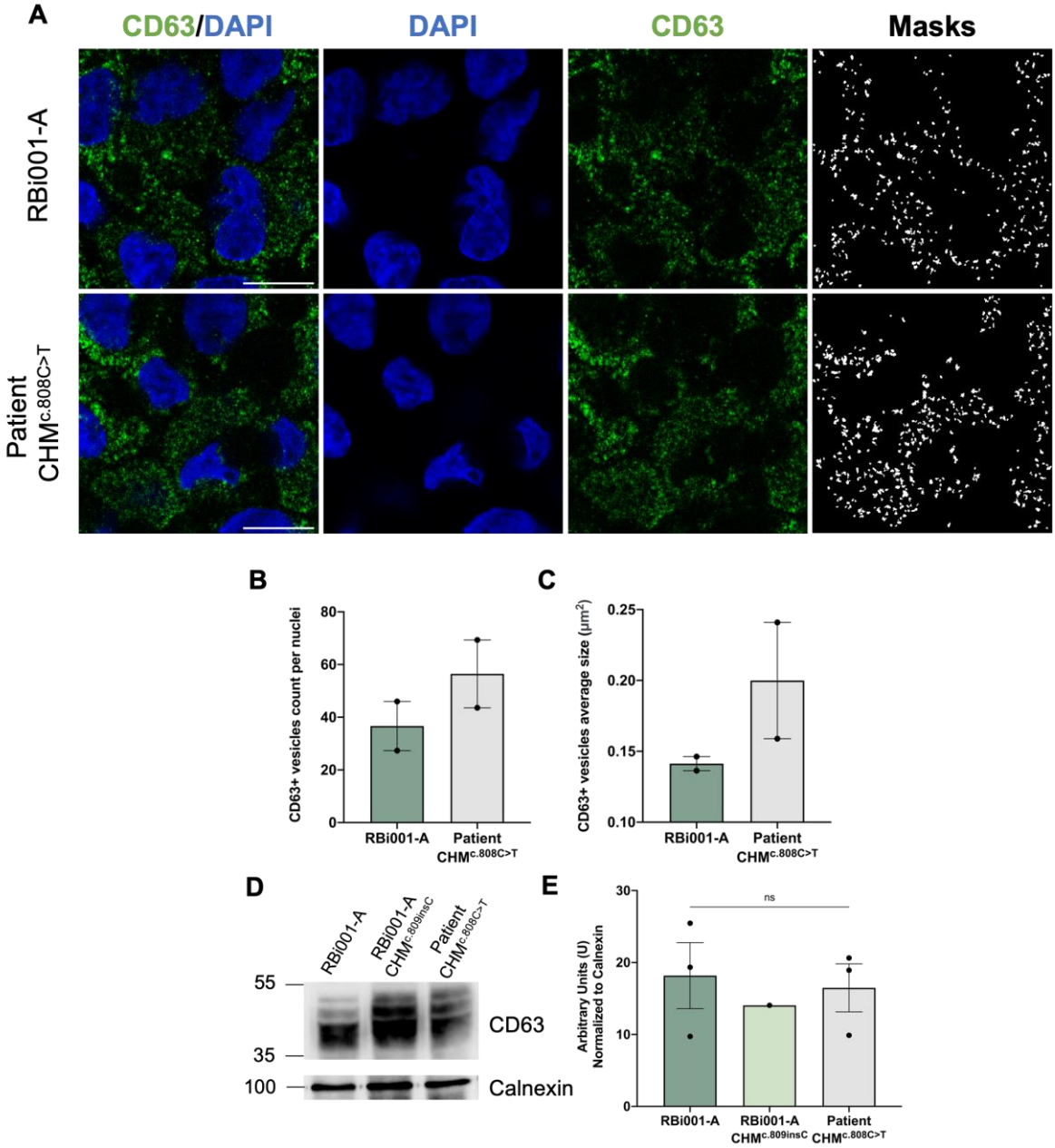

Figure 38. Characterization of late endosomes/MVBs in hiPSc-RPE cell model of CHM. A) Immunofluorescence images of multivesicular bodies (MVBs), CD63 (green) with nuclei stained with DAPI

(blue). Scale bar 10 μm. **B)** Quantification of the number of CD63+ vesicles per nuclei. Data is presented as Mean ± SEM, representative of n=2 independent experiments. **C)** Average size of CD63+ vesicles (μm^2). Data is presented as Mean ± SEM, representative of n=2 independent experiments. **D)** Western blot analysis of CD63 expression in whole cell lysates between healthy (RBi001-A) and CHM (RBi001-A CHM$^{c.809insC}$ and Patient CHM$^{c.808C>T}$) cells, representative of n=3 for RBi001-A and Patient CHM$^{c.808C>T}$ and n=1 for RBi001-A CHM$^{c.809insC}$. Loading control: β-actin. **E)** Graphical representation of WB quantification. Normalized to calnexin. Data is presented as Mean ± SEM, representative of n=3 for RBi001-A and Patient CHM$^{c.808C>T}$ and n=1 for RBi001-A CHM$^{c.809insC}$. Statistical comparisons were performed using unpaired t-test (ns, not significant).

3.2.3.1. Lysosome function and activity

When we attempted to study function and activity or perform phagocytic assays, hiPSc-RPE pose many limitations. Given their high content of pigment containing granules as well as the increased thickness of these cultured cells, the use of live dyes or fixable ones, which successfully work in ARPE-19, was not possible. Furthermore, the 75-day differentiation needed to generate RPE cells, makes it impossible to perform live cell imaging, as the cells are too confluent and don't uptake the dyes as efficiently as ARPE-19 cells. Thus, the confirmation of lysosome activity phenotypes found in ARPE-19 CHM cells was not possible.

Nevertheless, some antibodies could be used successfully in hiPSc-RPE cells, such as for cathepsin D, which revealed no differences between healthy and patient derived cells, in terms of vesicle number, **Figure 39 A and 39 B**. The average size of cathepsin D+ vesicles also did not reveal a significant difference, **Figure 39 A and 39 C**.

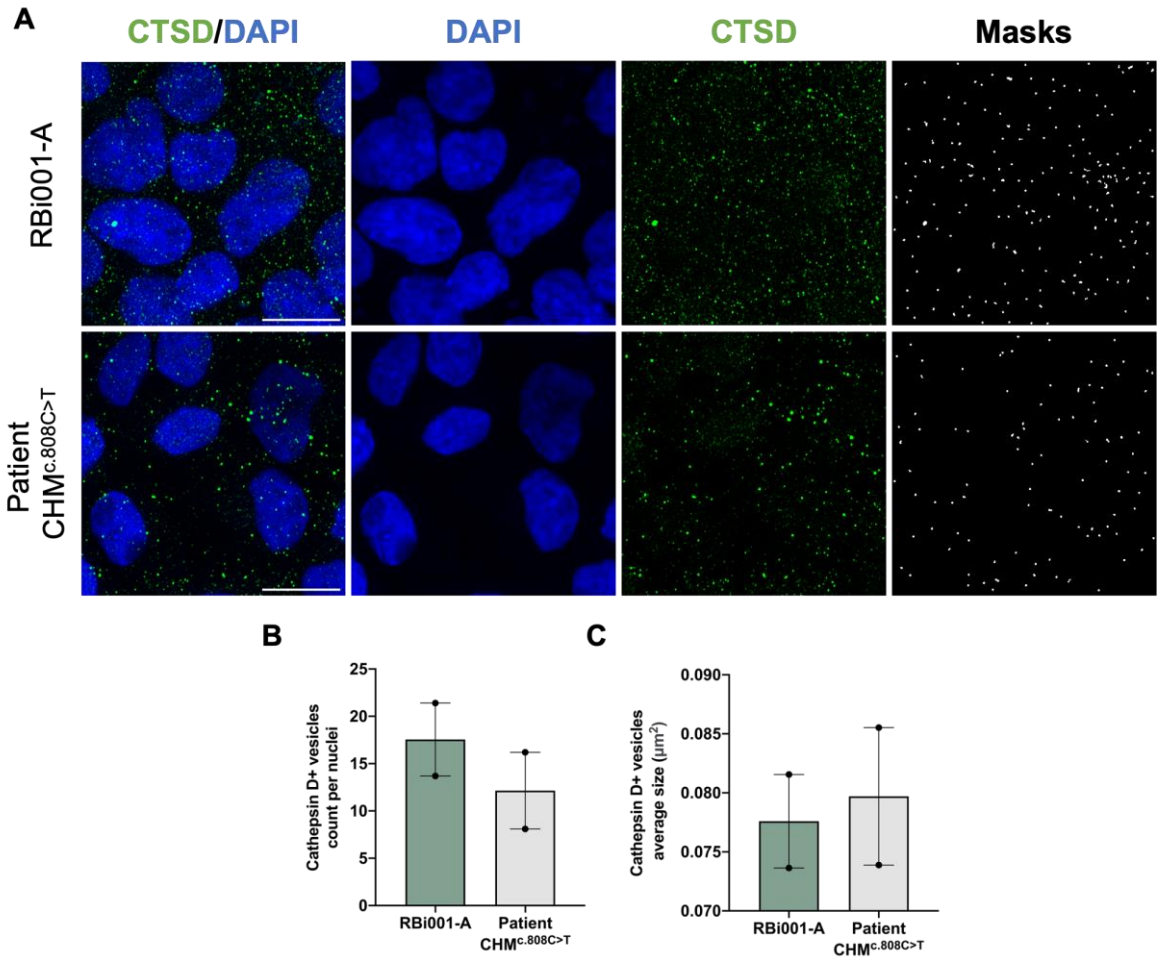

Figure 39. Characterization of lysosomal activity in hiPSc-RPE cell model of CHM. **A)** Immunofluorescence images of cathepsin D marker, CTSD (green) with nuclei stained with DAPI (blue). Scale bar 10 µm. Quantification of **B)** number of CTSD+ vesicles per nuclei. Data is presented as Mean ± SEM, representative of n=2 independent experiments. **C)** average size of CTSD+ vesicles (μm^2). Data is presented as Mean ± SEM, representative of n=2 independent experiments.

The expression levels of different cathepsin isoforms were analysed by WB, **Figure 40**, specifically two different brand antibodies were used for cathepsin D and the ratio between procathepsin and mature cathepsin was quantified, revealing a tendency for higher ratio of procathepsin D/mature levels in patient derived cells, **Figure 40 A-C**, suggesting that procathepsin D accumulates in CHM patient cells indicating a possible deficiency in the maturation of cathepsin D, however confirmation is needed. The analysis of cathepsin L shows a significant increase (p-value: 0.0218) in the ration of Procathepsin L and mature cathepsin L between healthy and patient derived cells, **Figure 40 A and 40 D**, suggesting that in CHM patient cells procathepsin L accumulate and, similar to cathepsin D, there may be a deficiency in the maturation of this protease. In ARPE-19, a slight tendency towards higher levels of procathepsin L was observed, although not significant.

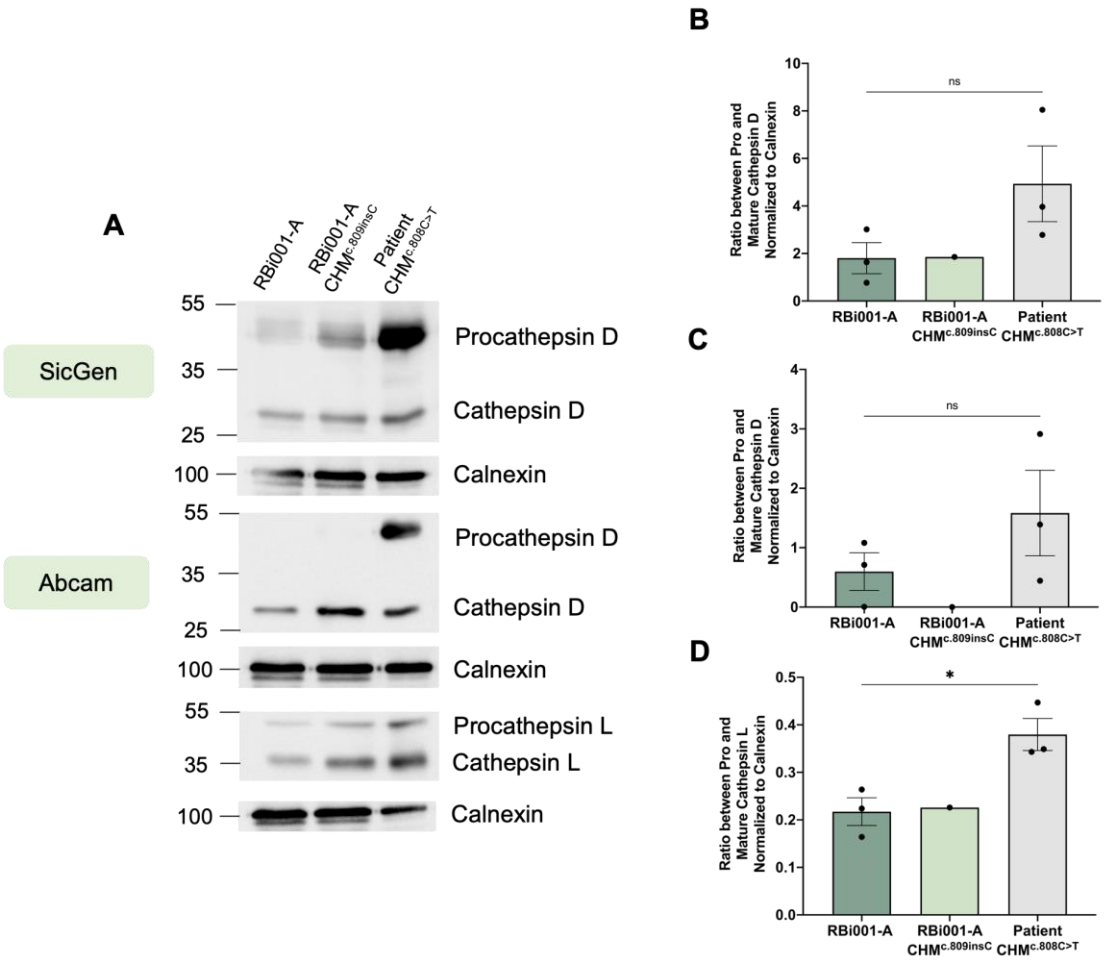

Figure 40. Cathepsins expression levels in hiPSc-RPE cell model of CHM. **A)** Western blot analysis of pro- and matured CTSD (SicGen), CTSD (Abcam) and CTSL expression in whole cell lysates between healthy (RBi001-A) and CHM (RBi001-A CHM$^{c.809insC}$ and Patient CHM$^{c.808C>T}$) cells, representative of n=3 for RBi001-A and Patient CHM$^{c.808C>T}$ and n=1 for RBi001-A CHM$^{c.809insC}$. Loading control: calnexin. **B)** Graphical representation of WB quantification of CTSD (SicGen). Graphs represent the ratio between pro- and matured cathepsin D normalized to calnexin. Data is presented as Mean ± SEM, representative of n=3 for RBi001-A and Patient CHM$^{c.808C>T}$ and n=1 for RBi001-A CHM$^{c.809insC}$. Statistical comparisons were performed using unpaired t-test (ns, not significant). **C)** Graphical representation of WB quantification of CTSD (Abcam). Graphs represent the ratio between pro- and matured cathepsin D normalized to calnexin. Data is presented as Mean ± SEM, representative of n=3 for RBi001-A and Patient CHM$^{c.808C>T}$ and n=1 for RBi001-A CHM$^{c.809insC}$. Statistical comparisons were performed using unpaired t-test (ns, not significant). **D)** Graphical representation of WB quantification of CTSL. Graphs represent the ratio between pro- and matured cathepsin L normalized to calnexin. Data is presented as Mean ± SEM, representative of n=3 for RBi001-A and Patient CHM$^{c.808C>T}$ and n=1 for RBi001-A CHM$^{c.809insC}$. Statistical comparisons were performed using unpaired t-test (* P<0.05).

Chapter 4 – Discussion

Over the years, choroideremia research has been largely focused on the clinical features and as the development of new therapies, with limited interest in the molecular consequences, such as the endo-lysosomal pathway in RPE cells[56,63,64,67]. One of the limitations has been the absence of adequate humanized cell models to study this disease in RPE cells. Evidence has shown that RPE cells absent for REP1 show a reduction in the degradation capacity of POS, a deficiency in phagosome acidification as well as an impairment in the movement of melanin containing granules to the apical side of the cells[65,66]. With this in mind, we intended to do a full characterization of the endo-lysosomal pathway to hopefully uncover new phenotypes to better understand the impact of REP1 loss in RPE cells, as well as to contribute to the current knowledge to potentiate new therapies.

To develop this project, we started by employing a commonly used immortalized cell line, ARPE-19 which allows the analysis of morphological, functional, and phagocytic cellular events with a high yield and efficiency. Additionally, any evidence found in ARPE-19 was also tested in hiPSc differentiated RPE cells which more closely resembles the RPE found in the human retina, however with limitations in the type of assays available when compared to ARPE-19.

One of the most important features of differentiated RPE is the achievement of a polygonal shape, polarization, pigmentation, post-mitotic state, and a phagocytic capacity, all of them verified in our differentiated hiPSc RPE, except for the phagocytic capacity which needs further optimization[111]. However, between control and CHM lines we found slight differences in some of these parameters. Regarding polarization, we measured the TER and found a striking difference between control and CHM lines, suggesting that somehow the absence of REP1 is affecting the ability of RPE to form a tight monolayer, which may be due to defects in the formation and maintenance of tight junctions, previously described in Daniela Oliveira master thesis[111]. In RPE cells derived from healthy donors, TER reached levels of 102.3 Ω cm^2, however levels higher than 250 Ω cm^2 have been described with other differentiation protocols. Moreover, stainings of both ZO-1 and Claudin-19 revealed an increased cellular area in CHM cells, again suggesting subtle defects in the establishment of a tight monolayer, a phenotype that should be further analysed and understood.

Our work uncovered new phenotypes in the endo-lysosomal pathway in two different CHM models. Analysing the early components of this pathway, by evaluating EEA1 staining and expression levels, revealed that in both ARPE-19 and hiPSc-RPE, no difference was found in the number and size of EEA1+ vesicles, as well as expression levels, suggesting that REP1 deficiency does not influence the formation of early endosomes. We found that the number of CD63+ vesicles is significantly increased in both ARPE-19 and hiPSc-RPE CHM models, with no differences verified in the average size of vesicles, as well as CD63 expression levels. Thus, in CHM, higher numbers of CD63+ vesicles in both models may indicate a possible distribution difference of CD63 protein, being present in more vesicles compared to control cells, suggesting that there

are subtle defects in these intermediate compartments, both in terms of numbers and their localization within the cell, due to REP1 deficiency.

The endo-lysosomal pathway begins with the endocytosis of extracellular material into early endosomes, which further mature into late endosomes/MVBs, which in turn can be exocytosed or fuse with lysosomes. We focused this work on the lysosomes, analysing both their morphology as well as their activity. LAMP1 and LAMP2 staining, well known lysosomal membrane markers, revealed an increase in the number of LAMP1+ and LAMP2+ vesicles in both CHM models, with no differences in average vesicle size. In terms of expression, no difference was observed for both proteins between control and CHM cells in both cell models, thus, similar to CD63+ structures, the unchanged expression levels together with the higher numbers of positive vesicles may indicate that there are more lysosomes present per cell and that the distribution of LAMP1 and LAMP2 protein is spread across this increased number of vesicles. However, such finding should be confirmed by new assays that analyse the distribution of vesicles within the cell, some of them already being used for lysosome analysis[123]. Our results suggest that while early endosome number and size is not affected, changes in number are observed in late endosomes/lysosomes, suggesting that the absence of REP1 affects late stages of the endo-lysosomal pathway. To our knowledge, the findings mentioned above, have never been described before in the literature.

Western blot analysis of cathepsin D revealed an increased tendency, however not significant, towards higher expression levels of procathepsin D in hiPSc-PE CHM patient cells. Additionally, WB of cathepsin L reveals a significant increase in procathepsin L in hiPSc-RPE patient cells. In ARPE-19, the analysis of the expression of pro- and matured cathepsin D does not show the same tendency since no significant difference is observed in the ration between pro- and matured cathepsin D in WT and CHM ARPE-19 cells. Since the delivery of cathepsin D to lysosomes is dependent on the endocytic pathway, regulated by Rab7[124], the higher levels of the procathepsin form in hiPSc-RPE CHM models may suggest an impairment in the transport of the protease to lysosomes.

In ARPE-19, the two different antibodies for cathepsin D (R&D and SicGen) revealed a tendency towards higher numbers of cathepsin D+ vesicles, however not significant, with no difference in vesicle size. In hiPSc-RPE, both numbers and size of cathepsin D+ vesicles do not show any differences. However, more independent experiments are needed in both models to reach significant conclusions. The quantification of immunofluorescence images of cells stained for different cathepsin forms presents its challenges due to the inability to distinguish between pro- and matured cathepsin, thus results obtained from expression levels analysis provide more significant conclusions regarding activity of cathepsins in lysosomes.

In this project, we took advantage of a new fixable dye that stains specifically active cathepsin D, in order to complement the findings from western blot analysis that showed a tendency towards higher levels of procathepsin. We found higher numbers of vesicles with active cathepsin D in our CHM ARPE-19 model. Previous studies have shown an impairment in phagosome acidification in CHM cells[64] and since the activity of cathepsin is dependent on an acidic environment it is hard to understand how CHM ARPE-19 cells can

present higher numbers of active cathepsin D containing vesicles. To try and understand this further, we used different dyes, such as LysoTracker, which stains acidic vesicles. LysoTracker staining, showed no difference in the number of positive vesicles. Additionally, we also tested pHRODO Dextran, a live dye that can be used to specifically stain late endosomes/lysosomes, and its fluorescence intensity is directly proportional to the luminal pH. Quantification of these vesicles from three independent experiments, showed no difference in vesicle fluorescence intensity. These results together showed that when looking at the overall cellular compartments, no difference is found regarding vesicle acidity and the same was true when narrowing the search to late endosomes/lysosomes. Thus, the results found regarding cathepsins, specifically the accumulation of procathepsin forms, together with the lack of differences in vesicle acidity, may indicate an impairment in the transport of the procathepsin forms to the lysosomes in order to mature in an acidic environment.

To look further into cathepsins activity we used two different live dyes, magic red cathepsin B and magic red cathepsin D, which only fluoresces when its substrate is cleaved by each specific cathepsin. The number and fluorescence intensity of magic red cathepsin B stained vesicles revealed no difference between control and CHM cells. However, when looking at cathepsin L, the fluorescence intensity shows a slight decrease in CHM compared to control cells, suggesting that in the absence of REP1, vesicles with active cathepsin L have decreased pH. All of these results together suggest that the higher number of active cathepsin D+ vesicles found in ARPE-19 CHM cells may be due to differences in the protein distribution across vesicles and not due to real changes in total cathepsin activity or vesicle pH.

Previous studies using hfRPE showed that a single pulse of POS leads to the appearance of AFGs 24h after POS feeding, with this accumulation being both time and POS-concentration dependent[46]. Our current results, where ARPE-19 cells were POS-fed and AFGs appeared as early as 4 hours later, validate this cell line as a good model to study POS phagocytosis and digestion. Unfortunately, with our current experimental protocol, hiPSc-RPE cells did not produce AFGs after a POS feeding, but further optimisation is required. To test the phagocytic capacity of RPE we challenged ARPE-19 cells with POS isolated from porcine eyes[46,112] and observed at different chase times. ARPE-19 CHM cells fed with POS and chased for 72h, revealed a 6-fold increase in the number of cells positive for undigested POS-containing phagosomes, a striking difference compared to WT cells. Additionally, previous studies[64] of POS phagocytosis in the context of REP1 deficiency, also showed a reduced degradation and accumulation of POS-containing phagosomes, a result we were able to confirm. In that study, POS were labelled with a sensitive rhodamine-based dye that only fluoresces in acidic environments unlike our ARPE-19 cells were POS are fed and natural occurring autofluorescence is tracked along time.

In ARPE-19 cells the formation of AFGs which mimic lipofuscin *in vivo*, is observed as early as 4h, allowing us to quantify these granules and therefore quantify the degree of accumulation when REP1 is absent from RPE cells. Our results, show a significant accumulation of AFGs in CHM cells as early as 4h post feeding, and the same accumulation was observed in later time points. Additionally, the average size of AFGs

at 24h post-feeding is significantly decreased in CHM cells compared to WT and the same tendency is observed at 72h, however not significant. The mechanisms regulating AFGs size remain completely unknown.

In the future, we would like to understand to a greater extent the early steps of the phagocytic pathway, as well as the internalization of POS particles by RPE cells and the consequences of CHM in these events. Previous studies reported no differences in the incorporation/internalisation of POS, only in the degradation of POS-containing phagosomes, thus we wanted to confirm and better understand such results in both our cell models[56,63,64].

We checked for the interaction between late endosomes/lysosomes markers and AFGs at 72h post-feeding since previous works have described a decrease in this interaction in CHM cells. In 2010, Gordiyenko et.al measured the interaction of POS-containing phagosomes with late endosome/lysosome markers, Rab7 and LAMP1 and found a decreased association in REP1 absent cell[64]. In the future, we would like to analyse this further and quantify the level of interaction between different endo-lysosomal markers, such as LAMP1 and CD63, with the AFGs formed in ARPE-19 cells.

The hiPSc-RPE generated in our lab, as previously mentioned, check most parameters to be considered an excellent RPE cell model, with the exception of POS phagocytosis. One of these key features is pigmentation, due to the high content of melanin containing granules, confirmed by the quantification of PMEL fluorescence intensity levels. However, pigmentation poses a huge limitation in immunofluorescence assays, and the difference in immunofluorescence images obtained in hiPSc-RPE cells compared to ARPE-19 is clear, as well as in the changes that immunofluorescence protocol for hiPSc-RPE required for antibodies to penetrate the tight monolayer. For our work, specifically for the POS phagocytosis assays, we encounter many challenges. Given the time-consuming differentiation period, when hiPSc-RPE reached the final differentiation period and were considered matured RPE, the thickness of the cell layer is significant and becomes a challenge for adequate fluorescent imaging. To try and overcome this technical challenge, we added 10% FBS to stimulate phagocytosis, however the observation of clear fluorescent AFGs was still difficult, possibly due to the weak autofluorescent signal being quenched by the dark melanin pigment. In the future, we would want to achieve an optimized protocol to be able to clearly analyse the accumulation of AFGs in hiPSc-RPE cells, just like with ARPE-19.

Given the key role that REP1 protein has on the endo-lysosomal pathway, the characterization of the molecular mechanisms of REP1 deficit in the endo-lysosomal pathway was our main focus. However, since no cell process works independently, we also wanted to check for possible cellular defects in other organelles other than the ones present in the lysosomal pathway. To do so, we chose to focus on the mitochondrial network given its crucial role in maintaining cellular energy homeostasis. Additionally, evidence shows that in a mitochondria dysfunction disease, Kearns-Sayre syndrome, retinal degeneration is found at a degree also seen in late stages of CHM. Our results show that in ARPE-19, the total area occupied by the mitochondrial network is slightly increased in CHM cells, however no relevant difference in the expression levels of TOM20 was observed. The absence of REP1 is RPE cells seems to lead to a general change in distribution of cell

contents compared to WT cells. We verified this idea with late endosome/lysosome markers, such as LAMP1, LAMP2 and CD63, which appear in a higher number of vesicles yet show with no changes in total protein expression, suggesting a possible defect in cellular targeting of some of these proteins. A recent review describes protocols to analyse vesicle/organelle positioning relative to nuclei and plasma membrane using automatic methods[123], thus in the future we want to employ some of these methods and further explore new possible phenotypes of REP1 absence in CHM cells. Additionally, other organelles such as the ER and the Golgi apparatus should also be analysed.

With this work we provided new evidence regarding different cellular phenotypes of members belonging to the endo-lysosomal pathway, POS incorporation and degradation, as well as morphological differences in newly generated RPE from hiPSc and polarization defects, represented in **Figure 41.** We also show key differences between two cellular models of RPE, detailing advantages and disadvantages of each model in different assays and technical approaches. We strived to achieve optimized protocols for hiPSc-RPE to overcome technical challenges and make hiPSc-RPE an even better model of RPE to investigate the molecular and cellular mechanisms of choroideremia.

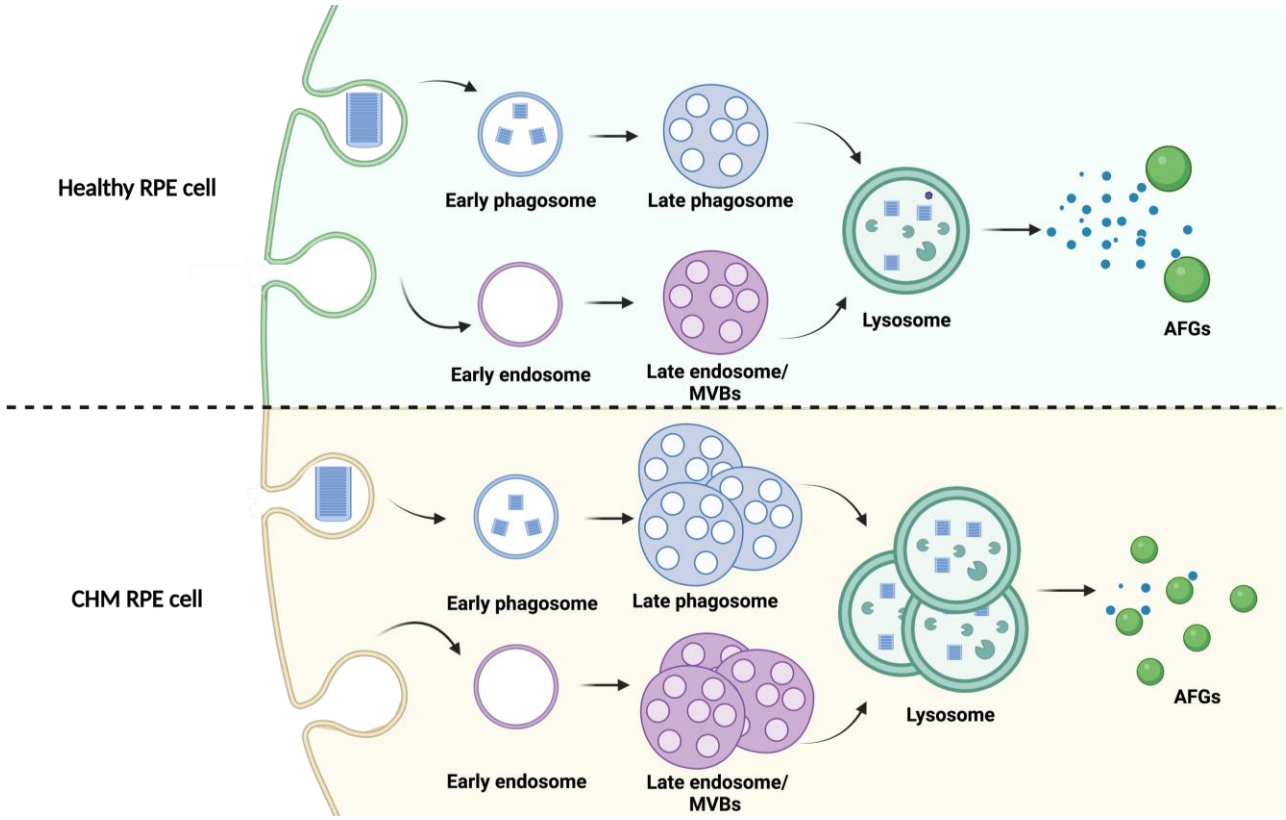

Figure 41. Novel phenotypes of the endo-lysosomal pathway in CHM cells. Early compartments, such as early endosomes and phagosomes showed no difference in both number and size, analysed by EEA1. Late endosomes/MVBs and late phagosomes revealed a significant increase in the number of vesicles with no difference in their size in CHM cells, analysed using CD63. The number of lysosomes significant increase in CHM, as verified with LAMP1 and LAMP2, while no difference in vesicle size was observed. Autofluorescent granules (AFGs) resulting from an incomplete digestion significantly accumulate after POS feeding in CHM cells with a significant decrease in size.

References

1. MacLaren, R. E. *et al.* Retinal gene therapy in patients with choroideremia: Initial fi ndings from a phase 1/2 clinical trial. *Lancet* **383**, 1129–1137 (2014).
2. Lakkaraju, A. *et al.* The cell biology of the retinal pigment epithelium. *Progress in Retinal and Eye Research* vol. 78 100846 (2020).
3. Seabra, M. C., Mules, E. H. & Hume, A. N. Rab GTPases, intracellular traffic and disease. *Trends Mol. Med.* **8**, 23–30 (2002).
4. Pereira-Leal, J. B., Strom, M., Godfrey, R. F. & Seabra, M. C. Structural determinants of Rab and Rab Escort Protein interaction: Rab family motifs define a conserved binding surface. *Biochem. Biophys. Res. Commun.* **301**, 92–97 (2003).
5. Klumperman, J. & Raposo, G. The complex ultrastructure of the endolysosomal system. *Cold Spring Harb. Perspect. Biol.* **6**, (2014).
6. Hu, Y. B., Dammer, E. B., Ren, R. J. & Wang, G. The endosomal-lysosomal system: From acidification and cargo sorting to neurodegeneration. *Transl. Neurodegener.* **4**, 1–10 (2015).
7. E, K., AJ, L., DA, T. & JA, R. Impaired Cargo Clearance in the Retinal Pigment Epithelium (RPE) Underlies Irreversible Blinding Diseases. *Cells* **7**, 16 (2018).
8. Homma, Y., Hiragi, S. & Fukuda, M. Rab family of small GTPases: an updated view on their regulation and functions. *FEBS J.* **288**, 36–55 (2021).
9. Ali, B. R. & Seabra, M. C. Targeting of Rab GTPases to cellular membranes. *Biochem. Soc. Trans.* **33**, 652–656 (2005).
10. Corbeel, L. & Freson, K. Rab proteins and Rab-associated proteins: major actors in the mechanism of protein-trafficking disorders. doi:10.1007/s00431-008-0740-z.
11. Pereira-Leal, J. B., Hume, A. N. & Seabra, M. C. *Prenylation of Rab GTPases: molecular mechanisms and involvement in genetic disease*.
12. Scott, C. C., Vacca, F. & Gruenberg, J. Endosome maturation, transport and functions. *Semin. Cell Dev. Biol.* **31**, 2–10 (2014).
13. Leung, K. F., Baron, R. & Seabra, M. C. thematic review Thematic review series: Lipid Posttranslational Modifications Geranylgeranylation of Rab GTPases. *J. Lipid Res.* **47**, 467–475 (2006).
14. Bahadoran, P. *et al.* Rab27a: A Key to Melanosome Transport in Human Melanocytes. *J. Cell Biol.* **152**, 843–849 (2001).
15. M, P. & C, A. Rab escort protein 1 (REP1) in intracellular traffic: a functional and pathophysiological overview. *Ophthalmic Genet.* **25**, 101–110 (2004).
16. Elkin, R.S, Lakoduk, M.A, Schmid L.S. Endocytic pathways and endosomal trafficking: a primer. Springer. 2016. 166:196-204
17. ROTH, T. F. & PORTER, K. R. YOLK PROTEIN UPTAKE IN THE OOCYTE OF THE MOSQUITO AEDES AEGYPTI. L. *J. Cell Biol.* **20**, 313 (1964).

18. Mayor, S. & Pagano, R. E. Pathways of clathrin-independent endocytosis. *Nat. Rev. Mol. Cell Biol. 2007 88* **8**, 603–612 (2007).
19. Kerr, M. C. & Teasdale, R. D. Defining Macropinocytosis. *Authors J. Compil. #* **10**, 364–371 (2009).
20. Kishore, U. *et al.* Phagocytosis: Our Current Understanding of a Universal Biological Process. *Front. Immunol. | www.frontiersin.org* **1**, 1066 (2020).
21. Kamentseva, R. *et al.* Functional cycle of EEA1-positive early endosome: Direct evidence for pre-existing compartment of degradative pathway. (2020) doi:10.1371/journal.pone.0232532.
22. Yuan, W. & Song, C. The Emerging Role of Rab5 in Membrane Receptor Trafficking and Signaling Pathways. (2020) doi:10.1155/2020/4186308.
23. Huotari, J. & Helenius, A. Endosome maturation. *EMBO J.* **30**, 3481–3500 (2011).
24. Russell, M. R. G., Nickerson, D. P. & Odorizzi, G. Molecular mechanisms of late endosome morphology, identity and sorting. *Curr. Opin. Cell Biol.* **18**, 422–428 (2006).
25. Rink, J., Ghigo, E., Kalaidzidis, Y. & Zerial, M. Rab conversion as a mechanism of progression from early to late endosomes. *Cell* **122**, 735–749 (2005).
26. Luzio, J. P., Pryor, P. R. & Bright, N. A. Lysosomes: fusion and function. *Nat. Rev. Mol. Cell Biol. 2007 88* **8**, 622–632 (2007).
27. DE DUVE, C., PRESSMAN, B. C., GIANETTO, R., WATTIAUX, R. & APPELMANS, F. Tissue fractionation studies. 6. Intracellular distribution patterns of enzymes in rat-liver tissue. *Biochem. J.* **60**, 604 (1955).
28. Saftig, P. & Klumperman, J. Lysosome biogenesis and lysosomal membrane proteins: trafficking meets function. (2009) doi:10.1038/nrm2745.
29. A, B. & JS, B. Lysosomes as dynamic regulators of cell and organismal homeostasis. *Nat. Rev. Mol. Cell Biol.* **21**, 101–118 (2020).
30. Ageing and health. https://www.who.int/news-room/fact-sheets/detail/ageing-and-health.
31. Lamming, D. W. & Liron Bar-Peled, |. Lysosome: The metabolic signaling hub. (2018) doi:10.1111/tra.12617.
32. Platt, F. M., Boland, B. & van der Spoel, A. C. The cell biology of disease: Lysosomal storage disorders: The cellular impact of lysosomal dysfunction. *J. Cell Biol.* **199**, 723 (2012).
33. Yang, S., Zhou, J. & Li, D. Functions and Diseases of the Retinal Pigment Epithelium. doi:10.3389/fphar.2021.727870.
34. Kwon, W. & Freeman, S. A. Phagocytosis by the Retinal Pigment Epithelium: Recognition, Resolution, Recycling. *Front. Immunol.* **11**, 2985 (2020).
35. Caceres, P. S. & Rodriguez-Boulan, E. Retinal Pigment Epithelium Polarity in Health and Blinding Diseases. doi:10.1016/j.ceb.2019.08.001.
36. Hartong, D. T., Berson, E. L. & Dryja, T. P. Retinitis pigmentosa. *Lancet* **368**, 1795–1809 (2006).
37. Jager, R. D., Mieler, W. F. & Miller, J. W. Age-Related Macular Degeneration. *https://doi.org/10.1056/NEJMra0801537* **358**, 2606–2617 (2008).

38. Busskamp, V. *et al.* Rebuilding the Missing Part-A Review on Photoreceptor Transplantation. **10**, 105 (2017).
39. den Hollander, A. I., Roepman, R., Koenekoop, R. K. & Cremers, F. P. M. Leber congenital amaurosis: genes, proteins and disease mechanisms. *Prog. Retin. Eye Res.* **27**, 391–419 (2008).
40. Lamb, T. D. Why rods and cones? *Eye* **30**, 179–185 (2016).
41. Strauss, O. The Retinal Pigment Epithelium in Visual Function. (2005) doi:10.1152/physrev.00021.2004.-Located.
42. Choi, E. H., Daruwalla, A., Suh, S., Leinonen, H. & Palczewski, K. Retinoids in the visual cycle: Role of the retinal G protein-coupled receptor. *J. Lipid Res.* **62**, (2021).
43. Wright, A. F., Chakarova, C. F., Abd El-Aziz, M. M. & Bhattacharya, S. S. Photoreceptor degeneration: genetic and mechanistic dissection of a complex trait. (2010) doi:10.1038/nrg2717.
44. Kiser, P. D., Golczak, M. & Palczewski, K. Chemistry of the Retinoid (Visual) Cycle. (2013) doi:10.1021/cr400107q.
45. Mazzoni, F., Safa, H. & Finnemann, S. C. Understanding photoreceptor outer segment phagocytosis: Use and utility of RPE cells in culture. *Exp Eye Res* **0**, 51–60 (2014).
46. Escrevente, C. *et al.* Formation of Lipofuscin-Like Autofluorescent Granules in the Retinal Pigment Epithelium Requires Lysosome Dysfunction. (2021) doi:10.1167/iovs.62.9.39.
47. Moreno-García, A., Kun, A., Calero, O., Medina, M. & Calero, M. An overview of the role of lipofuscin in age-related neurodegeneration. *Frontiers in Neuroscience* vol. 12 (2018).
48. Boulton, M. E. Studying melanin and lipofuscin in RPE cell culture models. *Exp. Eye Res.* **126**, 61–67 (2014).
49. Katz, M. L. & Robison, W. G. What is lipofuscin? Defining characteristics and differentiation from other autofluorescent lysosomal storage bodies. *Arch. Gerontol. Geriatr.* **34**, 169–184 (2002).
50. Terman, A. & Brunk, U. T. Lipofuscin. *Int. J. Biochem. Cell Biol.* **36**, 1400–1404 (2004).
51. Adler, L. *et al.* The 11-cis Retinal Origins of Lipofuscin in the Retina. *Prog. Mol. Biol. Transl. Sci.* **134**, e1–e12 (2015).
52. Coussa, R. G. & Traboulsi, E. I. Choroideremia: A review of general findings and pathogenesis. *http://dx.doi.org/10.3109/13816810.2011.620056* **33**, 57–65 (2012).
53. Sanchez-Alcudia, R. *et al.* A Comprehensive Analysis of Choroideremia: From Genetic Characterization to Clinical Practice. *PLoS One* **11**, 151943 (2016).
54. De Silva, S. R. *et al.* The X-linked retinopathies: Physiological insights, pathogenic mechanisms, phenotypic features and novel therapies. *Prog. Retin. Eye Res.* **82**, 100898 (2021).
55. Moosajee, M., Ramsden, S. C., Black, G. C., Seabra, M. C. & Webster, A. R. Clinical utility gene card for: Choroideremia. *Eur. J. Hum. Genet.* 22 (2014) doi:10.1038/ejhg.2013.183.
56. A, M., AM, D. & M, M. Choroideremia: from genetic and clinical phenotyping to gene therapy and future treatments. *Ther. Adv. Ophthalmol.* **10**, 251584141881749 (2018).

57. Barnard, A. R., Groppe, M. & Maclaren, R. E. Gene Therapy for Choroideremia Using an Adeno-Associated Viral (AAV) Vector. doi:10.1101/cshperspect.a017293.

58. PENNESI, M. E., BIRCH, D. G., DUNCAN, J. L., BENNETT, J. & GIRACH, A. CHOROIDEREMIA: Retinal Degeneration With an Unmet Need. *Retina* **39**, 2059 (2019).

59. Brambati, M., Borrelli, E., Sacconi, R., Bandello, F. & Querques, G. Choroideremia: Update On Clinical Features And Emerging Treatments. (2019) doi:10.2147/OPTH.S195564.

60. MS, Z. & RE, M. Recent advances and future prospects in choroideremia. *Clin. Ophthalmol.* **9**, 2195–2200 (2015).

61. Alexandrov, K., Horiuchi, H., Steele-Mortimer, O., Seabra, M. C. & Zerial, M. Rab escort protein-1 is a multifunctional protein that accompanies newly prenylated rab proteins to their target membranes. *EMBO J.* **13**, 5262–5273 (1994).

62. Köhnke, M., Delon, C., Hastie, M. L., Nguyen, U. T. T. & Wu, Y.-W. Rab GTPase Prenylation Hierarchy and Its Potential Role in Choroideremia Disease. *PLoS One* **8**, 81758 (2013).

63. NV, S. *et al.* Loss-of-function mutations in Rab escort protein 1 (REP-1) affect intracellular transport in fibroblasts and monocytes of choroideremia patients. *PLoS One* **4**, (2009).

64. Gordiyenko, N. V., Fariss, R. N., Zhi, C. & MacDonald, I. M. Silencing of the CHM gene alters phagocytic and secretory pathways in the retinal pigment epithelium. *Investig. Ophthalmol. Vis. Sci.* **51**, 1143–1150 (2010).

65. Futter, C. E., Ramalho, J. S., Jaissle, G. B., Seeliger, M. W. & Seabra, M. C. The role of Rab27a in the regulation of melanosome distribution within retinal pigment epithelial cells. *Mol. Biol. Cell* **15**, 2264–2275 (2004).

66. Hume, A. N. *et al.* Rab27a Regulates the Peripheral Distribution of Melanosomes in Melanocytes 7. *J. Cell Biol.* **152**, 795–808 (2001).

67. ST, W.-S., T, T., M, L. da S., CE, F. & MC, S. Conditional ablation of the choroideremia gene causes age-related changes in mouse retinal pigment epithelium. *PLoS One* **8**, (2013).

68. Seabra, M. C. New insights into the pathogenesis of choroideremia: a tale of two REPs. *https://doi.org/10.3109/13816819609057869* **17**, 43–46 (2009).

69. Research - CureCHM. https://www.curechm.org/research/#_evolving.

70. Kapetanovic, J. C., Barnard, A. R. & Maclaren, R. E. Molecular Therapies for Choroideremia. (2019) doi:10.3390/genes10100738.

71. Torriano, S. *et al.* The effect of PTC124 on choroideremia fibroblasts and iPSC-derived RPE raises considerations for therapy. *Sci. Rep.* **8**, 8234 (2018).

72. Stem Cell Therapy & Clinical Trials to treat Vision Loss - Fighting Blindness Canada (FBC). https://www.fightingblindness.ca/resources/stem-cell-therapy-for-vision-loss/.

73. Reinhard, J. *et al.* Optogenetic Gene Therapy for the Degenerate Retina: Recent Advances. (2020) doi:10.3389/fnins.2020.570909.

74. Schnichels, S. *et al.* Retina in a dish: Cell cultures, retinal explants and animal models for common diseases of the retina. *Prog. Retin. Eye Res.* **81**, 100880 (2021).

75. Van Cruchten, S. *et al.* Pre- and Postnatal Development of the Eye: A Species Comparison. *Birth Defects Res.* **109**, 1540–1567 (2017).

76. Sanchez, I., Martin, R., Ussa, F. & Fernandez-Bueno, I. The parameters of the porcine eyeball. doi:10.1007/s00417-011-1617-9.

77. Wiencke, A. K. *et al.* Growth of cultured porcine retinal pigment epithelial cells. *Acta Ophthalmol. Scand.* **81**, 170–176 (2003).

78. Klettner, A. & Miura, Y. Porcine RPE/Choroidal Explant Cultures. *Methods Mol. Biol.* **1834**, 109–118 (2019).

79. Miura, Y., Klettner, A., Noelle, B., Hasselbach, H. & Roider, J. Change of Morphological and Functional Characteristics of Retinal Pigment Epithelium Cells during Cultivation of Retinal Pigment Epithelium-Choroid Perfusion Tissue Culture. *Ophthalmic Res.* **43**, 122–133 (2010).

80. Verra, D. M., Sajdak, B. S., Merriman, D. K. & Hicks, D. Diurnal rodents as pertinent animal models of human retinal physiology and pathology. *Prog. Retin. Eye Res.* **74**, (2020).

81. Medicine, M., Aaron Ericsson, by C., Crim, M. J., Franklin, C. L. & Ericsson, A. C. A Brief History of Animal Modeling. *Mo. Med.* **110**, 201 (2013).

82. Hickman, D. L., Johnson, J., Vemulapalli, T. H., Crisler, J. R. & Shepherd, R. Commonly Used Animal Models. *Princ. Anim. Res. Grad. Undergrad. Students* 117 (2017) doi:10.1016/B978-0-12-802151-4.00007-4.

83. Van Den Hurk, J. A. J. M. *et al. Mouse choroideremia gene mutation causes photoreceptor cell degeneration and is not transmitted through the female germline*. *Human Molecular Genetics* vol. 6 (1997).

84. Krock, B. L., Bilotta, J. & Perkins, B. D. Noncell-autonomous photoreceptor degeneration in a zebrafish model of choroideremia. (2007).

85. Tolmachova, T. *et al.* Retinal Pigment Epithelium Defects Accelerate Photoreceptor Degeneration in Cell Type-Specific Knockout Mouse Models of Choroideremia. doi:10.1167/iovs.09-4892.

86. The Mouse Model: Less than Perfect, Still Invaluable. https://www.hopkinsmedicine.org/institute_basic_biomedical_sciences/news_events/articles_and_stories/model_organisms/201010_mouse_model.html.

87. Dunn, K. C., Aotaki-Keen, A. E., Putkey, F. R. & Hjelmeland, L. M. ARPE-19, a human retinal pigment epithelial cell line with differentiated properties. *Exp. Eye Res.* **62**, 155–170 (1996).

88. Klettner, A. K. Retinal Pigment Epithelium Cell Culture. *Retin. Pigment Ep. Heal. Dis.* 295–305 (2020) doi:10.1007/978-3-030-28384-1_17.

89. Tan, E. *et al.* Expression of cone-photoreceptor-specific antigens in a cell line derived from retinal tumors in transgenic mice. *Invest. Ophthalmol. Vis. Sci.* **45**, 764–768 (2004).

90. Krishnamoorthy, R. R. *et al.* Characterization of a transformed rat retinal ganglion cell line. *Brain Res. Mol. Brain Res.* **86**, 1–12 (2001).

91. Clark, A., Tamm, E. R., Al-Ubaidi, M. R. & Hollyfield, J. G. On the use of immortalized ocular cell lines in vision research: the unfortunate story of RGC-5. *Exp. Eye Res.* **116**, 433 (2013).

92. Chu, V. *et al.* In Vitro Characterization of a Spontaneously. *Thromb. Res.* **99**, 71–82 (2000).

93. Grisanti, S. & Guidry, C. Transdifferentiation of retinal pigment epithelial cells from epithelial to mesenchymal phenotype. *Investig. Ophthalmol. Vis. Sci.* **36**, 391–405 (1995).

94. Kuriyama, F., Ueda, Y. & Araki, M. Complete reconstruction of the retinal laminar structure from a cultured retinal pigment epithelium is triggered by altered tissue interaction and promoted by overlaid extracellular matrices. *Dev. Neurobiol.* **69**, 950–958 (2009).

95. Tamiya, S., Liu, L. H. & Kaplan, H. J. Epithelial-mesenchymal transition and proliferation of retinal pigment epithelial cells initiated upon loss of cell-cell contact. *Invest. Ophthalmol. Vis. Sci.* **51**, 2755–2763 (2010).

96. Flood, M. T., Gouras, P. & Kjeldbye, H. Growth characteristics and ultrastructure of RPE in vitro. *Invest. Ophthalmol. Vis. Sci.* **19**, 1309–1320 (1980).

97. Gonzalez-Cordero, A. *et al.* Assessment of AAV Vector Tropisms for Mouse and Human Pluripotent Stem Cell-Derived RPE and Photoreceptor Cells. *Hum. Gene Ther.* **29**, 1124–1139 (2018).

98. Achberger, K., Haderspeck, J. C., Kleger, A. & Liebau, S. Stem cell-based retina models. *Adv. Drug Deliv. Rev.* **140**, 33–50 (2019).

99. Dalvi, S., Galloway, C. A. & Singh, R. Pluripotent Stem Cells to Model Degenerative Retinal Diseases: The RPE Perspective. *Adv. Exp. Med. Biol.* **1186**, 1–31 (2019).

100. Zhu, J. *et al.* Generation of Transplantable Retinal Photoreceptors from a Current Good Manufacturing Practice-Manufactured Human Induced Pluripotent Stem Cell Line. *Stem Cells Transl. Med.* **7**, 210–219 (2018).

101. Skottman, H., Narkilahti, S. & Hovatta, O. Challenges and approaches to the culture of pluripotent human embryonic stem cells. *Regen. Med.* **2**, 265–273 (2007).

102. Brandl, C., Grassmann, F., Riolfi, J. & Weber, B. H. F. Tapping Stem Cells to Target AMD: Challenges and Prospects. *J. Clin. Med.* **4**, 282 (2015).

103. Kiamehr, M. *et al.* Compromised Barrier Function in Human Induced Pluripotent Stem-Cell-Derived Retinal Pigment Epithelial Cells from Type 2 Diabetic Patients. *Int. J. Mol. Sci.* **20**, (2019).

104. Chang, E.-A., Jin, S.-W., Nam, M.-H. & Kim, S.-D. Human Induced Pluripotent Stem Cells : Clinical Signifi-cance and Applications in Neurologic Diseases. *J Korean Neurosurg Soc* **62**, 493–501 (2019).

105. Induced Pluripotent Stem Cells (iPS) | UCLA Broad Stem Cell Center. https://stemcell.ucla.edu/induced-pluripotent-stem-cells.

106. Cereso, N. *et al.* Proof of concept for AAV2/5-mediated gene therapy in iPSC-derived retinal pigment epithelium of a choroideremia patient. *Mol. Ther. Methods Clin. Dev.* **1**, 14011 (2014).

107. Duong, T. T. *et al.* Use of induced pluripotent stem cell models to probe the pathogenesis of Choroideremia and to develop a potential treatment. *Stem Cell Res.* **27**, 140–150 (2018).

108. Fronk, A. H. & Vargis, E. Methods for culturing retinal pigment epithelial cells: a review of current protocols and future recommendations. *J. Tissue Eng.* **7**, (2016).

109. Seabra, M. C., Ho, Y. K. & Anant, J. S. Deficient geranylgeranylation of Ram/Rab27 in choroideremia. *J. Biol. Chem.* **270**, 24420–24427 (1995).

110. Foltz, L. P. & Clegg, D. O. Rapid, Directed Differentiation of Retinal Pigment Epithelial Cells from Human Embryonic or Induced Pluripotent Stem Cells. *J. Vis. Exp.* **2017**, (2017).

111. Filipa, D. & Oliveira, C. De. BSc in Biotechnology iPS Cell modeling of Choroideremia disease : Insights into trafficking pathways and necroptosis. (2021).

112. Parinot, C., Rieu, Q., Chatagnon, J., Finnemann, S. C. & Nandrot, E. F. Large-Scale Purification of Porcine or Bovine Photoreceptor Outer Segments for Phagocytosis Assays on Retinal Pigment Epithelial Cells. *J. Vis. Exp* 52100 (2014) doi:10.3791/52100.

113. Kobayashi, T. *et al.* The tetraspanin CD63/lamp3 cycles between endocytic and secretory compartments in human endothelial cells. *Mol. Biol. Cell* **11**, 1829–1843 (2000).

114. Piper, R. C. & Katzmann, D. J. Biogenesis and function of multivesicular bodies. *Annu. Rev. Cell Dev. Biol.* **23**, 519–547 (2007).

115. Turk, V. *et al.* Cysteine cathepsins: from structure, function and regulation to new frontiers. *Biochim. Biophys. Acta* **1824**, 68–88 (2012).

116. Albrecht, L. V., Tejeda-Muñoz, N. & De Robertis, E. M. Protocol for Probing Regulated Lysosomal Activity and Function in Living Cells. *STAR Protoc.* **1**, (2020).

117. More, K. N. *et al.* Molecular design of fluorescent pH sensors based on reduced rhodol by structure-pKa relationship for imaging of lysosome. *Dye. Pigment.* **184**, 108785 (2021).

118. LysoTracker™ Deep Red. https://www.thermofisher.com/order/catalog/product/L12492.

119. Anderson, R. G. W. & Orci, L. A view of acidic intracellular compartments. *J. Cell Biol.* **106**, 539 (1988).

120. Paroutis, P., Touret, N. & Grinstein, S. The pH of the secretory pathway: Measurement, determinants, and regulation. *Physiology* **19**, 207–215 (2004).

121. Kaemmerer, E., Schutt, F., Krohne, T. U., Holz, F. G. & Kopitz, J. Effects of Lipid Peroxidation-Related Protein Modifications on RPE Lysosomal Functions and POS Phagocytosis. *Invest. Ophthalmol. Vis. Sci.* **48**, 1342–1347 (2007).

122. Bissig, C., Rochin, L. & van Niel, G. PMEL Amyloid Fibril Formation: The Bright Steps of Pigmentation. *Int. J. Mol. Sci. 2016, Vol. 17, Page 1438* **17**, 1438 (2016).

123. Barral, D. C. *et al.* Current methods to analyze lysosome morphology, positioning, motility and function. *Traffic* **23**, 238–269 (2022).

124. Press, B., Feng, Y., Hoflack, B. & Wandinger-Ness, A. Mutant Rab7 Causes the Accumulation of Cathepsin D and Cation-independent Mannose 6-Phosphate Receptor in an Early Endocytic

Compartment. *J. Cell Biol.* **140**, 1075–1089 (1998).

Supplementary Information

1. ARPE-19 CHM clones – choosing the right clone

Upon genetic manipulation of the *CHM* gene in ARPE-19 cells, six different mutant clones were previously generated and stored in our lab. The successful CHM gene knockout was previously confirmed by WB and sequencing. In order to choose between the different clones for the one most appropriate to characterize the endo-lysosomal pathway as well as key RPE features, we assayed all clones for three RPE characteristics; monolayer morphology and organisation, REP1 expression and ability of phagocytose POS and for AFGs.

Immunofluorescence images of ZO-1, **Supplementary Figure 1 A**, a marker of tight junctions' protein, revealed different staining patterns between mutants, with a distinct conformation of both nuclei and tight junctions compared to other clones and WT cells (**Figure 15)**. in clone 8 and 10. Clones 1,4, 5 and 9 have a confluent monolayer of cells with an organized structure and well-defined borders between cells.

Western blot analysis of REP1 protein, **Supplementary Figure 1 B**, showed that all mutant clones lacked REP1 expression, therefore confirming *CHM* gene CRISPR-Cas9 induced knockout. To gain some insight as to whether the endo-lysosomal pathway was intact, we analysed LAMP1 expression, where clone 10 showed a very significant decrease in the amount of LAMP1 expressed, when compared with the other clones and control cells. Since our main goal is to study this pathway, we eliminated Clone 10. The expression of a mitochondrial marker, TOM20, was also analysed by WB and the results revealed a decrease in expression in both clone 8 and 10, **Supplementary Figure 1 B**. The decreased expression of TOM20 in clones 8 and 10 (Supplementary Figure 1 B) suggests a possible cellular dysfunction in the mitochondrial level, indicating a possible upregulation of cellular stress and toxicity, and thus these clones were not chosen for further analysis. Given the essential phagocytic function of RPE cells in the human retina and the already verified AFGs accumulation in ARPE-19 cells and hfRPE[46], we decided to analyse by FACS the % of 488 positive cells after a 4 hour POS feeding followed by a 72 hour chase,, **Supplementary Figure 1 C**. Results show that, while clone 1 had similar amounts of POS phagocytosis when compared to control cells, all other clones showed a clear increase, with a statistically significant increase in both clone 4 and 5.

With all the information collected regarding the mutant clones, we decided to use clone 4 for further studies on the characterization of the endo-lysosomal pathway in the absence of REP1. This clone showed an organised and tight monolayer, did not express REP1 and showed the ability to phagocytose POS and produce AFGs, all key elements for our future studies are expressed and AFGs accumulate as seen before in ARPE-19 cells, we decided to employ this clone in our studies.

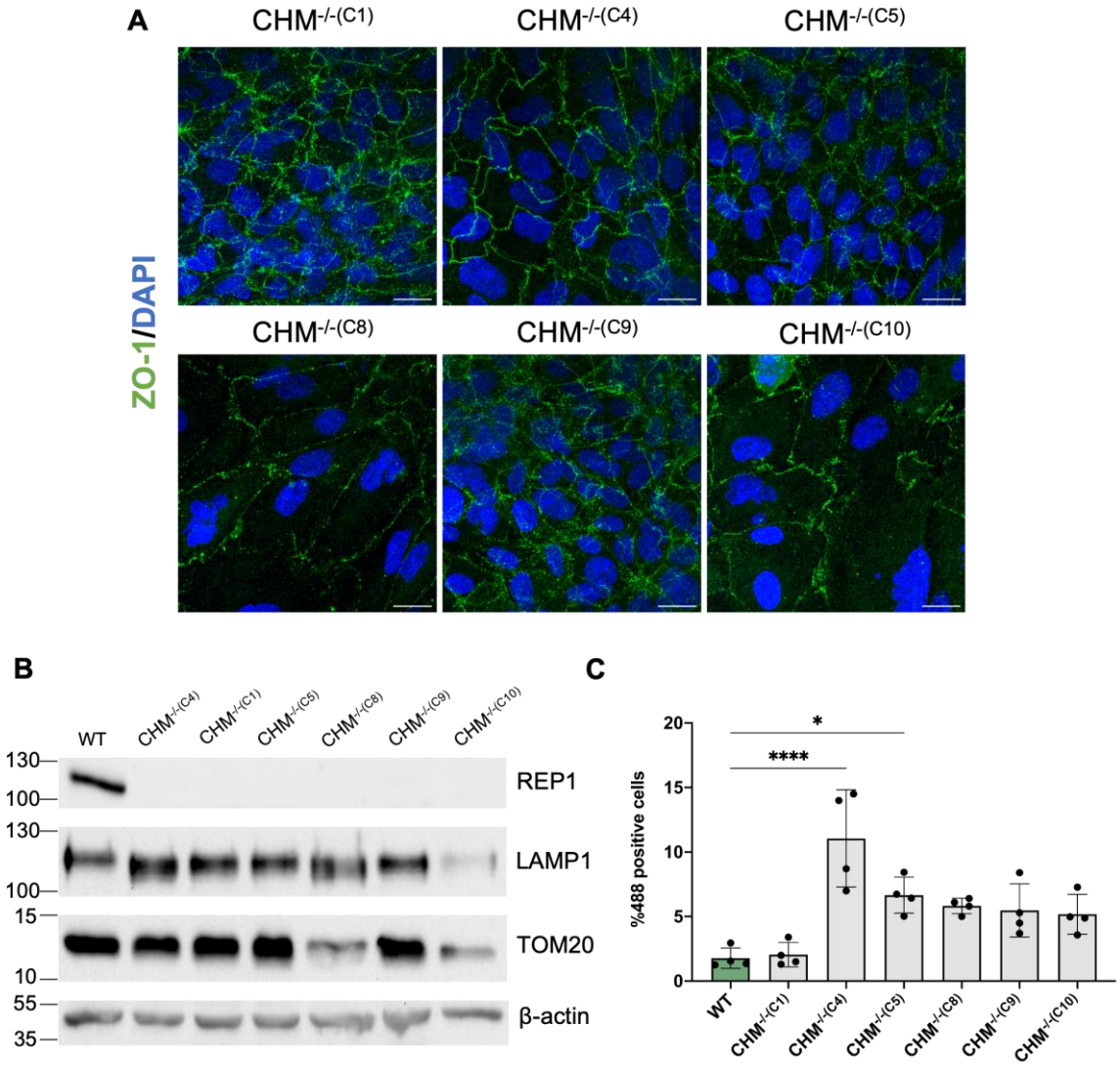

Supplementary Figure 1. Characterization of CRISPR/Cas9 CHM-/- clones in ARPE-19 cells. **A)** Immunofluorescence images of tight junctions' marker, zonula occludins-1 (ZO-1), green with nuclei stained with DAPI (blue). Scale bar 20 μm. **B)** Western blot analysis of REP1, LAMP1 and TOM20 expression in whole cell lysates between WT and different CHM$^{-/-}$ clones (C1, C4, C5, C8, C9 and C10), representative of n=1 independent experiment. Loading control: b-actin. **C)** Quantification of % of 488+ cells after 4h POS feeding and 72h chase using FACS. Data is presented as Mean ± SD, representative of n=1 independent experiment. Statistical comparisons were performed in technical replicates using one-way ANOVA test (*P<0.05, ****P<0.0001). The graph only presents significant statistical comparisons between WT and different clones.

2. Western Blot analysis – ARPE-19 cell model

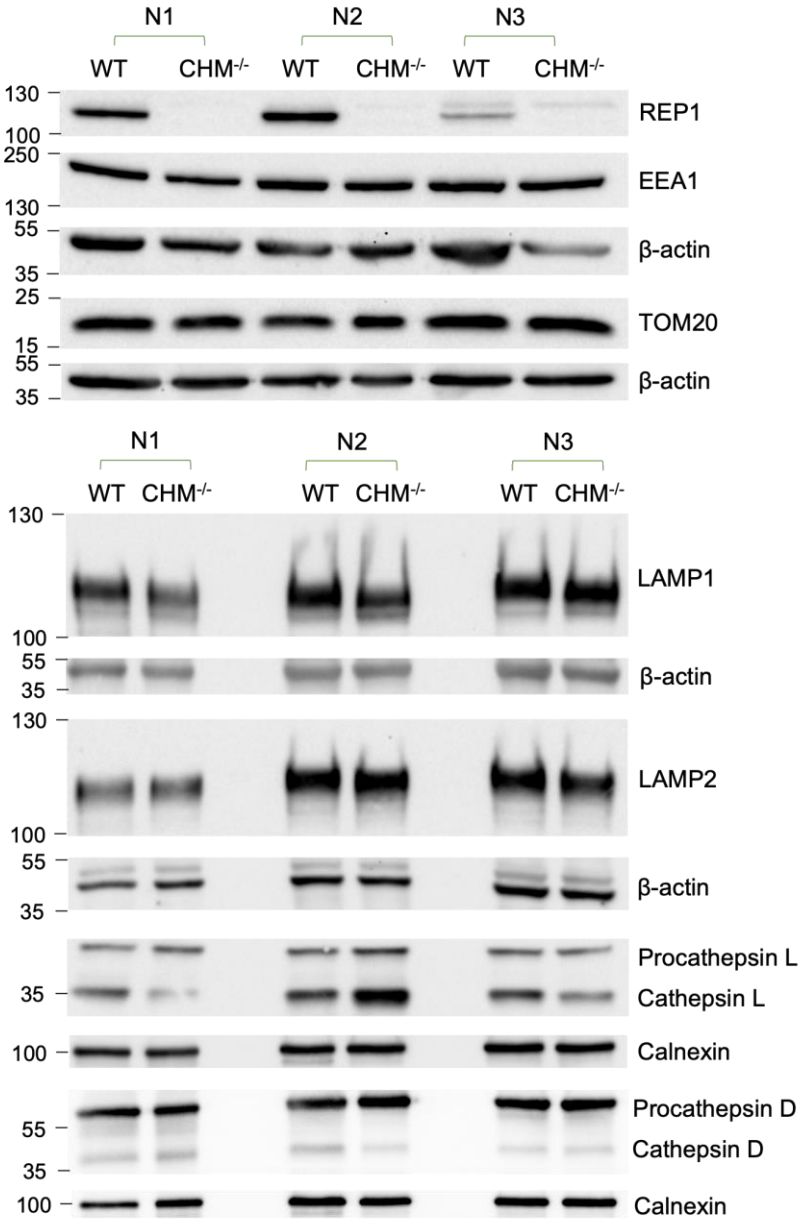

Supplementary Figure 2. Expression levels of several proteins in ARPE-19 cell model. Western blot analysis of REP1, EEA1, TOM20, LAMP1, LAMP2, Cathepsin L and Cathepsin D expression in whole cell lysates between WT and different CHM$^{-/-}$ cells, representative of n=3 independent experiments. Loading control: β-actin and calnexin.

3. Western Blot analysis – hiPSc-RPE cell model

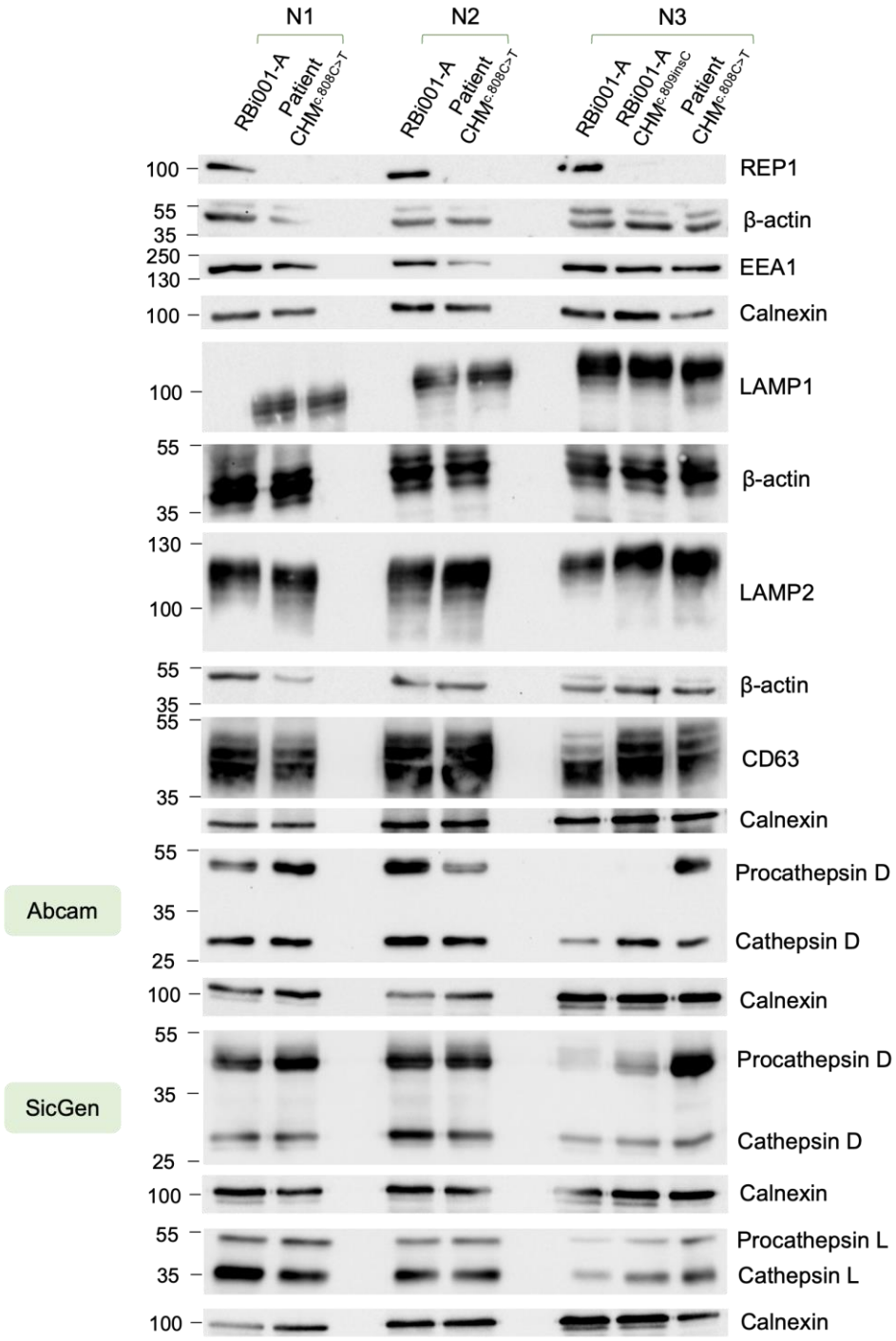

Supplementary Figure 3. Expression levels of several proteins in hiPSc-RPE cell model. Western blot analysis of REP1, EEA1, TOM20, LAMP1, LAMP2, CD63, Cathepsin D (Abcam and SicGen), Cathepsin L expression in whole cell lysates between healthy (RBi001-A) and CHM (RBi001-A CHM$^{c.809insC}$ and Patient CHM$^{c.808C>T}$) cells, representative of n=3 for RBi001-A and Patient CHM$^{c.808C>T}$ and n=1 for RBi001-A CHM$^{c.809insC}$. Loading control: β-actin and calnexin.

4. Automatic image analysis and structure quantification – Macros

In order to quantify immunofluorescence images of markers related to the endo-lysosomal pathway, cell structures and other organelles we developed an automatic image analysis protocol making use of macros in Fiji software in order to quantify target structures in an unbiased manner. Firstly, in images obtained directly from the microscope, each channels needs to be individually processed and the one that has the target structures saved in Tif format. To do so, we employ the use of the first macro, **Supplementary Figure 4**.

```
// Encontrar ficheiros
// Abrir ficheiros
// Z-project & Merge channels
// Save

//////////////// make an "input" and an "output" folder and
copy the folder path into the lines below////
////place images in input folder////


// Step 0: initialize variables
dir_in = "path of input folder";   //note, no spaces allowed
in folder names
dir_out = "path of output folder";

colors = getluts(3);      // This asks the user for 3 LUTs

setBatchMode(true);

// Step 1: Find files
allfiles = getFileList(dir_in);

// Step 2: Open files
for(i=0; i<lengthOf(allfiles); i++){

                    this_file = allfiles[i];
                    // open file
                    run("Bio-Formats Importer", "open=" +
dir_in + "/" + this_file +
                    " autoscale color_mode=Default
rois_import=[ROI manager] split_channels
                    view=Hyperstack
stack_order=XYCZT");
                    titleC1 = this_file + " - C=0";
                    titleC2 = this_file + " - C=1";
                    titleC3 = this_file + " - C=2";

                    // Step 3.1: Z-Project channels
                    selectWindow(titleC1);
                    run(colors[0]);
                    run("Z Project...", "projection=[Max
Intensity]");
                    selectWindow(titleC2);
                    run(colors[1]);
                    run("Z Project...", "projection=[Max
Intensity]");
                    wait(2000);
                    selectWindow(titleC3);
                    wait(2000);
                    run(colors[2]);
                    run("Z Project...", "projection=[Max
Intensity]");
                    titleC1_MAX = "MAX_" + titleC1;
                    titleC2_MAX = "MAX_" + titleC2;
                    titleC3_MAX = "MAX_" + titleC3;

//save x channel - need to choose channel
                    selectWindow(titleC1);
                    run("Z Project...", "projection=[Max
Intensity]");
                    path_out = dir_out + "/x_" + this_file;
                    saveAs("tiff", path_out);

//save y channel - need to choose channel
                    selectWindow(titleC2);
                    run("Z Project...", "projection=[Max
Intensity]");
                    path_out = dir_out + "/y_" + this_file;
                    saveAs("tiff", path_out);

                    // Step 3.2: Merge channels
                    run("Merge Channels...", "c1=[" +
titleC1_MAX + "]
                    c2=[" + titleC2_MAX + "] c3=[" +
titleC3_MAX + "] create");

                                        // Autoscale again...
                                        for (j = 1; j <= 3; j++)
{

                    Stack.setChannel(j);

                    run("Enhance Contrast",
"saturated=0.2");
                                        }

                    // You can spot detect here..


                    // Step 4: Save file
                    path_out = dir_out + "/RGB_" +
this_file;
                    saveAs("tiff", path_out);

                    path_out = dir_out + "/PNG_" +
this_file;
                    saveAs("PNG", path_out);

                    // Step 5: clean up
                    run("Close All");
}

// return 3 lut names as an array
function getluts(nluts){

                    all_luts = getList("LUTs");

                    // create dialog box
                    Dialog.create("LUT selector");
                    for (i = 1; i <= nluts; i++) {

                    Dialog.addChoice("LUT for channel " +
i, all_luts, all_luts[i+4]);
                     // Red, Green, Blue, ...
                    }
                    Dialog.show();

                    // Retrieve data
                    result = newArray(nluts);
                    for (i = 0; i < nluts; i++) {
                                        result[i] =
Dialog.getChoice();
                    }

                    return result;
}
```

Supplementary Figure 4. Macro script to analyse individual channels and obtain images for further quantification. An input and output folder must be created, followed by the attribution of the desired colours to the different channels. The different channels are then stacked and merged with an auto scale in

brightness and contrast. Images are saved in both PNG and RGB with the desired channel also saved in Tif for further quantification.

For image quantification, the second macro, **Supplementary Figure 5**, is used, where images in Tif format are put in the input folder. With this macro, depending on the structure being quantified, we need to choose different parameters, which are described in **Supplementary Table 1**.

```
dir_in = "path of input folder";   //note, no spaces allowed in
folder names
dir_out = "path of output folder";

//clean up
run("Close All");
run("Clear Results");
roiManager("reset");

setBatchMode(false);

// Step 1: Find files
allfiles = getFileList(dir_in);

// Step 2: Open files
for(i=0; i<lengthOf(allfiles); i++){

                this_file = allfiles[i];
                // open file
                run("Bio-Formats Importer", "open=" + dir_in + "/" +
this_file +
                " autoscale color_mode=Default rois_import=[ROI
manager]        split_channels
                view=Hyperstack stack_order=XYCZT");

                rename(this_file);

run("Set Measurements...", "area mean standard modal min display
redirect=None decimal=3");

//For segmentation and quantification

// 1 - Smooth or gaussian blur
run("Smooth");

// 2 - Subtract background from images
run("Subtract Background...", "rolling=x");

// 3 - Set auto local threshold or normal threshold
run( ..............................)

// 4 - Watershed
run("Watershed");

// 5 - Analyze particles
(don't clear results - will add to summary table)
run("Analyze Particles...", "size=x-y show=Outlines display
exclude include summarize add");
```

```
path_out = dir_out + "/PNG_" + this_file;
saveAs("PNG", path_out);

}

//save summary table
selectWindow("Summary");
saveAs("results", dir_out  + "/" + this_file + "_summary.csv");
close ();

selectWindow("Results");

                for (i = 0; i < Table.size ; i++) {
                                name = Table.getString("Label", i);

                                sepname = split(name, "_.");

                                Table.set("Condition1", i, sepname[1]);
                                Table.set("Condition2", i, sepname[2]);
                                Table.set("Condition3", i, sepname[3]);
                }

saveAs("results", dir_out  + "/" + this_file + "_results.csv");
close ();


// loop to make table

                for (i = 0; i < 10; i++) {
                                name = Table.getString("Label", i);

                }
```

Supplementary Figure 5. Macro script for quantification of a desired channel. Tif images are now put in the input folder and different parameters are chosen according to the structure being analysed. These parameters include, smooth filter, background subtraction where we choose the rolling ball radius in pixels, manual or auto local threshold, watershed for vesicle separation if needed and analyse particle function with a size exclusion filter. The output will be a summary table with the desired measurements, such as count and size, as well as an individual table for each vesicle.

Supplementary Table 1. Type of threshold and size filter for each structure and cell model

Structure	Threshold	Size filter ARPE-19	Size filter hiPSc-RPE
EEA1+ vesicles	Manual threshold	0.05-1.0	0.025-0.5
LAMP1+ vesicles	Auto local threshold phansalkar (ARPE-19)/bersten (hiPSc-RPE)	0.1-Infinity	0.05-Infinity
LAMP2+ vesicles	Auto local threshold bersten	0.1-Infinity	0.05-Infinity
Rab7+ vesicles	Auto local threshold bersten	0.1-Infinity	-
CD63+ vesicles	Auto local threshold bersten	0.1-Infinity	0.05-Infinity
Cathepsin D+ vesicles (R&D)	Manual threshold	0.1-Infinity	-
Cathepsin D+ vesicles (SicGen)	Manual threshold	0.1-Infinity	-
Cathepsin D+ vesicles (BDT)	Auto local threshold bersten	-	0.05-Infinity
SiR-lysosome+ vesicles	Auto local threshold bersten	0.1-Infinity	-
Cathepsin B+ vesicles	Manual threshold	0.1-Infinity	-
Magic Red Cathepsin B+ vesicles	Auto local threshold bersten	0.1-Infinity	-
Magic Red Cathepsin L+ vesicles	Auto local threshold bersten	0.1-Infinity	-
Lysotracker+ vesicles	Auto local threshold bersten	0.1-Infinity	-
pHRODO Dextran+ vesicles	Manual threshold	0.1-Infinity	-
AFGs	Auto local threshold bersten	0.0-20	-
TOM20+ network	Manual threshold	0.0-Infinity	-